Lilly, J. M., P. B. Rhines, F. Schott, K. Lavender, J. R. N. Lazier, U. Send, and E. D'Asaro (2003). Observations of the Labrador Sea eddy field. *Progress in Oceanography* **59**(1):75-176.

Observations of the Labrador Sea eddy field

Jonathan M. Lilly [i,*,†], Peter B. Rhines [i], Friedrich Schott [ii],
Kara Lavender [iii], John Lazier [iv], Uwe Send [ii], Eric D'Asaro [i]

[i] *School of Oceanography, Box 357940, University of Washington, Seattle, WA 98195, USA*
[ii] *Institut für Meereskunde an der Universität Kiel, Düstenbrooker Weg 20, D-24105 Kiel, Germany*
[iii] *Physical Oceanography Department, MS #21, Woods Hole Oceanographic Institution, Woods Hole, MA 02543*
[iv] *Bedford Institute for Oceanography, P.O. Box 1006, Dartmouth, Nova Scotia B2V 4A2, Canada*

Abstract

This paper is an observational study of small-scale coherent eddies in the Labrador Sea, a region of dense water formation thought to be of considerable importance to the North Atlantic overturning circulation. Numerical studies of deep convection emphasize coherent eddies as a mechanism for the lateral transport of heat, yet their small size has hindered observational progress. A large part of this paper is therefore devoted to developing new methods for identifying and describing coherent eddies in two observational platforms, current meter moorings and satellite altimetry. Details of the current and water mass structure of individual eddy events, as they are swept past by an advecting flow, can then be extracted from the mooring data. A transition is seen during mid-1997, with long-lived boundary current eddies dominating the central Labrador Sea year-round after this time, and convectively-formed eddies similar to those seen in deep convection modeling studies apparent prior to this time. The TOPEX / Poseidon altimeter covers the Labrador Sea with a loose "net" of observations, through which coherent eddies can seem to appear and disappear. By concentrating on locating and describing anomalous events in individual altimeter tracks, a portrait of the spatial and temporal variability of the underlying eddy field can be constructed. The altimeter results reveal an annual "pulsation" of energy and of coherent eddies originating during the late fall at a particular location in the boundary current, pinpointing the time and place of the boundary current-type eddy formation. The interannual variability seen at the mooring is reproduced, but the mooring site is found to be within a localized region of greatly enhanced eddy activity. Notably lacking in both the annual cycle and interannual variability is a clear relationship between the eddies or eddy energy and the intensity of wintertime cooling. These eddy observations, as well as hydrographic evidence, suggest an active role for boundary current dynamics in shaping the energetics and water mass properties of the interior region.

Keywords: Labrador Sea; Coherent eddies; Deep convection; Wavelets; Subpolar gyre; Current meter moorings; TOPEX / Poseidon altimeter

*Current affiliation: Laboratoire d'Océanographie Dynamique et de Climatologie, Université Pierre et Marie Curie à Paris 6, Paris, France
†Corresponding author. *E-mail address:* jonathan.lilly@lodyc.jussieu.fr

Contents

1. Introduction

This paper is an observational study of deformation-scale eddies in Labrador Sea, one of the primary sites for deep convection in the world ocean. As such it concerns the intersection of several research areas: the role of the Labrador Sea in the ocean-atmosphere system, the physics of deep convection, and the nature of the oceanic eddy field. Relevant ideas from each of these will be reviewed in turn.

1.1. The Labrador Sea

The Labrador Sea, located between the west coast of Greenland and the Labrador coast of Canada (Fig. 1), is the site of some of the deepest convection in the world ocean, with convection during intense winters reaching to over 2 km depth Lazier (1980), Clarke & Gascard (1983). The resulting cold, fresh, isopycnally thick Labrador Sea Water (LSW) spreads out at middepths (Talley & McCartney 1982), becoming one of the major water mass components of the North Atlantic. The depth of convection there has long been known to vary on decadal time scales (Lazier 1980) and appears strongly linked to the large-scale atmospheric variability (Dickson, Lazier, Meincke, Rhines & Swift 1996). Indeed, the deep convection in the Labrador Sea all but shut down in the 1960's (Lazier 1980) as a combined result of the "Great Salinity Anomaly" (Dickson, Meincke, Malmberg & Lee 1988) and a weakened North Atlantic Oscillation (NAO) (Dickson et al. 1996). Thickness variations of the Labrador Sea Water have large-scale consequences since newly formed LSW rapidly reaches the subtropical gyre (Curry, McCartney & Joyce 1998), altering the potential vorticity structure and impacting the ocean dynamics.

These observations of the variability of deep convection in the Labrador Sea take on new importance in the light of recent numerical studies. Climate model experiments illustrate the sensitivity of the ocean thermohaline circulation to high-latitude freshwater anomalies (Rahmstorf 1996, Häkkinen 1999), an effect which contributes to the slowing or total shutdown of the thermohaline circulation in long-term global warming simulations (Rahmstorf & Ganopolski 1999). The Labrador Sea, positioned at the confluence of three major freshwater pathways — the West Greenland Current, the Baffin Island Current, and Hudson Straight outflow (Khatiwala, Schlosser & Visbeck 2002) — may be particularly sensitive to atmospheric freshwater forcing (Häkkinen 2000). The significance of such simulations is underscored by paleoceanographic sediment core research, showing major transitions in the North Atlantic circulation and deep water formation have indeed occurred over the past 30,000 years (Keigwin, Jones, Lehman & Boyle 1991, Sarnthein, Winn, Jung, Deplessy, Labeyrie, Erlenkeuser & Ganssen 1994) involving times scales as short as a few decades (Lehman & Keigwin 1992); in particular, deep water formation in the Labrador Sea seems not to have occurred during the last interglacial period (Hillaire-Marcel, de Vernal, Bilodeau & Weaver 2001).

1.2. Deep convection

The physics of deep convection involves organization of the ocean from the scales of the mixing elements or "plumes" [O(1) km], to the baroclinic deformation radius [O(10) km], to the scales of the forcing and the ocean basin [O(100)–O(1000) km] (Clarke & Gascard 1983, Gascard & Clarke 1983, Maxworthy & Narimousa 1994, Jones & Marshall 1993). The response of a laterally uniform ocean to a localized forcing in laboratory (Maxworthy & Narimousa 1994) and numerical (Jones & Marshall 1993) experiments proceeds as follows. Convective plumes mix the water column in the vertical, creating a dense cylinder of water known as a "chimney". A rim current forms around the chimney which becomes baroclinically unstable, developing into eddies which can both disperse convected water away from the chimney, and replace it with more buoyant ambient waters (Legg & Marshall 1993, Jones & Marshall 1997).

Variations on this localized-forcing scenario, as well as "chimney adjustment" problems which develop from the initial condition of a dense chimney, have proved a fruitful avenue of research, yielding estimates of large-scale effects of deep convection (Send & Marshall 1995, Jones & Marshall 1997, Send & Käse 1998). Importance differences between the case of a laterally homogeneous ocean with a localized forcing, and the more realistic case of a laterally homogeneous forcing with localized eddy structures, have also been noted (Legg, McWilliams & Gao 1998, Straneo & Kawase 1999). Recent experiments are providing the next level of realism, showing for instance that convection interacting with a pre-existing eddy field leads to a modification of the energy cascade (Legg & McWilliams 2001) compared with the case of pure geostrophic turbulence (Rhines 1979). Additionally the existence of bottom topography results in a much greater and more rapid excitation of the gyre-scale circulation (Hallberg & Rhines 1996, Rhines 1998) compared with a flat-bottomed ocean.

The localized-forcing experiments offer predictions for the basic behavior of ocean currents and water mass exchange, both of which are driven, via baroclinic instability (Jones & Marshall 1993), by localized surface heat loss. The lateral, eddy-mediated ocean heat flux arises to counteract a localized heat loss to the atmosphere (Send & Marshall 1995, Jones & Marshall 1997). Domain-averaged kinetic energy increases while buoyancy loss continues, then levels off or drops when buoyancy loss ceases depending upon whether ocean eddies were or were not present initially (Legg & McWilliams 2001).

As an organizing principle, it is useful to ask whether the observations support the hypothesis that the interior Labrador Sea merely responds passively to local heat flux forcing, that is, whether the localized-forcing convection experiments capture the essential elements of interior Labrador Sea variability. This may be termed the "isolated convection region" model of the Labrador Sea, "isolated" in the sense that remote ocean dynamics and remote atmospheric forcing are unimportant. It will be shown that this is not the case.

1.3. Coherent eddies

Long-lived deformation-scale structures, generally referred to as "coherent eddies", are expected to play a particularly important role in convective regions such as the Labrador Sea. Modeling studies show baroclinic, property-carrying eddies mediate the exchange of water between a convected region with its surroundings (Jones & Marshall 1993, Legg & Marshall 1993, Send & Marshall 1995, Jones & Marshall 1997, Rhines 1998). Coherent eddies may be important to deep convection in another way: upward isopycnal deflection inside cyclonic eddies can destabilize the upper water column, "preconditioning" it for deep convection (Legg et al. 1998, Straneo & Kawase 1999). The interaction between convection and eddies is therefore not only important to the dynamics of the convecting region, but also to the gyre-scale relationship between the convectively-generated product and the surrounding water masses.

In order to gauge the consequences of the neglect of small-scale eddies in ocean general circulation models, it is necessary understand the role of those eddies in the real ocean. A recent sensitivity study (England & Rahmstorf 1999) showed a factor of two variability in the deep water ventilation timescale depending on the choice of subgrid-scale mixing parameterization, indicating the global importance of small-scale oceanic features. Coherent eddies in particular may be difficult to parameterize since they have the potential to self-propagate in a gradient of planetary (Smith 1993, Lam & Dritschel 2001) or topographic (LaCasce 1998) potential vorticity, and so do not necessarily flux properties according to a simple down-gradient transport law; this tendency appears to permit Meddies (Mediterranean water eddies in the North Atlantic) to deform the shape of the Mediterranean salinity tongue (Stephens & Marshall 1999).

A basic question is the dominant polarity of eddies in convecting regions. Submesoscale ed-

dies appear to be predominantly anticyclonic (McWilliams 1985), yet one would not necessarily expect a similar situation in the Labrador Sea. Some theoretical evidence for an evolution asymmetry exists, such as shallow water elliptical eddy experiments (Arai & Yamagata 1994) showing stable anticyclones but fragmentation of cyclones. Interestingly, when a buoyancy loss forcing is applied to a preexisting deformation-scale eddy field in a numerical model (Legg & McWilliams 2001) the opposite tendency is observed, with diffuse anticyclones and more intense cyclones. Models of localized deep convection (Jones & Marshall 1993) or of the adjustment of a dense cylinder much larger than the radius of deformation (Send & Käse 1998), however, show generation of cyclones and anticyclones of comparable strengths and equal numbers. Understanding these various effects is important, since an asymmetry would be expected to have consequences for the large-scale influence of the eddy field.

1.4. The observational challenge

The importance of the relatively small scales to the large scale in convecting regions presents a challenge to both observational and modeling studies. While observations of mesoscale and submesoscale eddies abound, there are only a handful of reports of eddies in convecting regions (Gascard 1978, Gascard & Clarke 1983, Prater 2002). Studying the deformation-scale eddy field is particularly difficult in the high latitudes where the deformation radius is small (about 7 km in the Labrador Sea). Until recently, the entire body of knowledge concerning the Labrador Sea eddy field consisted of a careful study of several drifter tracks performed some twenty years ago (Gascard & Clarke 1983). Other authors (Marshall & Schott 1999, Send & Käse 1998) find in reviewing the convection literature a similar scarcity of eddy observations.

In the past few years the Labrador Sea has been the focus of an intense, coordinated research effort (Labrador Sea Group 1998), including a wintertime hydrographic survey (Pickart, Torres & Clarke 2002), numerous float studies (Steffen & D'Asaro 2002, Lavender, Davis & Owens 2000, 2002, Prater 2002, Cuny, Rhines, Niiler & Bacon 2002), numerical modeling (Harcourt 1999), annual hydrographic sections (Lazier, Hendry, Clarke, Yashayaev & Rhines 2002) including transient tracer measurements (Khatiwala et al. 2002), and the mooring project (Lilly, Rhines, Visbeck, Davis, Lazier, Schott & Farmer 1999), as well as additional moorings and a tomographic array. Recent observations in the Labrador Sea have greatly increased our understanding of the plume scale (Steffen & D'Asaro 2002) and gyre scale (Lavender et al. 2000, 2002) dynamics in this region.

A few more observations of coherent eddies are now available. Prater (2002) presents three float tracks and a sea surface brightness temperature image showing eddy generation near 61.5°N, 52°W in the West Greenland Current. In a pilot version of the first part of this study, Lilly and Rhines (2002) [hereafter LR] showed via simple analytic models that an advected eddy results in a characteristic geometrical structures on the (u, v) plane; these "hodographs" were used together with time-depth cross-sections to locate and describe six eddies in a six-month long mooring record. However, this handful of observations provides little information with which to constrain the modeling studies of deep convection. As the range of possibilities is no doubt broader than can be efficiently explored with modeling alone, more observations of convective eddy fields are clearly necessary.

Much of our knowledge of these scales comes from concentrated hydrographic surveys, allowing detailed study of eddy dynamics (Ruddick 1992, Prater & Sanford 1994) and occasionally of long-term evolution (Armi, Hebert, Oakey, Price, Richardson & Rossby 1989). Hydrographic surveys are, however, not well suited to examining the distribution of coherent eddies over a large spatial domain or their temporal variability. For such applications satellite altimetry has proved invaluable, permitting on the one hand the tracking of individual features (Stammer, Hinrichsen

& Käse 1991, Byrne, Gordon & Haxby 1995), and on the other the bulk measurement of kinetic energy associated with eddy-scale fluctuations of the sea-surface height (Stammer & Böning 1992, White & Heywood 1995, Stammer & Wunsch 1999).

The importance of the Labrador Sea motivated the establishment of a long-term mooring, located at 56.75° N, 52.5° W (see Fig. 1) near the site of the former Ocean Weather Ship Bravo. The "Bravo" mooring, and its nearby sister mooring "K1", are intended to monitor oceanographic variability in the central Labrador Sea, extending the valuable hydrographic measurements recorded by the weather ship during the 1960's and 1970's (Lazier 1980). From June of 1994 until June 2002 (with some data gaps) these moorings provided measurements of the currents and of temperature and salinity at multiple depths throughout the water column with at least hourly resolution. The use of mooring data in the coherent eddy literature is generally restricted to supplementing float or hydrographic observations. This is due in part to the difficulty in making meaningful statements from mooring observations alone. Yet the results of LR suggest long-term, densely-instrument moorings such as the Bravo mooring could contain important information about eddy structure and variability on annual and interannual time scales.

While a densely-instrumented mooring samples the entire water column at a fixed point, a satellite altimeter observes the "skin" of the ocean globally. However, investigation of coherent eddies using satellite altimetry is inherently problematic for a variety of reasons: some criterion must be proposed for determining which sea surface excursions represent different dynamical features in the ocean interior; altimeter measurements are coarsely resolved in time and in one of two spatial dimensions; the signal due to eddies may be close to the noise level of the measurements; finally, the two-dimensional (x, y) sea surface height anomaly due to an eddy or a front can lead to a variety of one-dimensional "slices", in the way a shadow changes as an object is rotated.

One approach is to search through the altimeter data for what appear to be long-lived migrating features, and then to identify these with dynamically stable physical structures, an approach which has been used with success by other authors (Stammer et al. 1991, Byrne et al. 1995). This approach is however difficult to automate, and is not appropriate for rapidly propagating or small-scale eddies that can "fall through the cracks" of the altimeter grid. Further such a subjective approach does not lend itself to comparison with a noise model, and therefore it is impossible to evaluate whether the data is being underutilized or over-interpreted.

Both the "eddy-tracking" methods employed in satellite altimeter studies, and LR's graphical eddy-identification method, are limited by being inherently subjective. Part of the problem is that traditional analysis methods do not accommodate features, like coherent eddies, which are neither sinusoids nor delta-functions. The continuous wavelet transform offers a natural way of representing such features, and provides a useful language for forming an objective definition of an "eddy-like" event. Isolated structures having certain specific properties can then be extracted automatically from large datasets. Additional analysis of the mooring data leads to details of individual coherent eddies, while from the altimeter data one obtains estimates of eddy populations constrained within error bars.

1.5. An overview of this paper

A brief overview of observed large-scale changes during the 1990's is given in Section 2. In Section 3, the graphical approach of LR will be extended and applied to a much larger mooring dataset spanning the time period 1994–2000, using the continuous wavelet transform to visualize and partially automate the detection process. A comprehensive census of eddy features in seven mooring-years of data is performed in Section 4, revealing fundamental changes in the eddy

structures over this time period. Attention then turns towards satellite altimetry in order to investigate questions of spatial variability raised by the mooring analysis. Section 5 develops a wavelet-based automated census algorithm for the alongtrack altimeter data, including the statistical groundwork necessary to place confidence limits on estimations of eddy field parameters. Results of the altimeter census are given in Section 6 together with a discussion of the eddy observations and their relationship to the large-scale structure. Finally a summary and discussion is given in Section 7.

2. An overview of the 1990's

The nineteen-nineties was a decade of remarkable changes in the Labrador Sea which were observed by a host of platforms, including hydrographic surveys (Lazier et al. 2002, Pickart et al. 2002), moorings (Lilly et al. 1999), and four types of floats and drifters (Prater 2002, Cuny et al. 2002, Lavender et al. 2000, 2002, Steffen & D'Asaro 2002). In this section the variability of the heat flux and wind stress forcing, water mass properties, currents, and estimated lateral heat fluxes will be examined, including ideas from the literature as well as some new results. In particular, observed variability will be compared with that expected under the "isolated convection region" hypothesis discussed in Section 1.2. This primarily qualitative and large-scale discussion will set the stage for the more focussed and quantitative analysis to follow.

The locations of mooring and hydrographic data used in this study are shown in Fig. 2. Observed annual and interannual variability of the various fields are summarized in Fig. 3. The discussion of this figure row by row constitutes the bulk of this section.

2.1. Atmospheric forcing

Surface heat flux and wind stress forcing fields taken from the National Center for Environmental Prediction (NCEP) Global Reanalysis Project are presented in Fig. 3a,b. All NCEP heat fluxes have been adjusted as per Renfrew, Moore, Guest & Bumke (2002). Comparing the NCEP Reanalysis data with in situ observations, these authors find both heat flux and wind stress to be significantly overestimated (by about 50%) in the model reanalysis. They recompute the heat fluxes using a more appropriate bulk algorithm, reducing the bias magnitude by about 25% but also changing its sign to an underestimation. Nevertheless, model and observed fields were found to be strongly correlated ($\sim$0.8 correlation coefficient for momentum flux, $\sim$0.9 for both sensible and latent heat fluxes). For this reason one expects variability of the adjusted model fluxes to be indicative of variability in the real world, even though absolute magnitudes may be biased.

In examining surface fluxes, averages over two spatial domains will be considered. A "subpolar" region will be defined as 60° W–25° W and 45° N–65° N. The "Labrador Sea interior" will refer to the nearly circular region of 300 km radius described by the 3000 m isobath, with its center near the point 52° W, 58.5° N (see Fig. 2).

For wind stress forcing it is appropriate to take an average over a large spatial domain, since barotropic waves can propagate rapidly throughout the subpolar waveguide. Monthly-mean wind stress averaged over the subpolar region has a January–February peak and a June-July minimum (Fig. 3a). The Corresponding field averaged over the Labrador Sea interior only are virtually identical to this curves (not shown).

The June-to-June annual mean of wind stress (Fig. 3b) over the same spatial domain varies over a much smaller range than the annual cycle (0.04 N m^{-2} compared with 0.15 N m^{-2}) and has a scattered appearance from year to year. The years of strongest and weakest wind stress forcing were 1992 and 1998 respectively. Here interannual variability is expressed in terms of June-to-June annual means in order not to split a winter between two years, and to be consistent

with the annual hydrographic sections (see Section 2.3) which are typically taken in June. In this context "1997" will be understood to mean the year June 1997–June 1998, which encompasses January first of 1998. Interannual variability averaged over the interior Labrador Sea region is similar to that for the entire subpolar gyre, but tends to be of smaller magnitude when wind stress is large.

For surface heat flux, the local forcing is of interest. Monthly mean net surface heat gain, positive when the ocean is being warmed, is averaged over the Labrador Sea interior region. Cooling of the ocean is greatest during January–February (Fig. 3c, thick solid line), coincident with the wind stress maximum, with monthly-mean heat loss approaching 300 W m^{-2}. June and July are the months of greatest warming, with April and September marking the transitions between cooling and warming of the ocean. The deepest convection generally occurs in March (Lilly et al. 1999, Lavender et al. 2002), just before the surface heat flux changes sign and begins to warm the ocean.

As could be expected the June-to-June annual mean heat gain (Fig. 3d, thick grey line) is always negative — the atmosphere cools the ocean — and the interannual range of variability is much smaller, by a factor of ten, than the annual range. The average annual heat loss from 1990–1999 is 35 W m^{-2}. Extreme years were 1996, during which the heat loss was only 8W m^{-2}, and 1993, during which the heat loss was 67 W m^{-2}. Nineteen-ninety-seven is especially interesting because the relatively warm (i.e., having small heat losses) November and December of 1996 were offset by the very cold January of 1997, leading to an unexceptional November–January heat loss. However, the periods September–October 1996 and February–March 1997 were also colder than usual, so that the net heat loss over the entire winter was comparable in magnitude to that experienced during the early 1990's.

2.2. Temperature and current variability

A wealth of mooring data was collected in the interior Labrador Sea during 1994—1999. The locations of these moorings are shown in Fig. 2 and a detailed list of instrumentation is given in Table 1. For orientation, the deepest convection has been observed to occur (Clarke & Gascard 1983, Pickart et al. 2002, Lavender et al. 2002) mostly to the west of the Bravo mooring but offshore of the 3000 m isobath, an area referred to as the "convection region". The primary records used here are the Institut für Meereskunde (IFM) an der Universität Kiel K1 mooring and the University of Washington (UW) / Bedford Institute of Oceanography (BIO) Bravo mooring, located within about 20 km of each other along the World Ocean Circulation Experiment (WOCE) AR7W hydrographic line.

Combining these two moorings (Fig. 4) yields a nearly-continuous five-year record of currents and temperatures at multiple depths. During two of these years (1996–1997, 1998–1999) the two moorings overlapped. Salinity and density are well-resolved in the vertical in three years (1994–1995, 1996–1997, 1999–1999). Additionally IFM Kiel moorings K4, K5, K15, K17, and K20 provide five location-years of current and temperature data at one or two depths. All time series used in this section are at hourly resolutions and unless otherwise noted have been de-tided through lowpassing with a 24-point Hanning filter.

The annual variability of temperature (Fig. 5) involves first-order changes in the structure of the water column, but also has a very different appearance from year to year. As surface heat loss to the atmosphere continues to cool the ocean, the ocean surface mixed layer becomes statically unstable with respect to the underlying water column, resulting in a vertically homogenized "convective mixed layer" of increasingly greater depth. This process can be seen in Fig. 5 as the deepening of a layer of very cold ($<2.8°$C in b,c), convectively mixed water from a few hundred meters in January to a kilometer or more during March. A sudden warming, or restratification,

of the water column is subsequently apparent in late March or early April. Between 1994 and 1999, a significant warming of the water column also occurs, with the depth of the 3.2°C isotherm increasing from a few hundred meters to nearly one kilometer. Temperature fluctuations take on a more intermittent character in the later years: for 1994–1995 the most obvious feature is a roughly linear warming trend (for example, the sinking of the 2.8°Ctemperature contour), while during 1998–1999 several isolated patches of warm (>4°C) water obscure any such trend. Several smaller-amplitude, mid-depth cold cores are also visible during November 1996–January 1997.

The deep warming during 1994–1995 occurs even during months in which the surface heat loss is positive, implicating lateral oceanic heat fluxes. This time period was examined by Lilly et al. (1999), who concluded the observed temperature changes were due to a combination of vertical and lateral fluxes, with the long-term warming during June–December 1994 and the sudden restratification during March–April 1995 both being too large in magnitude and extending too deeply throughout the water column to be attributable to surface warming alone. In that study, the evolution during the warming periods was seen to indicate mixing of the interior Labrador Sea water with the warm, saline water of the bounding Irminger Current. The issue of lateral ocean heat fluxes will be address in more detail later in this section.

The moorings exhibit an annual cycle in speed, shown in Fig. 3e. Here each point is an average over the monthly-mean speed observed during different years or at different locations, for two groups of observations: those taken at the Bravo / K1 mooring (black circles), and those from other moorings (gray triangles). At each mooring the shallowest available instrument is used (see Table 1). Standard deviations among each group of monthly-mean values are also shown. Note the absence of any July observations for the non-Bravo /K1 moorings.

Increased speeds occur during April–June relative to the rest of the year, with average speeds of $\sim$35 cm s^{-1} at the Bravo / K1 location and $\sim$17 cm s^{-1} at the other moorings. Interestingly the tripling of speed at the Bravo / K1 mooring from $\sim$10 cm s^{-1} during February to more than 30 cm s^{-1} during April occurs as the surface fluxes are beginning to warm the ocean (Fig. 3c). Standard deviations are large owing to interannual and spatial variability.

Interannual variability (Fig. 3f) is found by averaging the speed over the entire length of each mooring deployment, for three groups of observations: the Bravo mooring (filled circles), the K1 mooring (open circles), and other moorings (triangles). At the Bravo / K1 location, the speed observed during 1998–1999 is a factor of three larger than that during June 1994–June 1996. Peak speeds of 80 cm s^{-1} are occasionally observed throughout years 1997–1998 and 1998–1999 (see Fig. 4), with monthly-mean speeds (not shown) often from 25 to 50 cm s^{-1}. By comparison, the monthly-mean speeds during 1994–1996 never exceeded 25 cm s^{-1}. The increase observed at the Bravo / K1 location during 1998–1999 coincides with a period of unremarkable surface heat losses, while the very cold winter of 1996–1997 does not stand out as being associated with particularly strong currents.

Yet it appears the Bravo site may be unusual: at the five additional single-year moorings during 1997–1999, average speeds are comparable with those from the Bravo mooring during 1994–1996. Unfortunately these additional moorings are not well suited for the study of coherent eddies since they are equipped with only one or occasionally two instruments, and therefore cannot resolve the vertical structure of the water column. The additional moorings were only in place at one or two locations each year (see Table 1); with at most three contemporaneous measurements (counting K1 and Bravo together) available, the moorings are not suitable for a discussion of spatial variability. The mooring study (Sections 3 and 4) will therefore focus on the densely-instrumented Bravo / K1 moorings, leaving spatial variability to be addressed using satellite altimetry in Sections 5–6.

2.3. Water mass structure and variability

Hydrographic surveys are invaluable in describing the temporal and spatial variability of water mass properties. Every May or June since 1990 the Bedford Institute of Oceanography has occupied the AR7W WOCE line (Fig. 2), stretching across the center of the Labrador Sea from Labrador to Greenland, sometimes together with other hydrographic lines. Additionally, three sets of hydrographic data (October–November 1996, February–March 1997, and January–February 1998, all of which included the AR7W line) were taken in other seasons (by various research groups), allowing a description of seasonal variability.

Orientation as to the major water masses is provided by a section of potential temperature (Fig. 6) from February 1997 along a more northern line paralleling the AR7W line (see Fig. 2). Deep convection is occurring at the time of the section, with differences in mixed layer depths of ~500 m across the Labrador Sea interior. Old Labrador Sea Water (2.9–3°C) fills the basin at middepths, with a strong bottom stratification due to Northeast Atlantic Deep Water (~2–2.5 km) and Denmark Straight Overflow Water (beneath ~2.5 km). A core of warm, salty Irminger Water is visible north of 61°N and above about 700 m depth. This potential temperature (θ) / salinity (S) core is associated with a deep boundary current, generally trapped shoreward of the three kilometer isobath, which moves northwestward (into the page) on the Greenland side and southeastward on the Labrador side. Above the Irminger Current lies the West Greenland Current (which becomes the Labrador Current as it reaches the Labrador coast), its extremely buoyant fresh water providing a barrier to convective mixing on the Greenland side (Pickart et al. 2002). While an Irminger Water core and a portion of the Labrador Current are generally visible on the Labrador side in the spring, in this late winter section there is a strong asymmetry between the two sides of the gyre.

To examine the interannual variability of the Labrador Sea water column using the springtime AR7W sections, a representative profile for each year is formed by averaging over all hydrographic casts extending to at least 3300 m, after rejecting a handful of casts likely to be contaminated by eddies or by the edge of the boundary current (see Appendix A for details). This results in mean profiles of potential temperature and salinity, and the potential density determined by these, for each year from 1990 through 2000 with the exception of 1991 which is not currently available. It is then possible to estimate the depth of convection for each intervening winter by examining the year-to-year change of isopycnal thickness, as discussed in Appendix A.

Depth-time plots of the mean interior Labrador Sea salinity and potential temperature are shown in Fig. 7, together with the estimated depth of convection. From a hydrographic point of view the 1990's divide into two periods with a split between the winters of 1995 and 1996. In the earlier period, convection reached 2 km or more, while in the later period the estimated depth was ~1–1.5 km. As a result, the mid-depth (~200–2000 m) water column observed in the spring sections was vertically homogeneous until 1994, after which a deep stratification begins to develop. Isotherms drop down from 1994 onward, as the water column undergoes a warming of over 0.5°C in the top 500 m. While the trend after 1994 is towards warming throughout the upper 2 km, the salinity trend changes sign at about one kilometer depth, with the upper water column becoming increasingly fresh. Above one kilometer depth the water column becomes less saline by 0.01 psu (practical salinity units) or more, while in the 1–2 km depth range a salinity increase of twice that is observed. Changes beneath about 2200 m, while important in their own right, are minute in magnitude compared with those in the upper water column.

The depth of convection is also shown in Fig. 3h (squares), and exhibits a transition beginning in 1996 from relatively deep (~2 km) to relatively shallow (~1 km) convection. Notice that the relationship between the depth of convection and the surface heat flux (Fig. 3d) is not straightforward. The shallow convection of 1996 appears to be due to the exceptionally

weak heat fluxes during that winter, but the relatively strong winter of 1997 only increased the depth of convection by a few hundred meters. The relationship between the depth of convection and the mooring currents is also interesting. The years of the deepest convection during which the mooring array was present, 1993–1994 and 1994–1995, are also the years of weakest currents, while the strongest currents at the Bravo / K1 mooring occurred during 1998–1999 coincident with the shallowest convection of the 1990's. This is not what one would expect from a convectively-forced region.

The vertical structure of restratification, with warming and freshening in the near-surface layer and warming and salinization at middepths, is emphasized in Fig. 8. This pattern apparently reflects the competition of deep lateral mixing, bringing warm and salty Irminger Water into the Labrador Sea interior, and shoaling convection which concentrates the influence of near-surface freshwater fluxes. Between 1994 and 1999, a "sinking" of isopycnals results in a thick pycnocline between 400 m and 2 km, all but erasing the ~1.5 km thick lens of nearly unstratified Labrador Sea Water observed every spring from 1990 to 1995.

The changing density structure has implications for dynamics as well. Shown in Fig. 8d is the horizontal structure function of the first linear baroclinic mode. In the early 1990's the nearly homogeneous upper 2 km could support little shear, leading to a flat structure function above ~2.3 km. By 1999, the first baroclinic mode was nearly linear with depth, with the difference between the upper convected water mass and the deeper overflow waters having almost disappeared. The deformation radius associated with the first mode, however, is nearly constant in time at approximately 7 km.

2.4. Heat content variability

The negative heat balance seen in Fig. 3d implies that to reach a steady-state, heat must be entering the Labrador Sea interior water column through lateral exchange. This section presents evidence for the annual and interannual variability of those fluxes.

Examining dozens of P-ALACE (Profiling Autonomous Ocean Lagrangian Circulation Explorer) floats in the interior Labrador Sea, Lavender et al. (2002) reported an anomalous warming of the ocean during April–May 1997 relative to expected NCEP fluxes. This result will be extended here. Every month from February to November 1997 there were between 19 and 140 floats in the "convection region", bounded by 59° N on the north, 51° W on the east and the 3000 m isobath on the south and west. The floats profile the temperature of the water column to 1300 m roughly every ten days. From in situ temperature, potential temperature can be derived to a very good approximation by choosing a constant reference salinity. The water column heat content $H(z)$ can then be found from integrating the potential temperature profiles $\theta(z)$

$$H_{1300} = \rho_o c_p \int_{-1300}^{0} \theta(z')\, dz'$$

where $\rho_o = 1000$ kg m^{-3} is a reference density, $c_p = 4000$ J kg^{-1} °C^{-1} the specific heat of water at constant pressure, and z is positive upward.

Finding the heat content for each P-ALACE profile and averaging by month leads to the heat storage estimate shown in Fig. 3g (thick gray line), offset so that the March value equals zero. Also shown are the mean values and standard deviations of the heat content at 1300 m for two hydrographic cruises (triangles), in each case considering all profiles within the "convection region", offset by the same amount used to offset the P-ALACE curve; these match well the contemporaneous P-ALACE measurements.

The observed heat content can be compared with that expected based on the adjusted (as discussed in Section 2.1) NCEP surface heat fluxes alone. The heat content change due to those

fluxes (thin black line) nearly exactly balances the P-ALACE estimated heat content in the upper 200 m (thick dotted line), yet that is only about 1/2 of the total heat gain between the surface and 1300 m. The difference between the total P-ALACE heat content and the NCEP surface fluxes can be converted to a monthly-mean rate of warming the Labrador Sea interior; this is an estimate of the inward heat flux due to oceanic processes. The estimated lateral flux peaks in April–May at 200 W m^{-2} (Fig. 3c, thick dashed line). Since the errors associated with the wintertime NCEP heat fluxes are O(10) W m^{-2}, this is likely to be a physically meaningful signal.

The vertical structure of the springtime warming is shown in Fig. 9. Between February and March, deep convection erodes the warm water beneath 500 m, leading to a vertically homogeneous profile. A deep warming then begins, increasing temperatures over the top ~700 m by more than 0.1°C during each of the next two months. Note that by May the water column beneath 700 m again matches the profile from the preceding February. By the end of May, nearly one gigajoule per meter squared of warming has occurred, with only a minor contribution apparently due to surface fluxes. The deep restratification is both rapid and large in magnitude.

While it is not known if the estimated lateral heat flux curve produced during 1997 is representative in form or in magnitude, the idea of a rapid restratification following deep convection is consistent with an earlier mooring study (Lilly et al. 1999). In that paper θ/S diagrams were used to deduce two phases to the restratification, a "fast" phase occurring 1–2 months following deep convection, and a weaker "background" phase that continued to warm the deep water column until the following winter's convection.

Interannual variability of the heat content, formed from integrating the springtime mean interior hydrographic profiles to 2000 m, is shown in Fig. 3h. The values move erratically until 1996 at which time a steady warming begins, continuing until 1999. Again the relationship with surface fluxes (Fig. 3d) is perplexing, since the largest heat storage gain of the 1990s occurs between June 1996 and June 1997, a time period during which the ocean experienced relatively large surface heat loss.

More information about the nature of this warming can be found by partitioning it into two terms. As described in Appendix B, the heat storage at a given depth $H(z)$ can be decomposed as

$$H(z) = \mathbf{H}(z) + H^*(z)$$

where $\mathbf{H}(z)$ is the surface heat loss required to convect to depth z, and the residual $H^*(z)$ is the heat content left behind in the convected product. The "available" heat storage $\mathbf{H}(z)$ is proportional to buoyancy loss when nonlinearities are neglected, while $H^*(z)$ is analogous to "spiciness" and cannot be removed from the water column by local convection. This partitioning requires a choice about the ratio of latent to sensible heat loss (see Appendix B). An illustration of these definitions using a typical profile from the springtime Labrador Sea is shown in Fig. 10.

The values of these two quantities at 2 km are shown in Fig. 3h for the mean Labrador Sea interior profiles. Here one sees that the residual $H^*(z)$ is essentially constant from 1993–1999 except for a one gigajoule per meter squared increase between June 1996 and June 1997. Since $H^*(z)$ is unaffected by changes in magnitude of the surface heat loss, this increase is likely to be the result of lateral fluxes. Two other years stand out, 1992–1993 and 1999–2000, during which substantial decreases in $H^*(z)$ are evident.

Annual average lateral heat fluxes were estimated as a residual from the NCEP fluxes and the hydrographic heat content (Fig. 3d). Values range between a minimum of 16 W m^{-2} in 1994 and 85 W m^{-2} in 1997, with a mean over this time period of 48 W m^{-2}. The standard deviation of the estimated lateral fluxes is 23 W m^{-2}, so that the 1997 value is an excursion

from the mean of close to twice the standard deviation. In general lateral fluxes after 1997 are estimated to be higher than in 1993–1996.

It is tempting to link the extremely large estimated lateral heat fluxes during June 1996–June 1997 with the relatively shallow depth of convection during that year, despite a very strong surface heat loss. However, from the heat content partitioning (Fig. 3h) one sees that 0.84 GJ m^{-2} or 27 W m^{-2} of the 1997 warming is associated with changes in the residual heat content, and therefore is unable to influence the stability of the water column against convection. The remaining 1.81 GJ m^{-2} or 57 W m^{-2} is less than one standard deviation away from the mean and thus is not exceptional in a statistical sense. Therefore the bulk of the anomalous lateral heat flux (relative to the mean) in 1997 resulted in a warming and salinization of the water column without a change in its resistance to convection.

Nevertheless, it still appears that the additional 1997 lateral heat flux had a noticeable impact on the depth of convection. Because the slope of the available heat storage $\mathbf{H}(z)$ versus z is roughly three times as large in the stratified layer beneath $\sim$ 2 km as in the weakly stratified layer above it, a given amount of excess lateral heat flux will have a larger impact on reducing the depth of convection when convection is already shallow than when it is deep. The 57 W m^{-2} of warming during 1997 not associated with the change in the residual heat content represents a 16 W m^{-2} increase over the mean lateral heat flux excluding 1997 of 42 W m^{-2}, equivalent to an extra 0.5 GJ m^{-2}. In the middle water column one has a slope of $\mathbf{H}(z)$ versus mixed layer depth of about 0.3 GJ m^{-2} km^{-1}. Assuming that half of the excess 0.5 GJ m^{-2} arrived prior to the end of deep convection, and therefore would have contributed to reducing the depth of convection, one obtains a decrease in the depth of convection of $\sim$ 200 m. While this estimate is certainly rough, it appears that the depth of convection was somewhat shallower in winter of 1997 than it would have been with "average" lateral fluxes.

2.5. Summary

The annual cycle and interannual variability of surface forcing [from NCEP fluxes, adjusted as per Renfrew et al. (2002)], current meter speed, and water mass properties were examined. Combining the water mass measurements with the NCEP fluxes, lateral (oceanic) heat fluxes were also estimated. The main results for the annual cycle are as follows:

- Surface heat loss peaks in January at 200–300 W m^{-2}, and crosses through zero around April as solar insulation begins to warm the ocean.
- A current speed maximum occurs in May, with elevated values during April–June compared to the rest of the year; this maximum is much stronger at the Bravo / K1 moorings than at the other moorings, and is seen (not shown) during both the earlier and later parts of the time period.
- In 1997 P-ALACE float profiles showed a deep and sudden springtime warming, with estimated lateral fluxes peaking in April–May at 200 W m^{-2} and accounting for one-half the $\sim$2 GJ m^{-2} total ocean heat gain during March–September 1997.

In contrast to the observed annual cycle, a detailed numerical study of deep convection in the presence of eddies (Legg & McWilliams 2001) shows domain-averaged kinetic energy levels rising as buoyancy forcing continues, then leveling off or decaying within days after buoyancy forcing ceases. Thus the observed annual cycle does not support the notion of the Labrador Sea as an isolated convection region. In interannual variability, the following results were found:

- Wind stress forcing and surface heat loss were generally stronger during 1991–1993 than during later years, with the exception of June 1996–June 1997 which also had large surface

heat losses.

- Two distinct time periods are apparent, the deeply convected early part of the 1990's (1991–1995) and the shallowly convected later part (1996–2000).
- During the latter time period, the water column warmed throughout the upper 2 km, but became less saline above and more saline below the ~1 km depth of convection.
- The average rate of warming due to lateral fluxes was estimated to be 48 W m^{-2} between the surface and 2 km during the 1990s, roughly a third larger than the average cooling rate due to surface fluxes of 35 W m^{-2}; the remaining 13 W m^{-2} is the average rate of net warming of the water column.
- Current speeds tripled at the Bravo / K1 mooring during the time period 1994–1999 from ~10 cm s^{-1} to ~30 cm s^{-1}, but remained at ~10 cm s^{-1} at other moorings in the Labrador Sea interior.
- The very large lateral heat flux anomaly during 1997, double the mean excluding 1997 of 42 W m^{-2}, primarily (~60% of 42 W m^{-2}) resulted in a warming and salinization of the water column without a change in its stability against convection; nevertheless the remainder was estimated to have reduced the depth of convection by roughly ~200 m.

Here again a mismatch between forcing and the ocean's behavior is observed. The high speeds observed at the Bravo / K1 moorings during 1997–2000 do not coincide with increased wind stress or heat flux forcing relative to 1994–1997; indeed, the weaker currents occurred when the depth of convection was deeper. Generally speaking, the variability of the currents and the estimated lateral heat fluxes points to the potential importance of the boundary current system in influencing the properties of the Labrador Sea interior. With these observed large-scale changes providing a context, the focus will now be turned to small-scale features.

3. Wavelet-based detection of isolated velocity anomalies

3.1. Introduction and motivation

This section develops the intuitive and technical foundations necessary for identifying coherent eddies in mooring current meter data, leading to the five-year eddy census presented in the next section. Readers who are not interested in these technical details may skip directly to Section 4 without compromising the logical flow of the paper.

A coherent eddy is generally defined as a long-lived, isolated potential vorticity anomaly. However, this definition is impossible to apply to mooring observations; instead, one must resort to comparing observed signals with those expected to be associated with such a structure. The range of possible forms coherent eddies may take in moored instrument records is very broad (Lilly & Rhines 2002, Lilly 2002) owing to the variety of eddy types together with the various scenarios in which an eddy may be observed by a mooring. Additionally, other phenomena — such as mooring towdown during times of intense currents— may exhibit an appearance very similar to that of an advected eddy. Therefore, the process of locating eddies in mooring observations necessarily involves a level of judgment.

The expected currents at a mooring due to an advected eddy were examined by Lilly and Rhines (2002) [LR], and those due to multiple and dipolar eddies by Lilly (2002). An important tool for the comparison of data with model predictions turns out to be the velocity hodograph (a plot of u versus v), which reveals details of eddy-like current anomalies not apparent in, say, stick-vector plots or progressive vector diagrams. Searching through data from the Bravo

mooring during June–November 1994, LR identified six events having hodographs and vertical structures consistent with those expected for coherent eddies.

This approach to finding eddies in mooring data can be improved in two major ways. First, it would be valuable to find a representation of eddy currents which reveals the sort of structure seen in the hodographs, but which also displays the temporal evolution of the currents. Second, it is desirable to have an objective "first guess" criterion for what is or is not an eddy. Such a criterion would facilitate the analysis of a large amount of data, and would also lend a degree of repeatability to the study. Events identified by this method could then be examined on a case-by-case basis, employing the geometrical analysis of LR to sort eddies from non-eddies. It should be pointed out that the goal is to create a practical definition, based on some expected feature of an advected coherent eddy, rather than a statistical definition founded on a stochastic model.

Creating an objective definition of an eddy-like feature is difficult. Temperature or salinity anomalies at a given depth are not a good indicator, due to the large magnitude annual and interannual variability in these fields (discussed in Section 2). Furthermore, a water mass anomaly is not a necessary property of a coherent eddy; rather, the association between water mass anomalies and potential vorticity anomalies is an empirical result based on studies in other parts of the world ocean, and may or may not be appropriate in the Labrador Sea.

It is therefore preferable to use some feature in the currents themselves as a definition of a coherent eddy. Traditional Fourier analysis does not prove useful here. A velocity time series in an eddy field will contain structures at many temporal scales, as coherent eddies will not only vary in size but will move past a mooring at different speeds. The Fourier spectrum averages these structures together, resulting in little more information than a spectral slope on the basis of which an organized eddy field cannot be distinguished from red noise. In particular, the two-dimensionality of the eddy currents, reflecting the two-dimensional structure of the eddies themselves, is lost.

Simple time-domain statistics are similarly of little usefulness. An eddy event is not an isolated excursion in a time series, such as "bad" data point, which one can locate using a statistical criterion. Rather, the finite duration of the event, and the structure of the currents during that period, are crucial elements one wishes to capture in a "definition". This suggests that statistics over some smoothed or filtered version of the time series could be employed. However an eddy will be compressed or stretched out in time depending on the magnitude of the advecting flow, thus no single choice of filter duration is appropriate.

The analysis of structures which are neither isolated events nor sinusoids is the domain of the wavelet transform. This is essentially a "stack" of bandpasses, each using an increasingly stretched-out version of some suitably chosen filter, which decomposes the variability of the time series as a function of both time and "scale". While the rapidly-growing field of wavelet analysis is proving to be a powerful and flexible technique, for example, in the analysis of multivariate seismic (Lilly & Park 1995, Bear, Pavlis & Bokelmann 1999) and climatic (Park & Mann 2000) time series, applications to oceanographic time series seem to have received relatively little attention.

In this section a modified version of the wavelet transform appropriate to an eddy-rich vector time series is developed, paralleling to some extent work on the Fourier analysis of vector time series (Gonella 1972, Mooers 1973). A wavelet-based algorithm is developed which examines the "topography" of the time-scale plane and automatically identifies eddy-like velocity events. These events are then examined in detail and classified as eddies or non-eddies, providing the starting place for the five-year eddy census presented in the next section.

3.2. The continuous wavelet transform for vector time series

The continuous wavelet transform decomposes the variability of a time series into contributions from various times and various scales; extensive discussions of the wavelet transform and its applications can be found elsewhere (Mallat 1999, Farge 1992). In this subsection a modified version of the standard wavelet transform is derived and is found to have useful properties for examining eddy currents. The next section uses the wavelet transform to create a definition of an "eddy-like" event.

3.2.1. Definition

The wavelet transform of a time series $x(t)$ with a wavelet $g(t)$ is defined as

$$\mathcal{W}^{(n)}[x](\tau, a) \equiv \int_{-\infty}^{\infty} x(t)\, \frac{1}{a^n} g^* \left(\frac{t-\tau}{a} \right) dt \tag{3.1}$$

where the asterisk denotes the complex conjugate, n is a normalization exponent, and the superscript (n) is used here to reflect the dependence of $\mathcal{W}$ on the choice of normalization. The wavelet $g(t)$ is a function having finite energy

$$\int_{-\infty}^{\infty} |g(t)|^2 dt < \infty$$

and zero mean

$$\int_{-\infty}^{\infty} g(t) dt = 0 \tag{3.2}$$

and may be either real or complex. An analytic wavelet is a complex-valued wavelet the Fourier transform of which vanishes for negative frequencies. When $n = 1/2$ the squared modulus of an analytic wavelet transform of a real-valued signal represents an energy density local to a point in time and frequency (or scale)

$$S[x](\tau, a) \equiv |\mathcal{W}^{(1/2)}[x](\tau, a)|^2 \tag{3.3}$$

and is known as the scalogram. This is the time-varying wavelet analogue to the Fourier spectral density.

The wavelet transform (3.1) has a more compact form in terms of the convolution operator[3]

$$s_1 * s_2(\tau) \equiv \int_{-\infty}^{\infty} s_1(t)\, s_2(\tau - t)\, dt$$

as

$$\mathcal{W}^{(n)}(\tau, a) = x \star \bar{g}_a^{(n)}(\tau)$$

where $\bar{g}(t) \equiv g^*(-t)$ and $g_a^{(n)}(t)$ is defined as a rescaled version of $g(t)$

$$g_a^{(n)}(t) \equiv a^{-n} g\left(\frac{t}{a}\right).$$

The wavelet transform of $x(t)$ with $g(t)$ is therefore the convolution of $x(t)$ with rescaled and time-reversed versions of the wavelet. However for an analytic wavelet, $\bar{g}(t) = g^*(-t) = g(t)$, so that the wavelet transform

$$\mathcal{W}^{(n)}(\tau, a) = x \star g_a^{(n)}(\tau)$$

[3]Equivalently, (3.1) could be rewritten as an inner product or a correlation operation.

is just the convolution of $x(t)$ with $g(t)$ itself.

Both the wavelet scalogram and the moving-window Fourier transform or spectrogram describe the time-frequency structure of a signal, but the way in which they cover the time-frequency plane is different. In the spectrogram the width of the time-frequency window is independent of frequency, whereas in the scalogram the window width is inversely proportional to the frequency. The latter is a natural choice when one expects to see rescaled versions of a signal having a known "wiggliness" or a self-similar structure across scales.[4]

3.2.2. The amplitude spectrum

Typically the energy normalization $n = 1/2$ is used in (3.1), ensuring that the projection of the wavelet onto itself is independent of scale. Instead the normalization $n = 1$ will be used here. With this "amplitude normalization", stretching or compressing a signal in time results in a wavelet transform that is stretched or compressed in both time and in scale

$$\mathcal{W}^{(1)}[x(\alpha t)](\tau, a) = \mathcal{W}^{(1)}[x(t)](\alpha\tau, \alpha a) \tag{3.4}$$

without change in amplitude; we will refer to this property as "dilation invariance". Generally $\log(a)$ rather than a is used as the scale axis, so stretching or compressing a signal will translate its wavelet transform along the log-scale axis by $\pm\log(\alpha)$. This property implies that the peak magnitude of an advected feature's wavelet transform is independent of the advection speed.

With the n=1 normalization, rescaling the wavelet by varying a merely translates the wavelet's Fourier transform along the log-frequency axis, without change in form or in magnitude. The wavelet transform therefore becomes a set of complex-valued bandpass operations, with the spectral width of the bandpass decreasing towards large scales. It can be shown (Section 3.2.5) that such a complex-valued bandpass returns the slowly-varying envelope of variability of a particular Fourier component. This suggests interpreting the $n = 1$ transform as a measure of the local value of the Fourier spectrum near a particular time τ and a particular "frequency" a^{-1}. By analogy with the wavelet "energy spectrum" or scalogram (3.3) one can define the "amplitude spectrum" as the modulus of a wavelet transform with $n = 1$

$$\mathcal{A}[x](\tau, a) \equiv |\mathcal{W}^{(1)}[x](\tau, a)| \tag{3.5}$$

which is a measure of the amplitude of signal variability local to a point (τ, a).

In what follows the superscript (n) of $\mathcal{W}$ will be dropped, and the amplitude normalization $n = 1$ will be used exclusively.

3.2.3. Choice of wavelet

Consider a real-valued and even window function $h(t)$, such as a Gaussian probability density function $(\sqrt{2\pi\sigma^2})^{-1}\exp\{\frac{-t^2}{2\sigma^2}\}$ where σ is the standard deviation. For convenience assume that the second derivative of $h(t)$ vanishes at $t = \pm 1$, corresponding to $\sigma = 1$ for the Gaussian. This marks the edges of a central portion of the window $t = [-1, 1]$ within which $h(t)$ has substantial amplitude.

An analytic wavelet can be constructed by using $h(t)$ as the envelope of a complex-valued sinusoid

$$g_{\tau,a}(t) = \frac{1}{a}h\left(\frac{t-\tau}{a}\right)\left(e^{2\pi i\tilde{f}(t-\tau)} + \delta\right) \tag{3.6}$$

[4]See Mallat (1999) for a discussion of the theoretical relationship between the scalogram and spectrogram as tilings of the time-frequency plane.

where $\tilde{f} \equiv \frac{1}{2}ma^{-1}$, m is the number of wavelengths of the sinusoid which fit inside the central portion of the window $t = [-a, a]$, and δ is a small real number necessary to enforce the zero-mean condition (3.2).

Since a convolution in the time domain is equivalent to a multiplication in the frequency domain, the wavelet transform with the amplitude-normalized wavelet may be interpreted as a succession of bandpass operations. The width of the bandpass in the frequency domain is inversely proportional to the scale a, hence larger scales are better resolved in the frequency domain.[5]

Generally a Gaussian window is chosen for $h(t)$, yielding the Morlet wavelet. However, the long tails of the Gaussian window lead to a poor time localization which can be problematic. A class of functions known as discrete prolate spheroidal sequences or DPSSs (Slepian 1978) are optimally concentrated in time and frequency, and so have found extensive application as data tapers in spectral analysis (Thomson 1982, Park, Lindberg & Vernon 1987, Percival & Walden 1993). The time-bandwidth product $P \equiv 2NW$, where W is the half-width of a spectral window within which the function is concentrated and N is the function's length, determines the tradeoff between time and frequency localization. Here the lowest-order DPSS with $P = 2$ will be used as the wavelet envelope $h(t)$, which will be referred to as a 2π envelope following the notation in the DPSS literature. This function is strictly zero outside of a time window corresponding to approximately $t = \pm 3.28$, where again the time axis is scaled so that the second derivative of $h(t)$ vanishes at $t = \pm 1$. Further, the window $h(t)$ is normalized so that the peak magnitude of its Fourier transform is unity, so that the wavelet transform at a given scale is exactly a (complex-valued) bandpass operation.

The number of oscillations within the central window of the wavelet is then set by the choice of m. Choosing $m = 2/3$ yields the wavelet shown in Fig 11b, the even and odd components of which are roughly similar to the parallel and perpendicular currents due to an advected eddy Fig 11a. This wavelet is "narrow" in time but "broad" in frequency. For this choice of wavelet, the wavelet transform at scale a corresponds to a bandpass of half-width $W = 0.35a^{-1}$ centered at frequency $\tilde{f} = \frac{1}{3}a^{-1}$. The ratio of the half-width to the central frequency $W/\tilde{f}$ is 0.90, so that the frequency resolution of these wavelets is quite poor.

3.2.4. Complex-valued time series

Consider a complex-valued time series

$$\xi(t) = u(t) + iv(t)$$

where u and v are the eastward and northward velocity components respectively. The complex-valued wavelet transform of a complex-valued time series contains four real-valued transforms which can be combined together into three sets of physically meaningful transform pairs, as with Fourier analysis (Gonella 1972).

The (u, v) component transforms will be denoted

$$\begin{aligned} \mathcal{W}_u[\xi](\tau, a) &\equiv \Re\{\xi\}\star g &= u\star(g_c + ig_s) \\ \mathcal{W}_v[\xi](\tau, a) &\equiv \Im\{\xi\}\star g &= v\star(g_c + ig_s) \end{aligned} \tag{3.7}$$

where g_c and g_s are the real (cosine-like) and imaginary (sine-like) parts of the wavelet, and the subscripts τ and a have been dropped; $\Re\{\xi\}$ and $\Im\{\xi\}$ denote the real and imaginary parts

[5]This increase in bandpass width toward high frequencies again highlights the difference between the Fourier and wavelet tilings of the time-frequency plane. Equivalently, one may say that the time-bandcenter product – the number of periods in the time window – is constant for a wavelet transform but increases towards high frequencies for Fourier analysis.

of ξ, respectively. Mathematically positive (counterclockwise) and negative (clockwise) rotating components are given by

$$\begin{array}{rclcl} \mathcal{W}_p[\xi](\tau,a) & \equiv & \xi\star\frac{1}{\sqrt{2}}g & = & (u+iv)\star\frac{1}{\sqrt{2}}(g_c+ig_s) \\ \mathcal{W}_n[\xi](\tau,a) & \equiv & \xi\star\frac{1}{\sqrt{2}}g^* & = & (u+iv)\star\frac{1}{\sqrt{2}}(g_c-ig_s) \end{array} \tag{3.8}$$

Finally a separation into locally even and locally odd components

$$\begin{array}{rclcl} \mathcal{W}_c[\xi](\tau,a) & \equiv & \xi\star\Re\{g\} & = & (u+iv)\star g_c \\ \mathcal{W}_s[\xi](\tau,a) & \equiv & \xi\star\Im\{g\} & = & (u+iv)\star g_s \end{array} \tag{3.9}$$

is also possible. All six component transforms are in general complex-valued. Following the definition of the amplitude spectrum (3.5), $\mathcal{A}_u$ will be understood to mean $|\mathcal{W}_u|$, etc.

Although the three transform pairs each have an analogue in Fourier analysis, it is interesting to point out that the cosine/sine pair takes on a new significance in the wavelet analysis. Due to the global nature of Fourier analysis the cosine and sine wavelet transforms rarely have different physical interpretations in oceanographic time series analysis. However whether a time-localized event is even or odd (or a mixture) is a fundamental property that can help distinguish coherent eddies from other features.

To measure the total amplitude spectrum of a complex-valued time series, it is inappropriate to use $\mathcal{A}[\xi] = |\xi\star g|$ since

$$\begin{array}{rcl} \mathcal{A}[\xi](\tau,a) & = & \sqrt{(\xi\star g)(\xi\star g)^*} \\ & = & \sqrt{\mathcal{A}_u^2+\mathcal{A}_v^2+2\Im\{\,\mathcal{W}_u\,\mathcal{W}_v^*\,\}} \end{array}$$

includes a cross-term which amounts to a wavelet correlation between the u and v time series.[6] $\mathcal{A}^2[\xi]$ is the wavelet equivalent of Mooers' (1973) "inner-autocovariance".

Instead one can define the total amplitude spectrum $\mathcal{T}[\xi]$ of a complex-valued time series in terms of the component amplitude spectra as

$$\begin{array}{rcl} \mathcal{T}[\xi](\tau,a) & \equiv & \sqrt{\mathcal{A}^2[\Re\{\xi\}]+\mathcal{A}^2[\Im\{\xi\}]} \\ & = & \sqrt{\mathcal{A}_u^2[\xi]+\mathcal{A}_v^2[\xi]}. \end{array}$$

The total spectrum $\mathcal{T}$ can be represented equivalently in terms of any of the three transform pairs since

$$\mathcal{T}[\xi](\tau,a) = \sqrt{\mathcal{A}_p^2[\xi]+\mathcal{A}_n^2[\xi]} \tag{3.10}$$

$$= \sqrt{\mathcal{A}_c^2[\xi]+\mathcal{A}_s^2[\xi]}, \tag{3.11}$$

as substitution of the definitions (3.8, 3.9) into (3.10, 3.11) verifies in few lines of algebra. The functions $\mathcal{T}$, $\mathcal{A}_c$, $\mathcal{A}_s$, $\mathcal{A}_p$, and $\mathcal{A}_n$ (as well as $\mathcal{A}$ itself) are all independent of rotation, i.e. $\mathcal{T}[e^{i\phi}\xi] = \mathcal{T}[\xi]$ for all angles ϕ.

3.2.5. A "wave-packet" interpretation

For the case of a "wave-packet" signal the total wavelet transform $\mathcal{T}$ has a simple physical interpretation, as will now be shown; see Lilly (2002) for additional details. A wave-packet consists of a "carrier wave" modulated by a low-frequency envelope. Consider a linearly polarized (near-buoyancy) wave packet

$$s_1(t) = u + iv = b(t)cos(2\pi f_o t) + i0$$

[6] In their paper on rotary wavelet analysis, Liu and Miller (1996) omit this correlation term (see their Equation 9).

as well as a circularly polarized (near-inertial) wave-packet

$$s_2(t) = u + iv = b(t)e^{-2\pi i f_o t}$$

where $b(t)$ is a real-valued low-frequency envelope. At the scale $a_o \equiv \frac{1}{2} m f_o^{-1}$ for which the wavelet frequency $\tilde{f}$ equals the wave frequency f_o, the total wavelet transform of the linearly polarized wave packet is to a very good approximation

$$\mathcal{T}[s_1](\tau, a_o) \approx \frac{1}{2}\left|\int_{-\infty}^{\infty} b(t) h_{a_o}(t-\tau)dt\right| \tag{3.12}$$

while that of the circularly polarized wave packet becomes

$$\mathcal{T}[s_2](\tau, a_o) \approx \frac{1}{\sqrt{2}}\left|\int_{-\infty}^{\infty} b(t) h_{a_o}(t-\tau)dt\right| \tag{3.13}$$

provided the Fourier transforms of $b(t)$ and of $h(t)$ are sufficiently localized; for convenience a rescaled version of the wavelet envelope $h_a(t) = \frac{1}{a} h\left(\frac{t}{a}\right)$ has been introduced. Note that the linearly-polarized wave packet and circularly polarized wave packet transforms are identical except for a factor[7] of $1/\sqrt{2}$.

For both the linear and circularly polarized wave-packet, the total wavelet transform $\mathcal{T}$ at f_o is simply the magnitude of the wave-packet envelope smoothed by the wavelet envelope. The convolution with the complex-valued wavelet effectively removes the carrier signal. Simple relationships between the various component transforms are also found to exist and are discussed in Lilly (2002).

3.3. Application to eddy-rich time series

The three decompositions of the wavelet transform of a complex-valued time series introduced in Section 3.2.4 would each be most applicable in different situations: the (u, v) component transforms in a highly polarized setting such as in a boundary current, the the rotary transforms for studies of internal waves, and as it turns out, the even/odd pair for eddy-rich time series. This pair "unwraps" the complex-valued curve traced out by the currents into locally even and locally odd contributions at each moment, partitioned as a function of scale.

3.3.1. An isolated eddy

Before turning to data, it is useful to explore the behavior of these transforms on a sample time series. The well-known eddy solution

$$v_\phi = u_o \begin{cases} \dfrac{r}{r_o} & r < r_o, \\ \dfrac{r_o}{r} & r > r_o \end{cases} \tag{3.14}$$

consists of solid-body rotation within the eddy core ($r < r_o$) and r^{-1} decay elsewhere, and is known as the Rankine vortex. Here the "rim current" u_o is the azimuthal velocity component at r_o, the edge of the eddy's core, and is positive for a cyclone and negative for an anticyclone. In steady, barotropic, and quasigeostrophic dynamics, these currents coincide with a uniform potential vorticity anomaly inside $r < r_o$. The Rankine vortex is arguably the simplest possible eddy model having a finite vorticity core. While this model is physically unrealistic for a number of reasons— most notably its infinite horizontally-integrated kinetic energy— it will be found to be adequate for the present discussion.

[7]The equation corresponding to (3.13) in (Lilly 2002) (his 3.22) erroneously omits the factor of $1/\sqrt{2}$.

The wavelet transform of the Rankine vortex sliced along a line midway between the eddy center and eddy rim, shown in Fig. 12, consists of a maximum in the odd transform flanked by two maxima of the even transform. The sudden changes in acceleration at the eddy edges are manifested as near-discontinuities in the odd component $\mathcal{A}_s$ and as "cusps" of the even spectrum $\mathcal{A}_c$ extending toward small scales. The ridges of $\mathcal{A}_c$ and the edges of the $\mathcal{A}_s$ "plateau" both converge onto the eddy edges at small scales. The total amplitude spectrum is smoothly varying, with a single maximum centered on a scale virtually identical to the width of the eddy core.

This even-odd-even "tripole" is a robust and characteristic feature of coherent eddies advected past the mooring under different scenarios. Specifically, this pattern is invariant to direction of the advecting flow, while a change in the magnitude of the advecting flow will merely stretch or compress the pattern along the time axis and shift it along the scale axis (see Section 3.2.2). Further, the basic even-odd-even pattern does not depend on the location of the slice, since the eddy signal perpendicular to the mean flow (which is odd in time) is always at least twice as large as that of the parallel (even) signal. Other types of coherent eddies, such as a Gaussian streamfunction profile (not shown), result in wavelet transforms similar to those of the Rankine vortex.

Lilly (2002) also examined the currents due to advecting pairs of same-signed Rankine vortices in a constant background flow, as well as those due to self-advecting dipoles. The even-odd-even patterns of transform maxima seen in isolated eddy case are generally also observed for the mutually advecting eddies, with additional low-frequency structures emerging which are partly due to the curvature of the eddy trajectories. For the case of a self-advecting dipole sliced near its center line, the dominant signal is an odd-even-odd pattern, the opposite of that observed for advected coherent eddies.

3.3.2. Labrador Sea eddies

The continuous wavelet transform for 1010 m current meter at the Bravo mooring during the summer of 1994 is shown in Fig. 13. Although the speed time series does not at first glance appear to contain clear eddy signals, a number of even-odd-even tripoles similar to those observed for the Rankine vortex may be observed. Indeed, this time period was found in LR to contain five events, marked by vertical lines in the speed figure, having eddy-like currents and θ/S structure.

The locations on the time-scale plane of eddy-like even-odd-even patterns agrees well with the locations of confirmed eddy cores as reported by LR (Fig. 13b,c,d). For instance, the short-duration event near yearday 180 appears to be part of the background noise in the speed time series, but has a discernible even-odd-even wavelet transform tripole. All but the smallest and weakest of the five confirmed eddies correspond to wavelet transform features similar to the pattern of the idealized eddy. One asymmetric eddy-like wavelet pattern (near yearday 210) not associated with a confirmed eddy appears from its hodograph (not shown) to be an eddy "near-miss" which did not intersect the θ/S core. The sixth event reported by LR occurs much later than the others and so is not shown in Fig. 13, but is also detected in the wavelet analysis.

The impression of the time series obtained by examining the wavelet transform therefore appears to agree well with the more exhaustive process of isolating the hodographs and vertical slices of individual events. This suggests the wavelet transform could be used to create an automated "first guess" marking potential eddies in a time series.

3.3.3. Five years of Labrador Sea data

In Section 2.2, nearly continuous velocity and temperature records from the Bravo / K1 mooring were presented. Speed time series and stickvectors are shown in Fig. 14 for the depth

corresponding to the maximum eddy currents during each year (see caption for depth values). An unsteady and apparently eddy rich flow is seen, the magnitude of which increases dramatically during this time period. Annually a period of stronger currents and enhanced high-frequency variability is apparent during March–April, within which period the convective mixed layer typically reaches its deepest extent and lateral restratification begins (Lilly et al. 1999).

The total transform $\mathcal{T}$ (Fig. 14e,f) maps out the rich detail of the currents across the time-frequency plane. The tidal/ inertial wave band shows up as a horizontal stripe of enhanced transform amplitude at the top of the image. The coherent eddies identified in Fig. 13 are now tall, slender wedges of enhanced amplitude. Many other similar isolated maxima are apparent, mostly occurring at scales between one and ten days, indicating a localized organization of the currents at a given scale. There is a tendency for events to be of larger scale (that is, longer duration) and larger magnitude during the last two years of the time series. Seasonal variability is apparent, with an increase in transform amplitude at small scales (especially at scales smaller than $\log_{10}(a) \sim 0.5$) tending to occur during March and April. During these months, the total transform has a disorganized appearance, with isolated events blending into a background of high-frequency activity. At large scales, greater than $\sim$ 10 days, few isolated maxima are apparent and broad bandlike structures are sometimes seen.

It is evident that the continuous wavelet transform plots fulfill one of the goals of this section, namely, to find a representation of eddy-rich time series which reveals both localized structures as well as temporal variation. The change in amplitude and scale of the isolated maxima of $\mathcal{T}$ throughout this time period is suggestive of interannual variability of an underlying eddy field. This display of the time/frequency content of the time series provides the starting place for the eddy census.

3.3.4. Definition of an isolated velocity anomaly

Creating an appropriate objective criterion for locating velocity signals due to advected eddies is difficult owing to the multiplicity of eddy forms as well as to the presence of non-eddy variability. Here we use the wavelet transform to form a definition that is independent of the advection speed and direction, and can separate an eddy signal from other current variability at both smaller and larger scales.

A modulus maximum of a wavelet transform $\mathcal{W}$ is defined (Mallat 1999) as a point (τ_o, a_o) such that $|\mathcal{W}(\tau_o, a_o)|$ is a local maximum with respect to variations in τ. A continuous line of modulus maxima across the time-frequency plane is called a maxima line, denoted $\tau_M(a)$, and traces the maximum signal due to a given structure across scales. The smoothing nature of the wavelet transform implies that the number of distinct maxima lines will decrease towards large scales so that maxima lines will tend to converge. Here the maxima-line peak is defined as the scale a_o at which $\tau_M(a)$ is a maximum with respect to a; a maximum-line peak is obviously a local maximum of $|\mathcal{W}(\tau_o, a_o)|$. The maxima-lines and maxima-line peaks correspond to "ridges" and "peaks" of the wavelet transform "topography", respectively, as seen in Fig. 13d.

A definition of an isolated velocity anomaly is a non-terminal maxima-line peak having a magnitude greater than a certain cutoff χ_a

$$|\mathcal{T}(\tau_M(a_o), a_o)| > \chi_a \tag{3.15}$$

and which rises at least a certain amount χ_b from the line's minimum value at smaller scales

$$|\mathcal{T}(\tau_M(a_o), a_o)| > \chi_b - \min\{|\mathcal{T}(\tau_M(a < a_o), a < a_o)|\}. \tag{3.16}$$

The latter is a crude "frequency localization" criterion that rejects weak peaks along energetic but flat maxima lines; such peaks are common during the convection season (March–May)

and are considered noise here. Finally since there may be other peaks at larger scales due to interference patterns, only the smallest-scale peak along a given line will be considered, beginning at $a = 1/2$ day ($\log_{10}(a) \approx -0.3$) just above the wave band. This last criterion reflects the physical belief that eddies are the smallest-scale organized features in these time series.

Provided that the advection velocity vary slowly relative to the duration of the feature's passage, this definition should detect eddies having a variety of forms (Gaussian, Rankine, etc.), as well as other localized features such as fronts or self-propagating dipoles. The wavelet definition is independent of the duration of the eddy, and therefore of both the eddy's size and the advection speed, as well as of the direction of the advecting flow. Although one does expect to have non-eddies in the set of wavelet-identified velocity anomalies ("false positives"), eddies not identified as velocity anomalies ("false negatives") are expected to be rare provided the advecting velocity varies slowly with respect to the duration of the eddy.

Locations on the time-scale plane of velocity anomalies exceeding the cutoff values $\chi_a = 6$ (corresponding to an azimuthal velocity of about 12 cm s^{-1}) and $\chi_b = 2$ are shown in Fig. 13, together with locations and durations of events identified by LR being as coherent eddies. Of the five eddies reported by LR during this time period, all but the weakest are detected by the wavelet method, with one wavelet event near day 210 being judged a non-eddy due to an absence of a θ/S core. The scales at which the isolated maxima occur are generally very close to the apparent duration of the eddy cores. Overall the agreement is very good and suggests the wavelet definition is useful as an objective first criterion in locating advected eddies.

3.4. Summary

In this section the continuous wavelet transform, which partitions the variability of a time series as a function of both time and scale, was adapted for use in the analysis of eddy-rich oceanographic velocity measurements. The following results pertain to the properties of the wavelet transform:

- A (scale)$^{-1}$ normalization, as opposed to the usual (scale)$^{-1/2}$ normalization, has a "dilation invariance" property, in that changing the duration of a structure stretches and translates the structure's transform on the time-scale plane without change in amplitude.

- When both wavelet and time series are complex-valued, there are three sets of two complex valued wavelet transforms: u and v components, clockwise / counterclockwise, and locally even / locally odd.

- A "total" wavelet transform $\mathcal{T}$ may be defined equivalently as the root-sum-squared-modulus of the two members of any of the three decompositions mentioned above.

- The total wavelet transform $\mathcal{T}$ has the simple property that the transform of a carrier wave of frequency f_o modulated by a (sufficiently) slowly varying envelope, at the scale at which the wavelet frequency also equals f_o, recovers the envelope of the wave smoothed by the wavelet envelope.

The wavelet transform was seen to be of value in application to eddy-rich time series from the Labrador Sea, in particular:

- A coherent eddy was found to be distinguished by an even-odd-even "tripole"— a maximum in the odd transform flanked by maxima in the even transform.

- The wavelet transform "unwraps" the structure of a complex-valued time series into components that are independent of rotation, allowing current anomaly structure as well as time evolution to be displayed simultaneously.

- A definition of an isolated velocity anomaly can be created by searching for suitable "peaks" of the total wavelet transform "geography" on the time-scale plane.

Additionally, the charactacteristic eddy structures in the wavelet transform appear (Lilly 2002) to be relatively insensitive to unsteadiness in the advecting flow or to advection due to other same-signed eddies.

The wavelet-based detector presented here, while still not fully objective, allows a precise definition of what is not an eddy, permitting a final subjective decision to be based on a relatively small set of events. This definition is fairly general since a broad range of eddy-like forms should give rise to time-frequency localized events. However, it should be pointed out that the interpretation of currents from a single point is difficult, and a positive diagnosis of an advected eddy requires an assessment of its vertical θ/S and current structure. In the following section this definition will become the starting place for a study of coherent eddies in the Labrador Sea mooring data.

4. Coherent eddies observed at Bravo / K1, 1994–1999

As discussed in Section 1, coherent eddies are expected to be of importance in a convecting region such as the Labrador Sea. The Bravo / K1 mooring data presented in the Section 2 indeed appear to contain, and sometimes to be dominated by, eddy-like events. In the previous section, a definition of a potentially eddy-like velocity anomaly based on the continuous wavelet transform was proposed. Here that definition will become the starting point for a multi-year eddy census, using densely-instrumented Bravo and K1 moorings during 1994–1999 (see Table 1). Simple physical measures of the advected eddies can be then defined, and their structures examined in detail. An emphasis will be placed on determining patterns of annual and interannual variability.

4.1. An eddy census

4.1.1. Automated event detection

The definition of an eddy-like velocity anomaly derived in the previous section contains two free parameters, an "amplitude cutoff" χ_a describing the magnitude of the anomaly and a "rise cutoff" χ_b describing the difference between the anomaly magnitude and that of small-scale "noise". Provided that the advection velocity varies slowly relative to the duration of the feature's passage, this definition should detect eddies having a variety of forms (Gaussian, Rankine, etc.). Further, it is independent of the duration of the eddy (and therefore of both the eddy's size and the advection speed) as well as the of direction of the advecting flow.

The velocity anomaly definition was applied to the seven mooring-years of data from the Bravo / K1 moorings during 1994–1999, which includes two overlapping years of data in addition to the five time series shown in Fig. 14. The value of the amplitude cutoff χ_a was set on a year-by-year basis to reflect what appears to be the local "noise level", below which our subjective assesment found no events which appeared to be coherent eddies: $\chi_a = 6$ for 1994–1995, $\chi_a = 7$ for 1995–1998, and $\chi_a = 10$ for 1998–1999, corresponding roughly to peak azimuthal velocities of 12, 14, and 20 cm s^{-1}, respectively. A value of the "rise" cutoff $\chi_b = 2$ was used for all years. Events meeting these criteria in Fig. 14 are indicated by symbols.

4.1.2. Subjective categorization

Following the initial identification of isolated velocity anomalies, these events can be examined in detail and sorted into "apparent eddies" and "apparent non-eddies" by examining the currents and water mass structures. For an event to be judged an eddy, it must have a velocity hodograph that is qualitatively similar to those generated by simple models of isolated or mutually advecting eddies; see LR or Lilly (2002) for details and case studies. Further, it must have a well-defined θ/S core in the vertical / temporal plane (this criterion will be justified *a posteriori*). The requirement of a θ/S core is necessary because hodographs at a single depth can occasionally be misleading; observations at multiple depths are generally necessary in order to confidently label an event as an eddy.

It is important to make a distinction between actual physical eddies, and their form as recorded by the mooring. An eddy will yield a recognizable velocity structure in a mooring time series only if the advecting flow varies relatively slowly over the eddy duration, hence the use of the term "apparent". The non-eddies are temporally localized velocity anomalies whose spatial structure cannot be inferred from their temporal structure, and could represent eddies whose temporal form is highly distorted, or self-advecting dipoles, or other physical features.

The set of wavelet-identified events is expected to include all or nearly all true eddy-advection events. The set of events rejected by the subjective assessment should include nearly all velocity anomalies not associated with eddy advection as well as some that are. Therefore overall analysis is therefore expected to reject some true eddies (especially when currents are highly variable) but to accept very few or zero non-eddies.

4.1.3. Event detection results

Fifty-four features are detected at Bravo and K1 during the period 1994–1999, 33 of which are labelled "apparent eddies" and 21 "apparent non-eddies". The annual cycle of apparent eddies and apparent non-eddies is shown in Fig. 15a. The non-eddies are concentrated during April–May, with 15 of the 21 non-eddies occurring during this period, precisely when the annual cycle of speed has its annual peak. These two months are also unusual because the currents tend to be highly variable, as is evident from the enhanced small-scale activity during these months in Fig. 14). Outside of these two months, only 6 of 35 events are judged to be non-eddies, thus the wavelet-based criterion appears to be a good "first guess". Further, requiring a θ/S core did not result in the rejection of a large number of events, therefore "invisible" eddies having eddy-like form but no θ/S anomaly appear to be rare or nonexistent during May through February. More likely the few rejected events are eddy "near-misses", resulting in velocity anomalies but no θ/S core.

There is also interannual variability in the event magnitude (Fig. 15b), with a dramatic increase over the five-year time period mirroring the increase in annual-mean speed reported in Section 2 (see Fig. 3f). Indeed, it appears that the interannual increase in speed is a consequence of averaging over increasingly energetic isolated events, many of which may be identified as coherent eddies. The magnitude of the coherent eddies currents increases by roughly threefold during this time period.

4.2. Eddy measures

Consider an eddy of core radius R and azimuthal velocity V advected by a constant mean flow of magnitude U and direction Θ. If this eddy is advected past a mooring, the mooring will observe the eddy core along a chord of half-width L. The chord half-width $L < R$ is the "apparent" eddy radius as observed from the mooring. One would like to form estimates of these quantities, denoted $\tilde{V}$, $\tilde{L}$, and $\tilde{U}$, $\tilde{\Theta}$.

It is useful to specify a rotated coordinate system for the mooring velocity observations,

based on the estimated advecting flow direction for a given eddy. Let u and v be the observed northward and eastward velocity components respectively. The velocity component in the same direction as the advecting flow will be called the parallel component u_p, and the component normal to the advecting flow (in the right hand sense) will be called to the normal component v_n. The normal component of the velocity v_n is odd with respect to the eddy's center for a steady advecting flow, while the parallel component u_p is even.

Details of the estimates are given in Appendix C. In order to estimate the error associated with such estimates, Lilly (2002) performed numerical experiments with a simple eddy-advection model. Although details varied somewhat with the model conditions, it was found the $\tilde{V}$ estimator underestimated the eddy magnitude V by about 15–25%, and had a standard deviation of ~20% of V. Although rough, these estimates are clearly sufficient to resolve the magnitude of interannual variability seen in Fig. 15b.

The eddy polarity (cyclonic or anticyclonic) is found from the vertical structure of the speed together with the density structure. While in principle one can find the rotation sense given the advecting flow based on the flow at a single level, reversals in the direction of the apparent mean flow when the eddies are strong relative to the background can lead to occasional ambiguities in the rotation sense as inferred purely from velocity records.

Determination of an eddy's size is difficult as it requires a knowledge of the advection speed. Three methods for estimating the advecting flow are described in Appendix C. When the advecting flow is large relative to the eddies, the magnitude of the advecting flow can be estimated by simply filtering out the eddy signal. Alternatively, an equivalent barotropic assumption can be used to infer the advecting flow by comparing the measured velocity with the measured shear. Finally, when the density structure of the eddies is well-resolved in both time and the vertical, the advection speed can be found by comparing density to shear through the thermal wind equation. However, each of these methods is only appropriate under certain conditions (as discussed in Appendix C), therefore only at the Bravo mooring during 1994–1995 and 1998–1999 can size be estimated.

4.2.1. Two illustrative events

The observed eddies fall into two distinct types, an example of each which is shown in Fig. 16. These are depth-time cross sections from features advected past the mooring, and can be thought of as approximating slices through the eddies at a fixed time. The velocity component shown is approximately perpendicular to the estimated direction of the advecting flow, and so is primarily due to the eddies themselves.

In Fig. 16a,b anticyclonic currents of ~30 cm s^{-1} swirl about two vertically aligned cold, fresh cores. Located at 1 km and 2 km depth, respectively, these are ~0.3°C (upper core) and ~0.2°C (lower core core) colder than ambient water. In Fig. 16(c,d) currents approaching 70 cm s^{-1} swirl anticyclonically around a warm, salty θ/S core whose temperatures exceed 4.5 degrees. This core appears to be vertically homogenized to a depth of about 300 m. A double velocity core structure is evident, with a weaker current maximum extending from one to two kilometers. These lower currents are associated with a cold, fresh θ/S core that appears to be roughly one-half the diameter of the upper core.

Most of the observed eddies are either similar to the first eddy, with cold, fresh mid-depth θ/S cores and middepth intensified anticyclonic currents, or are similar to the second eddy, with "domes" of warm, salty, surface trapped water and surface-intensified anticyclonic currents. The first type of eddies will be called "convective lenses", since they appear (as will be shown later) to contain convected water from the Labrador Sea interior and generally have a lens-like shape. The second type will be shown to originate in the bounding Irminger Current, and will be called

"Irminger rings" by analogy with eddies shed from other boundary currents such as Gulf Stream rings (no implication as to specific formation mechanism is intended here).

4.2.2. Eddy census results

The measures described above are applied to the thirty-three eddy events observed at the Bravo / K1 moorings during 1994–1999. Eddies are then grouped according to their similarity to the "convective lens" type or the "Irminger ring" type. To qualify for either of these types it is required that an event has a significant temperature anomaly that is outside the variance envelope of the de-eddied spring CTD sections (described in Appendix A) from the beginning of the relevant mooring-year. Of the 33 eddy events, 13 appear to be of the "anticyclonic lens" and 12 "Irminger ring" type, with eight eddies of other or ambiguous type. Eddy times, parameters, and categorizations are given in Tables 2 and 3.

The results are summarized in Fig. 17. Panel (a) shows the estimated normal velocity, here with negative values indicating anticyclonic rotation and positive values cyclonic rotation. Panel (b) shows the depth at which the maximum eddy currents occur, together with the instrument locations. Panel (c) shows the temperature of each event, with the upper symbol showing temperature at the instrument depth closest to 250 m, and the lower symbol showing the minimum temperature above ~1250 m; for reference, the mean temperature from the preceding spring's hydrographic section at 250 m and 1000 m are also shown.

A number of interesting patterns are apparent. First, there is an overwhelming dominance of anticyclones, with only two of the thirty-three eddies rotating cyclonically. The two cyclones were both observed during 1994, and consisted of warm θ/S core and cyclonic currents, as reported in Lilly and Rhines (2002) [LR].

Second, a transition in both the velocity and temperature structure of coherent eddies is observed. Estimated azimuthal currents increase from $\tilde{V}$=15–30 cm s^{-1} during 1994–1997 to $\tilde{V}$=30–80 cm s^{-1} during 1998–2000. At the same time the depth of maximum observed eddy currents moves[8] from 700–2500 m to 100–200 m. Most eddies having anomalously cold temperatures between 500 m and 1 km are seen before mid-1997, while very warm near-surface temperatures are common after this time. A few of these warm-core eddies also have cold mid-depth cores. The transition between the "convective lens" eddies and the "Irminger ring" eddies is sharp, with observations overlapping only within a six-month period. In the following two sections the structure of these two types of eddies is described in more detail.

It is clear from examining the speed time series together with the locations of detected eddies (see Fig. 14) that the transition to the occurrence of strong "Irminger ring" type eddies in the Bravo / K1 mooring records is the primary cause of the speed increase observed by these moorings after 1997 (Fig 3f). For instance, during the 1998–1999 mooring year, the Bravo mooring was inside or on the periphery of 40–80 cm s^{-1} Irminger ring type eddies for roughly half the year. This suggests that the lack of a speed increase at the other moorings is attributable to a local persistence of Irminger rings eddies near the Bravo / K1 moorings but not near the others; this hypothesis will be confirmed in Section 6.

The number of independent observations of each type of eddy is smaller than the number of events reported for two reasons. First, during the two years in which they overlap the K1 and Bravo moorings often appear to observe the same features. Second, it is possible that the same eddy or group of eddies pass by the mooring repeatedly; this notion is supported by the form of the velocity structures associated with some of the eddies, as discussed in Lilly (2002). Conceivably only a half-dozen separate eddies of each type are actually observed, passing by the

[8]Note the absence of observations in the central water column during 1995–1996; these eddies are also presumed to be middepth-intensified.

two moorings multiple times.

The results presented herein deal with the structures of the eddies rather than their statistics. It is important to emphasize that the Bravo / K1 mooring is not necessarily representative of the Labrador Sea interior as a whole. It is unlikely that quantities such as the fractional area covered by eddies, or the ratio of cyclones to anticyclones, can be meaningfully determined based only on a point measurement. Nevertheless, with only two of thirty-three events spanning five years rotating cyclonically, the relative sparseness of cyclonic eddies appears to be well-established.

4.3. Convective lenses

During 1994–1999, 13 events[9] similar to the "convective lens" shown in Fig. 16a,b were observed, having middepth-intensified currents (Fig. 18a) and cold, fresh middepth θ/S cores. The speeds of these eddies range from 10 to 30 cm s^{-1}, with most about 15 cm s^{-1}. For three convective lenses, size estimates were possible, and these range from 5–18 km with the two better-observed eddies appearing to be less than 7 km across.

The size of these latter two eddies is somewhat less that the first baroclinic deformation radius (associated with the normal mode shown in Fig. 8) of $\sim$7 km. Although there are too few observations to be able to make a categorical statement about the eddy size, based on their form — with a middepth velocity maximum— they appear similar to a class of eddies known as coherent submesoscale vortices or SCVs (McWilliams 1985), of which eddies of Mediterranean water in the North Atlantic (McDowell & Rossby 1978, Armi & Zenk 1984) are the most well-known example.

4.3.1. Origin

The cold, fresh θ/S properties of the cores of these "convective lenses" are comparable to those observed in the central Labrador Sea during deep convection (Lilly et al. 1999), in agreement with a one-dimensional mixing model (see Appendix B for details incorporating recent *in situ* surface flux measurements). Yet a rapid (1–2 month) rebound to warmer, saltier properties following deep convection is also observed [see Lilly et al. (1999)], so the large-scale θ/S properties appear to match the eddy properties only briefly. By contrast the Labrador Sea water is already colder and fresher along isopycnals than any other water mass in the North Atlantic, and experiments with the one-dimensional mixing model show such cold, fresh, dense water could not be produced by convection into the surrounding water masses. It therefore seems clear that these eddies originate in deep convection in the Labrador Sea interior, hence the name "convective lenses". Eddies of this type were reported in LR based on observations from the Bravo mooring during June–November 1994. A more detailed discussion of the water mass properties of several of the convective lenses can be found therein.

4.3.2. Double cores

It is reasonable to expect the depth of strongest eddy currents to decrease as the depth of convection decreases, but this turns out to not be the case. During 1994–1995, the convective lenses had their strongest currents between 750 and 1250 m, while convection reached 2 km; by contrast, weak current maxima were consistently observed between 1800 and 2500 m during 1996–1997, although the depth of convection is estimated at 1200 m. This seemingly minor detail actually reflects an interesting feature of the "convective lens" type eddies: multiple vertically-aligned cores.

The structure of eddy shown in Fig. 16a,b is particularly interesting; two other eddies from

[9]This includes three eddies from 1995–1996 whose cores were not observed due to instrument failure in the central water column. However, owing to the similarity of these features with other anticyclones observed in both the previous and follow years, it seems reasonable to group them with the "convective lens" type eddies.

1996–1997 are virtually identical. The lower core contains water isopycnally colder and fresher than all ambient water observed by the mooring or by the spring 1996 hydrographic section, but matching properties from the spring 1995 section. It appears impossible for convection during the winter of 1995–1996 to have locally penetrated to 2 km: NCEP heat fluxes during the winter of 1995–1996 were the smallest of the 1990's (see Fig. 3d), and no sign of convective modification deeper than 1250 m is seen in the spring 1996 CTD data. Thus it seems these eddies consist of a shallow (500–1000 m) lens of newly convected water, on top of a deeper (1.5–2.5 km) lens of convected water formed more than one year earlier.

Such composite vertical structure of the θ/S cores appears to be the rule rather than the exception. This structure was noted earlier in LR on the basis of the 1994 data. Of the eight "convective lens" type eddies observed by three or more instruments over the depth interval 500–2500 m, all had two (or once, three) vertically-aligned θ/S cores. Although the reason is unclear, this appears to be an unusual feature of the Labrador Sea convective lenses with respect to other coherent submesoscale eddies; see Section 7 for a discussion.

4.3.3. Comparison with a numerical model

It is useful to compare the convective lenses with the eddies generated by a numerical model of the aftermath of deep convection. Chimney-adjustment and localized-forcing models have become the underpinning for theoretical understanding of deep convection (Jones & Marshall 1993, 1997, Send & Marshall 1995), yet direct comparisons with observations have been rare.

Here simulations using the sigma-coordinate SPEM model version 5.1 (Haidvogel, Wilkin & Young 1991) are used with a square, closed domain of ~200 km, ~2 km horizontal resolution, and 31 vertical layers. The model runs are similar to those described in Send and Käse (1998), and are set up to be similar to the Labrador Sea during the late stages of deep convection. A large cylinder of dense homogeneous fluid of 1.5 km depth and 40 km radius was embedded within a weak stratification, all of which was lying over a strong deep stratification to 2.5 km. The cylinder adjusts and forms a rim current which becomes baroclinically unstable and sheds pairs of oppositely-signed eddies, as in Jones and Marshall (1993) and elsewhere.

A sample cross-section through the model showing a typical eddy pair is given in Fig. 19; note that the x-axis here is distance rather than time, since the model data was not available at sufficient temporal resolution to allow depth-time sections to be presented. The anticyclone is remarkably similar in temperature anomaly, strength, and vertical structure to the "convective lens" type eddies. By contrast, anticyclones in numerical models not including a dense lower layer tend to be bottom-intensified. The deep stratification therefore appears to be necessary for the creation of middepth-intensified anticyclones. The cyclones in this model, such as the one shown in Fig. 19, are somewhat stronger than the anticyclones and are surface-intensified with isopycnals bowing upwards at all depths.

In this survey thirteen convectively-generated anticyclones were observed in the Labrador Sea and zero convectively-generated cyclones. While sampling issues are certainly relevant, this thirteen-to-zero ratio is compelling evidence that convectively-generated cyclones are sparse or nonexistent in the neighborhood of the Bravo mooring during June through February. (Because it is difficult to identify eddies during convection from the mooring, no statement can be made about the initial ratio of cyclones and anticyclones.) This important difference between the model and the observations could have a number of physical interpretations, as discussed in more detail in Section 7.

4.4. Irminger rings

Twelve events appear to be of the "Irminger ring" type, similar to the eddy shown in Fig. 16(c,d). All of these have surface-intensified currents (Fig. 18b) ranging from 30–80 cm s^{-1}

in magnitude. From five well-resolved observations of Irminger rings during 1998–1999, the size can be estimated to be in the range 15–30 km, significantly larger than the deformation radius. The double-core structure apparent in Fig. 16(c,d) is not unusual, but occurs in at least half (and possibly all) of the eddies of this type.

Profiles of temperature versus depth for the Irminger rings observed during 1998–1999 are shown in Fig. 20, together with an anomalous hydrographic profile from the Labrador Sea interior along the AR7W section during the summer of 1998. This cast shows two warm mixed layers stacked on top of each other, each of about 400–500 m thickness, resulting in isopycnal displacements over 1 km at 1.4 km depth relative to the ambient Labrador Sea. Comparison with the mooring temperature profiles suggests this anomalous cast passes through the core of an Irminger ring. In particular, the vertical structure of the mooring temperatures confirms in some cases the existence of a warm surface mixed layer, and also shows secondary cores at depth (either warm or cold). It may be that this identical eddy was later observed at the mooring.

4.4.1. Origin

The warm temperatures and shallow (~400–500 m) mixed layers observed in the Irminger ring eddies could not have been produced by local convection near the Bravo site, but are similar to those observed on the northern rim of the Labrador Sea during winter (Pickart et al. 2002). The origin of the July 1998 eddy can be constrained further by a more detailed comparison with the three-dimensional hydrographic survey performed by the R/V Knorr in February–March 1997. Since the detailed wintertime survey was performed the year before the summertime eddy was observed, we must assume that the convected water column after the winter of 1998 was similar to that observed in the preceding year.

The July 1998 eddy shown in Fig. 20 has two well-defined homogeneous cores each having a thickness of 400–500 m, and potential temperatures of 3.5 and 4.3 °C for the lower and upper cores respectively. Thus one has three tracers that describe the eddy's origin: temperature, density (or salinity), and thickness.

Locations of hydrographic stations for the February–March 1997 cruise are shown in Fig. 21, with the different symbols indicating each of seven different hydrographic lines. To compare with the July 1998 eddy, the mixed layer model of Appendix B is applied to each station. A fixed amount of heat is removed from the surface of the water column, to mimic the effects of the continued heat loss experienced by the ocean in between the time station was taken and the end of winter. For simplicity, differences in station times are neglected and 0.5 GJ m^{-2} (1 GJ = 10^9 J) is removed from each station, corresponding to about 200 W m^{-2} of heat loss for about one month; the results are not particularly sensitive to this choice.

The properties of the resulting mixed layers are shown in Fig. 22. The values of θ characterizing the cores of the July 1998 eddy are shown with vertical lines. In the far north, one sees very cold mixed layers which are also very shallow, due to the buoyancy of the fresh surface coastal current. South of 59° N, mixed layer termperatures are between 2.5 and 3.25°C. The bulk of these stations have relatively deep (>500 m) mixed layers. The only stations having mixed layer temperatures matching the July 1998 eddy are found along the "triangle" line (the northernmost line in Fig. 21) in between 59 and 62° N. The mixed layer depth range for this group of stations is 250–500 m, with several stations having ~400–500 m mixed layer depths in agreement with the July 1998 eddy. Mixed layer salinity (not shown) also matches.

Thus it appears that the eddies of this type originate on the Greenland side of the northern Labrador Sea. Their water mass cores are composed of convected water from or strongly modified by the warm, salty Irminger Current, motivating the name "Irminger rings". This water mass result is interesting because satellite and float observations (Cuny et al. 2002, Prater 2002,

Lavender et al. 2000) show an EKE maximum near separation point of the 2000 and 3000 m isobaths (52°W, 61°N), apparently due to an instability of the West Greenland / Irminger Current system. In Section 6, detailed examination of TOPEX altimetry will confirm the EKE maximum as the generation site for the Irminger ring eddies.

4.4.2. Double cores

At least half of the Irminger rings have secondary θ/S cores at depth (~1–1.5 km) associated with an enhanced downward isopycnal depression. Although the instrument spacing was insufficient to resolve the density structure of lower core, the isopycnal depressions suggests thick layers of uniform density as with the anomalous hydrographic profile. This interpretation is supported by temperature time series which are often completely flat above 500 m and again from 1–1.5 km, indicating homogeneous layers. Examples of deep cores both warmer/saltier and colder/fresher than ambient water are observed. Additional discussion of this double-core structure may be found in Section 7.

4.4.3. A ship-surveyed eddy

An eddy observed in January of 1998 by the R/V Knorr appears to be an Irminger ring. Figure 23a shows contours of the ship-intake sea surface temperature (SST) together with the locations of the ship-track (dotted lines). Temperatures in a roughly circular region of about 50 km diameter were 3.5–4°C compared with ~3°C in the ambient Labrador Sea. The center of this feature as estimated from the SSTs is marked with a triangle.

The vertical structure of the eddy was resolved with expendable bathythermograph casts (XBTs), shown as circles in Fig. 23a. For each XBT cast, a mixed layer was computed by finding the first point beneath 133 m depth differing by more than 0.1°C from the mean value of that cast from 100–133 m. The rationale for beginning at 100 m is that intrusions seen in the top 100 m of some casts appear to obscure the true mixed layer depths and are likely to represent density-compensated interleaving. The mixed layer potential temperature for each cast, averaging between the surface and the estimated mixed layer depth, were then computed.

The mixed layer depth and temperature are shown in Figs. 23b,c versus the distance from the estimated center of the eddy (the triangle in Fig. 23a). The mixed layer extends to as deep as 500 m in the interior of the eddy but only to ~250 m in the surrounding water; several shallow mixed layers are likely to be a result of the intrusions described above. Mixed layer temperature drop from ~3.5°C in the eddy interior to ~3.1°C. In both mixed layer depth and temperature, the radius of the eddy appears to be 15–20 km.

From a single profile of temperature and salinity through the eddy core (not shown) the baroclinic currents can be estimated. Using 20 km for the eddy radius the surface currents are seen to rotate anticyclonically at 25 cm s^{-1} relative to 2500 m, similar to the Irminger rings observed by the mooring. Further, differences in mixed layer depths and properties between the eddy core and exterior are similar to those predicted from the 1-D mixing model applied to the Irminger ring observed the previous year in the summertime 1998 hydrographic section (see Fig. 20).

4.4.4. Effects on convection

It therefore seems clear the eddy presented in Fig. 23 is of the same type as the "Irminger rings" observed by the mooring. However, it is interesting that the deepest mixed layers in January— early in the winter as far as convection is concerned— should occur inside a buoyant eddy. This situation is doubly surprising since the buoyant eddy is an anticyclone. In convection literature, one finds frequent discussion of "preconditioning" of the water column by cyclonic circulation, which coincides with uplifted isopyncals and therefore a greater susceptability to

convection. The deepest mixed layers in the eddy-field convection experiments of Legg and McWilliams (2001) thus occur inside cyclonic eddies.

To address the influence of such an eddy on convection, we examine the erosion of the eddy's core expected as a surface heat loss is applied. A quantity called "available heat storage" $\mathbf{H}(z)$, defined in Appendix B and illustrated in Fig. 10, is the amount of heat loss to the atmosphere per unit horizontal area necessary to convect to depth $-z$. The available heat storage can be computed from profiles of potential temperature and salinity with depth, given an estimation of the ratio between the latent heat loss and the total heat loss.

The available heat storage $\mathbf{H}(z)$ is shown in Fig. 20d for the anomalous hydrographic cast observed in July 1998, and for the ambient water column. The anomalous profile is initially more susceptible to convection: after a heat loss of only 0.5 GJ m^{-2} (two months of 100W m^{-2} heat loss), the depth of the mixed layer is predicted to be ~500 m for the anomalous profile and ~100 m for the ambient Labrador Sea. Such an eddy, which apparently survives one winter's convection because its buoyancy limits the surface mixed layer to shallow depths, is expected to be the site of the deepest mixed layers should it persist in the Labrador Sea interior until the following winter. Thus the "preconditioning" which leads to the deepest mixed layers is not the usual uplift mechanism, rather it is the previous year's heat loss. (Note that while surface fluxes would be expected to warm (or cool) the eddy and its surroundings equally, the eddy is apparently insulated from the subsurface restratification the rest of the Labrador Sea undergoes.)

Long-lived anticyclones could therefore result in locations of particularly deep convection in early winter. Indeed the eddy shown in Fig. 23 appears to be such an Irminger ring that was convected once, survived a summer in the Labrador Sea, and is now being convected a second time. The importance of this modification of the "geography" of deep convection is discussed in Section 7.

4.4.5. Heat content

An important question is whether the Irminger rings transport a significant amount of heat into the Labrador Sea interior. Since the Labrador Sea interior loses heat to the atmosphere in the annual average, lateral fluxes of heat must compensate. Although meaningful estimates of the eddy spatial distribution cannot be made on the basis of a single point measurement, the contribution of an individual Irminger ring to the lateral heat exchange can be estimated from the anomalous hydrographic profile shown in Fig. 20. The heat content $H(z)$ of a water column per unit horizontal area is defined as

$$H(z) = \rho_o c_p \int_{-z}^{0} \theta(z')dz'$$

where ρ_o is a reference density of seawater and c_p is the specific heat of water at constant pressure. Note that z is positive upwards.

The net increase in the heat content of this region due to an incoming eddy is the difference between the heat content of the eddy and the heat content of the water it displaces. Assume that in the winter the ambient water column was homogenized down to a certain depth. In Section 2 we estimated the depth of convection to be about one kilometer a few months before the observations in Fig. 20 were taken. The variance envelope for the ambient water column in this figure collapses onto a temperature of about 3.1° C beneath about 600 m, suggesting that this temperature represents the homogenized water column at the end of convection and the warm water above it is due to recent lateral restratification. From the temperature profile inside the warm eddy, which has been kept isolated from the ambient restratification, one sees that

the effect of solar insulation is trapped in a very thin layer near the surface. Thus, the mean ambient water column set to 3.1° C above one kilometer is a reasonable approximation to the temperature profile one would have expected in the absence of restratification. The difference in heat content between this adjusted ambient mean and the warm eddy profile is an estimate of the heat imported into the Labrador Sea during the eddy formation process. Integrating in this way to 2000 m, one obtains a value of 4.6 GJ.

An equivalent heat increase for the entire Labrador Sea interior can be found by multiplying the heat content difference by the ratio of the eddy's horizontal area to the area of the Labrador Sea interior, denoted b. Assuming a 20 km eddy radius and approximating the Labrador Sea interior as a cicle of radius 325 km, $b \sim 0.004$. The 4.6 GJ m^{-2} heat content difference between the eddy and adjusted ambient mean is equivalent to 18 MJ m^{-2} (1 MJ = 10^6 J) when distributed over the entire Labrador Sea. In Section 2 the mean lateral heat flux in interior Labrador Sea during the 1990's was found to be 48 W m^{-2}, or 1.6 GJ m^{-2} year^{-1}. Using the above numbers, one eddy every ten days (for example) would contribute 0.67 GJ m^{-2} year^{-1} or 20 W m^{-2} to the warming of the Labrador Sea which would account for about 40% of the estimated total lateral heat flux. Obviously, the importance of the Irminger eddies to the heat budget depends upon the frequency of their occurence, which is not yet known.

4.5. Summary

This section presented a detailed survey of coherent eddies in the central Labrador Sea using measurements from the densely-instrumented Bravo and K1 moorings during 1994–1999. The process used to identify such features combined the geometrical analysis of Lilly and Rhines (2002) [LR] with the automated algorithm developed in Section 3. For the thirty-three coherent eddies found in the data, simple measures of azimuthal velocity were formed; in ten instances it was also possible to estimate the eddy size. Both velocity and size estimates are expected to underestimate the true values somewhat, by perhaps 20%. The principal results are:

- An overwhelming dominance of anticyclonic eddies was found, with only two of thirty-three eddies rotating in a cyclonic sense.
- The anticyclonic eddies are of two different types, "convective lens" type eddies with middepth-intensified currents of ~15–30 cm s^{-1} and radii of 5-15 km, and "Irminger ring" eddies with surface-intensified ~30–80 cm s^{-1} currents and 15–30 km radii.
- The θ/S properties of the former locate them as originating in the interior Labrador Sea during winter [see LR], and they compare favorably with anticyclonic eddies observed in a numerical model of a baroclinically unstable "column" of dense water.
- The Irminger ring type eddies appear from their θ/S properties to originate in the Irminger Current, and are notable for their deep mixed layers, the result of accumulated heat loss from the previous winter.
- Both types of eddies tend to have vertically-aligned composite cores.
- A transition occurs between the two types of eddies around mid-1997, with no Irminger ring eddies observed before this time and only two convective lenses observed after this time.
- The transition to persistent Irminger ring eddies at the Bravo / K1 location is the primary cause of the increased current speed observed by those moorings, reported in Section 2.2.

However, the spatial representativeness of the Bravo and K1 moorings (located only 20 km apart) is clearly an issue, particularly since other moorings in the interior Labrador Sea did not record a speed increase after 1997. It is striking and counterintuitive that the transition from weak to strong eddies should coincide with the transition between relatively deep (~2 km) and relatively shallow (~1 km) convection. In contrast to the isolated convection region hypothesis discussed in Section 1.2, such a transition appears to implicate the boundary current in shaping the energetics of the Labrador Sea interior during the later time period. Thus, it is essential to know whether the observed transition represents some shift in the entire Labrador Sea gyre, or a purely local phenomenon. The desire to resolve spatial variations in the eddy field serves as a motivation for the remainder of this study, in which a eddy census is conducted using TOPEX altimetry. Extended discussions of the implications of this section's results will be postponed until Section 7.

5. An automated event census for satellite altimetry

This section deals with the technical aspects of creating a census of eddy-like events using satellite altimetry, with a more detailed discussion of the physical motivations together with the results of the census postponed until Section 6. This has been done in order to allow a better continuity of reasoning in the next section, and because a detailed understanding of the technical elements is not essential for the physical discussion.

The basic difficulty with studying coherent eddies with an altimeter is that one hopes make statements about subsurface dynamical structures based on entirely on noisy one-dimensional measurements of sea surface height. The most basic approach is to search through the altimeter data "by hand" for extreme events. The goal of this section is to develop a reasonable definition for a coherent eddy in altimeter data based exclusively on an automated examination of the form of sea surface height anomalies. Such a form-based definition is not limited to features large enough and slowly moving enough to be well resolved by the altimeter grid, and can be compared with a noise model to ensure that detected events are unlikely to be the result of instrument noise.

However, it should be emphasized that it should not be expected that there exists a one-to-one correspondence between physical eddies in the ocean and any class of signal anomalies, no matter how well chosen. Instead we hope to identify a class of signal anomalies that is expected to include coherent eddies as a subset, and which can serve as a reasonable proxy field for examining the distributions and variability of the underlying eddies. This section will isolate such an "eddy band" and develop statistical methods for forming inferences about the physical eddy field. Additional specific issues regarding interpretations of signal anomalies are discussed in the introduction to Section 6.

5.1. Data and definitions

The primary dataset used in this and the following section is alongtrack sea surface height data from the TOPEX / Poseidon altimeter (Fu, Christensen, Yamarone, Lefebvre, Ménard, Dorrer & Escudier 1994). In-depth discussions of this instrument can be found elsewhere (Fu 2001, Martin 2003), but a brief summary is relevant here. The TOPEX / Poseidon satellite crisscrosses the earth between ± 66° latitude with a pattern of 127 tracks, with ascending tracks sloping to the northeast and descending tracks to the southeast. Each track is repeated almost exactly (± 1 km) every 9.92 days, a period referred to as one "cycle". The perpendicular distance between tracks in the Labrador Sea region (see Fig. 24) is approximately 100 km, but decreases northward as the satellite approaches its turning latitude. The alongtrack instrument data is averaged into one-second bins, corresponding to about 5.7 km at the latitude of the Labrador

Sea. The footprint of the altimeter is a circle of radius 2.5 km (without swell), so that although the crosstrack separation is large relative to the local deformation radius (about 7 km), one could hope to locate small-scale structures in the alongtrack data.

5.1.1. Processing

Processing of the raw TOPEX / Poseidon signal into a meaningful sea surface height signal depends upon a large number of intricate corrections. The resulting sea surface height (SSH) residual $\eta' \equiv \eta - \eta_o$ represents the level of the sea surface relative to a time-independent mean η_o, which includes the geoid — a stationary but unknown level surface — plus a contribution from the time mean portion of the currents. The data used here is the NASA / Goddard Space Flight Center reprocessed collinear product (Koblinsky, Ray, Beckley, Wang, Tsaoussi, Brenner & Williamson 1999*b*, Koblinsky, Ray, Beckley, Tsaoussi & Wang 1999*a*) developed as part of the NASA / NOAA Pathfinder project, which in addition to the usual corrections also removes aliasing of η_o due to small crosstrack excursions. After corrections the standard deviation of the measurement error is estimated to be about 4.7 cm (Fu et al. 1994).

Additional processing is necessary to prepare the data for the present analysis. Close examination of the structure of the sea surface height noise (not shown) suggests that the tails of the SSH probability density function are associated with periods of increased unbiased variance which can be removed by smoothing, rather than with isolated spikes. The data is nevertheless despiked by taking the second central difference and removing points corresponding to large excursions. Gaps in the alongtrack data as long as ten points are linearly interpolated over. Some filtering is then necessary to reduce instrument noise; all sea surface height data used here have been filtered with a five point Hanning filter, corresponding to 28.5 km on account of the 5.7 km data point spacing.

5.1.2. Definitions

Let (x_a, y_c) be a local (right-handed) coordinate system with x_a being the alongtrack direction, y_c the crosstrack direction, and (u_a, v_c) the corresponding along- and crosstrack currents. The time-variable crosstrack currents v_c' are estimated from the sea surface height residual η' as

$$v_c' \equiv \frac{g}{f}\frac{d\eta'}{dx_a} \tag{5.17}$$

assuming geostrophic balance, with f being the (constant) Coriolis frequency and g the acceleration due to gravity, and where the prime indicates a deviation from a time or ensemble mean value. The eddy kinetic energy (EKE) is then given by

$$\mathrm{EKE} \equiv \frac{1}{2}\overline{(u'^2 + v'^2)} = \overline{v_c'^2} \tag{5.18}$$

assuming that the time-varying currents are isotropic ($\overline{u_a'^2} = \overline{v_c'^2}$); here the overbar indicates an average over realizations or "cycles". EKE can also be expressed in terms of a root-mean-square "EKE speed" which we denote V_{EKE}

$$V_{\mathrm{EKE}} \equiv (2\,\mathrm{EKE})^{1/2} = (\overline{u'^2 + v'^2})^{1/2} = (2\,\overline{v_c'^2}\,)^{1/2}.$$

V_{EKE} is also the standard deviation of $u + iv$, defining $\mathrm{var}\{z\} = \overline{zz^*}$ for zero-mean complex-valued z as usual, and differs from the average speed $V_S \equiv \overline{(u'^2 + v'^2)^{1/2}}$ by a reversal in the orders of averaging and of taking the square root.

As before, the term "Labrador Sea interior" will be defined to mean the thick dashed curve in Fig. 24, which is the 3000 m isobath cut off at the southeast edge. This is approximately a circle of radius 300 km. A local Cartesian coordinate system will be used having a point (58.5° N, 52° W) near the center of the Labrador Sea interior as its origin.

5.2. An initial look at eddy kinetic energy values

The basic pattern of time-mean eddy kinetic energy shown in Fig. 24 has been reported by other authors (White & Heywood 1995, Stammer & Wunsch 1999). The maximum value of V_{EKE} (32 cm s^{-1}), equivalent to $\sim$500 cm^2 s^{-2}, is comparable to maximum values of $\sim$500 cm^2 s^{-2} and $\sim$400 cm^2 s^{-2} reported by earlier studies using altimeter (White & Heywood 1995) and drifter (Cuny et al. 2002) data, respectively. Additionally, a comparison of the monthly altimeter V_{EKE} in the vicinity of the Bravo / K1 moorings with similar quantities formed from the mooring data was presented in Lilly (2002). The mean annual cycles of monthly means observed by these two platforms were found to agree to within 10–20% except during the chaotic winter months (December–March), and the general patterns of seasonal variability were found to be comparable in both datasets. This suggests the altimeter signal includes contributions from the structures which account for the observed current variability described in Section 2.2. This idea is further supported by a comparision of the mooring with a nearby altimeter track presented in the next section, which shows that large-magnitude Irminger ring type eddies are often observed contemporaneously by the two observational platforms.

We now investigate the expected contribution of instrument noise to the V_{EKE} values. The standard deviation of the altimeter's estimate of sea surface height is about 4.7 cm (Fu et al. 1994). However, as pointed out by Kelly, Beardsley, Limeburner, Brink, Paduan & Chereskin (1998), the largest part of this error (3.5 cm) is due to the orbital model and involves spatial scales much larger than the size of an individual eddy. The remaining 3.1 cm ($\sqrt{4.7^2 - 3.5^2}$) standard deviation represents an estimate of the contribution of instrument noise to sea surface height fluctuations on scales comparable to or smaller than the deformation radius. The V_{EKE} associated with 3.1 cm standard deviation Gaussian white noise, after applying the same five-point Hanning filter using in processing the actual data, is 16.0 cm s^{-1}. The minimum value of the time-mean V_{EKE} (Fig. 24) is about 14 cm s^{-1}, suggesting that this 3.1 cm noise level is, if anything, too high.

Typical numbers for the radius R and peak velocity V for the two types of eddies are $R =$ 10 km, $V = 15$ cm s^{-1} for the convective lenses and $R = 20$ km, $V = 50$ cm s^{-1} for the Irminger rings. Applying these to an estimate of the sea surface displacement [derived below; see (5.25)]

$$\Delta\eta = \frac{5}{3}\frac{f}{g}RV, \tag{5.19}$$

leads to values of 3 cm and 20 cm, respectively. Thus one expects individual eddies of the Irminger ring type to be distinguishable from the background instrument noise, but not those of the convective lens type.

5.3. A wavelet-based event census

5.3.1. Sample eddy solutions

The sea surface height and geostrophic current current profiles associated with two simple eddy solutions are shown in Fig. 25. The even sea surface height signal is a for monopolar eddy "sliced" by an altimeter track along a line passing through its center, while the odd signal is for a dipolar eddy sliced by a line which passes though the center of each of its two opposing vorticity cores. The monopolar eddy is a quasigeostrophic 1.5 layer f-plane solution with a uniform, circular potential vorticity anomaly in the upper layer, and may be described in terms of growing and decaying modified Bessel functions. The dipolar eddy is a stable, self-propagating quasigeostrophic 1.5 layer β-plane solution due to Flierl, Larichev, McWilliams & Reznik (1980), consisting of a horizontally separated pair of opposite-signed vorticity cores in the upper layer. Analytic expressions for both solutions may be found in Lilly (2002).

The solution to the monopolar eddy is entirely determined by the ratio of the eddy radius R to the deformation radius λ. The solution shown in Fig. 25a is for the case $R = \frac{1}{2}\lambda$, and will be called the $\frac{1}{2}\lambda$ eddy. Relevant parameters for the dipole solution, together with their chosen values, are: the Coriolis frequency $f = 1.2 \times 10^{-4}$ s^{-1}, the northward gradient of the Coriolis frequency β (1.2×10^{-11} m^{-1} s^{-1}), the deformation radius λ (7.5 km), the "radius of discontinuity" R_d (40 km), and the east-west phase speed c_p (1.74 cm s^{-1}). The form of the sea surface height profile for the dipolar eddy is not particularly sensitive to the choice of c_p (not shown).

These forms are taken to be illustrative of the types of signals expected to be associated with monopolar and dipolar eddies, respectively, and are not intended to capture the precise dynamics. They will, however, be found to be quite similar to features observed in the altimeter data. In the following, these forms will be allowed to be arbitarily rescaled, and will be used as a reference point in the creation of the automated census.

At this point it is helpful to introduce some terminology. Consider an azimuthally symmetric, geostrophic eddy having a sea surface height displacement δ_o and a radius R_o. δ_o is positive for a cyclone and negative for anticyclones, and we define the radius R_o to be the distance from the eddy's center to its azimuthal velocity maximum. The sea surface displacement along a particular "slice" through this eddy varies with slice location and its magnitude will be less than or equal to $|\delta_o|$; this will be termed the "apparent" sea surface height anomaly. Similarly, one may define an "apparent" radius as one-half the distance between extrema in the alongtrack slope. For a slice through the eddy's center, this recovers the location of the azimuthal velocity maximum. However, for an arbitrary slice, the apparent radius need not be equal to the true radius, as will be shown later. For a dipolar eddy, we define the sea surface height anomaly δ_o to be the maximum minus the minimum sea surface height values associated with the eddy; δ_o is a signed quantity for a monopole but a positive quantity for a dipole. Also, we define an equivalent core radius R_o to be one-half the distance from the zero-crossing of the sea surface height anomaly to either extremum. Thus in Fig. 25 both the monopolar eddy and the dipolar eddy have R_o=10 km and δ_o=10 cm. These definitions of R_o and δ_o will allow for a consistent interpretation of the analysis between monopolar and dipolar forms.

5.3.2. Wavelet transform details

As in Section 3, we will use the continuous wavelet transform (3.1) as a tool for identifying localized features in a signal. Again we use the "n=1" normalization discussed in Section 3.2.2; in essence this normalization chooses the magnitude of a sea surface height anomaly (as opposed to, say, its slope) as the relevant measure of anomaly strength.

Since the features of interest are merely bumps or depressions of the sea surface, and since the data series are short relative to the scales of these features, a very spatially-localized but spectrally broad wavelet is appropriate. We choose a wavelet of the form

$$g_{\tau,a}(x) \equiv \frac{1}{a} h\left(\frac{x-\tau}{a}\right) e^{2\pi i \tilde{k}(x-\tau)} + \frac{\epsilon}{a} \tag{5.20}$$

where $h(x)$ is a slowly-varying envelope, $\tilde{k} \equiv \frac{1}{2} m a^{-1}$ is the wavenumber of the wavelet at scale a, m is a "wiggliness parameter" specifying the number of wavelengths of the sinusoid which fit inside $x = [-a, a]$, and ϵ is a (small) real number necessary to enforce the zero-mean condition. The envelope $h(x)$ is chosen as in Section 3.2.3, while m is set to a value of one-half. This extremely narrow wavelet requires a large correction parameter ϵ, equal to about 2/5 the peak value of $h(x)$.

Finally, the wavelet transform is "calibrated" using the $\frac{1}{2}\lambda$ eddy form shown in Fig. 25a.

The scale parameter a is rescaled ($a' = c_1 a$) so that the wavelet transform modulus of this signal has a maximum value when the scale parameter equals the eddy radius, and the wavelet amplitude is rescaled so that the value of this maximum equals the value of the eddy sea surface displacement, i.e. $|\mathcal{W}| = 10$ cm at a=10 km. It follows from the dilation invariance (3.4) of the wavelet transform that for any $\frac{1}{2}\lambda$ eddy of radius R_o and displacement δ_o sliced through its center, the wavelet transform modulus will obtain a maximum value of $|\mathcal{W}| = |\delta_o|$ at $a = R_o$. Applying this calibrated transform to the sample dipolar form in Fig. 25a, one finds again (almost exactly) a maximum value of $|\mathcal{W}| = \delta_o$ at $a = R_o$. Thus this calibrated transform returns the correct values for both the sample monopolar and sample dipolar forms. For different choices of eddy forms the ratio of transform magnitude to eddy sea surface displacement magnitude, and of wavelet scale to eddy radius, will of course depart from unity, but for reasonable choices of eddy forms the differences are not great.

5.3.3. Isolated signal anomalies

In this subsection we define a class of signal anomalies, and construct a few simple measures of these anomalies which will be dynamically meaningful for anomalies due to actual eddies. A point (τ_*, a_*) will be said to mark an "isolated anomaly" of a signal if it represents the largest value of the wavelet transform modulus within some neighborhood on the space-scale plane

$$|\mathcal{W}(\tau_*, a_*)| \geq |\mathcal{W}(\tau, a)| \left\{ \begin{array}{lcl} |\tau_* - \tau| & \leq & b_\tau \, a_* \\ |a_* - a| & \leq & b_a \, a_* \end{array} \right. \tag{5.21}$$

where b_τ and b_a specify the dimensions of a (τ, a) "box" and are here chosen to be $b_\tau = 1$ and $b_a = 1/2$; note that this definition implies the center of one anomaly may be located inside the diameter of another event provided they are sufficiently separated in scale. The evenness or oddness of an isolated anomaly at (τ_*, a_*) is measured by the phase angle of the (complex-valued) wavelet transform

$$\phi_* \equiv \arg\{\mathcal{W}(\tau_*, a_*)\} = \arctan\left(\frac{\mathcal{W}_s(\tau_*, a_*)}{\mathcal{W}_c(\tau_*, a_*)}\right)$$

which is zero for an even, positive sea surface height excursion, $\pm\pi$ for an even, negative sea surface height excursion, and $\pm\pi/2$ for an odd sea surface height excursion.

A measure of the sea surface height displacement associated with an isolated anomaly is

$$\delta_* \equiv s_* \, |\mathcal{W}(\tau_*, a_*)| \tag{5.22}$$

where $s_* = \pm 1$ is defined as the sign of the even wavelet transform

$$s_* \quad = \quad \left\{ \begin{array}{ll} -1 & \mathcal{W}_c(\tau_*, a_*) < 0 \\ 1 & \mathcal{W}_c(\tau_*, a_*) \geq 0 \end{array} \right.$$

so that δ_* is positive for upwards sea surface height excursions and negative for downward excursions. A measure of the "apparent radius" of an eddy-like signal as defined in Section 5.3.1 is

$$R_* \equiv a_* \left(\sin^2(\phi_*) + 1\right) \tag{5.23}$$

where for a dipolar signal R_* is interpreted as the radius of each core considered separately. Both R_* and δ_* return the correct values for the sample monopolar and dipolar signals.

An estimate of the peak currents in terms of the maximum sea surface height anomaly may be derived as follows. From the velocity profile within a solid-body core (3.14) together with geostrophy one obtains

$$\eta(r) - \eta(0) = \frac{1}{2}\frac{V}{R}\frac{f}{g}r^2 \tag{5.24}$$

where V is the azimuthal velocity at the core radius R. At $r = R$, the edge of the solid-body core, one has

$$V = \frac{2g}{f}\frac{\eta(R) - \eta(0)}{R}$$

which suggests the estimate

$$V_* \equiv -c\frac{2g}{f}\frac{\delta_*}{R_*}, \tag{5.25}$$

where the constant $c \equiv \frac{|\eta(0)-\eta(R)|}{|\eta(0)-\eta(\infty)|}$ will vary with the choice of eddy form; for the sample monopole $c = 0.3$ with $g = 9.81$ m s^{-2} and $f = 1.2 \times 10^{-4}$ s^{-1}. This estimate V_* has been constructed to give the correct answer for the sample monopolar form. For the sample dipole sliced along its axis of symmetry, $|V_*|$ also gives the correct maximum velocity to within a few percent, although in this case the sign of V_* is no longer meaningful.

The dynamical strength of an eddy can be characterized by the peak magnitude of the vertical vorticity $\zeta \equiv \mathbf{k} \cdot \nabla \times \mathbf{u}$ within the eddy core[10]. Using the velocity scale V_*, a nondimensional measure of the relative vertical vorticity an isolated anomaly in the alongtrack sea surface height data is

$$Z_* \equiv \left(\cos^2(\phi_*) + 1\right)\frac{V_*}{fR_*} = -\left(\cos^2(\phi_*) + 1\right)\frac{2cg}{f^2}\frac{\delta_*}{R_*^2}$$

which can also be considered an estimate of the Rossby number. Here the factor of $\cos^2(\phi_*) + 1$ is included because the vorticity at the center of an azimuthally symmetric monopole ($\phi = \pi \pm \pi$) includes equal contributions from orthogonal directions, $\zeta = \frac{dv}{dx} - \frac{du}{dy} = 2\frac{dv}{dx}$, while for a dipole ($\phi = \pm\pi/2$) there is a contribution only along the axis of symmetry and not along the orthogonal direction. Again $|Z_*|$ returns the correct values for the both the sample monopole and sample dipole sliced along their symmetry lines.

5.3.4. Phase sorting

Anomalies will be placed into one of three categories based on their phase angles: positive even ($|\phi_*| < \frac{\pi}{3}$), negative even ($|\phi_*| > \frac{2\pi}{3}$), and odd ($\frac{2\pi}{3} > |\phi_*| > \frac{\pi}{3}$), where ϕ_* varies between π and $-\pi$. These will be referred to as "anticyclonic events", "cyclonic events", and "dipolar events" respectively. The use of the term "event" emphasizes that this classification applies to the signal forms and is not intended to imply a one-to-one correspondence with physical anticyclonic, cyclonic, and dipolar eddies.

This three-way categorization avoids a potential ambiguity of how to deal with partly asymmetric features. In the data one sees events which clearly have a monopolar form, and others which clearly have a dipolar form, but the transition between these two extremes is ambiguous. The phase angle provides a useful cutoff for when an event is too asymmetric to be considered as

[10] For the dipole, the vorticity magnitude extrema in between the speed maxima will be considered, rather than the vorticity magnitude extrema at the dipole's "radius of discontinuity".

monopole-like. From this point of view dipolar events are counted as being neither anticyclonic events nor cyclonic events. Varying the choice of cutoff between $\pi/2$ (zero dipolar events) and $\pi/4$ does not qualitatively change the results.

Because the complex-valued wavelet transform can "see" partly asymmetic features, the locations τ_* of, say, an anticyclonic event center need not occur at a local sea surface height maximum. It is therefore useful to define an adjusted location

$$\tilde{\tau}_* \equiv \begin{cases} \tau_* + \frac{\phi_*}{\pi}\frac{a_*}{m} & |\phi_*| < \pi/3 \\ \tau_* - \frac{\phi_*}{\pi}\frac{a_*}{m} & |\phi_*| > 2\pi/3 \\ \tau_* + \frac{\phi_* - \pi/2}{\pi}\frac{a_*}{m} & \pi/3 > |\phi_*| > 2\pi/3 \end{cases}$$

which shifts the location of an event by an amount proportional to its phase. This adjusted center returns the approximate location of the local sea surface height maximum associated with a "positive even" event, the local minimum associated with a "negative even" event, and the zero-crossing associated with an odd event.

An illustration of the signal anomaly definition is shown in Fig. 27 for the descending track nearest the mooring (see Fig 24). Monopolar-like features show up as elongated teardrops on the time-frequency plane, whereas a more oscillatory feature would result in a horizontal "band" of increased transform amplitude. Marked events in the lower panel meet the definition of an isolated anomaly (5.21) — that is, the wavelet spectrum takes on a local maximum over the indicated box-shaped regions — and have $Z_* > 0.1$ and $\delta_* > 5$ cm.

5.3.5. Application to altimeter data

Applying the above analysis to the alongtrack sea surface height data results in a set of points (τ_*, a_*) marking isolated signal anomalies, which we will henceforth refer to simply as "events" for brevity. The detected events can be sorted according to both scale a_* and strength $|\delta_*|$, resulting in a two-dimensional histogram (Fig. 28a) for all even events located within the Labrador Sea interior (defined in Fig. 24). Both axes are logarithmic, and the bin width is uniform along the logarithmic axes. Each point $(a, |\delta|)$ in Fig. 28a therefore represents the number of events whose magnitude is within a certain fraction of $|\delta|$ and whose scale is within a certain fraction of a. The anomaly histogram shows a definite ridge, with an increased occurrence of events at a given value of $|\delta_*|$ apparent in a "tongue" centered on about 20 km.

The scale/magnitude locations of eddies observed by the moorings (and one by hydrographic survey) as reported in Section 4 are also marked; the SSH anomaly is approximated from the estimated peak azimuthal velocity V and the estimated radius R through (5.19). The ridge of increased anomaly concentration aligns well with the locations of observed coherent eddies, suggesting a correspondence between the two. All of the circles visible on this plot are for the "Irminger ring" type eddies. Due to their smaller size and weaker currents, the estimated sea surface height excursions associated with the "convective lens" type eddies are smaller than 5 cm. It therefore does not appear that individual eddies of the latter type can be differentiated from instrument noise.

The distribution of events in the data can be compared with that expected due to instrument noise. A time series of Gaussian white noise with this standard deviation 3.1 cm (see Section 5.2) is constructed. Ten realizations of this noise dataset are formed having the same size as the original dataset. Missing data points in the original data are left in place to preserve the large-scale spatial structure of the domain. The noise datasets are then filtered with the same filter that was applied to the actual data, and then the event census algorithm is applied. The result is the distribution of events that would be expected if the data consisted entirely of uncorrelated instrument noise.

The scale-magnitude histogram, averaged over the ten realizations of the noise dataset, is shown in Fig. 28b. Events are concentrated at small scale and small magnitude, where the number of events observed in the noise census is far larger than in the data census. However the event concentrations decay rapidly toward large magnitude and large scale, and no sign of a "ridge" is evident here as was seen in the data census. The thick solid line in both panels is the contour above which the event concentration in the data census is at least ten times that in the noise census. Events in the data having a magnitude greater than 10 cm are therefore highly statistically significant.

It therefore seems reasonable that a subset of the isolated anomalies could be extracted and loosely identified with coherent eddies. Such a subset should contain features which are clearly not noise and which are expected to be dynamically meaningful. Here the former will be ensured with a cutoff value of $|\delta_*| > 10$ cm, and the latter with a cutoff value of the estimated Rossby number $|Z_*| > 0.1$. These cutoff lines are shown in Fig. 28. Note that a line of constant Z_* on the (δ_*, a_*) plane will be different for even and odd events, due to the definition of Z_*. The diagonal solid and dashed lines in Fig. 28 mark a value of $Z_* = 0.1$ for the even and odd events, respectively. The Z_* and the δ_* cutoff together define a statistically significant subset of events straddling the histogram peak. This subset will be referred to as the "eddy band", a detailed examination of which is the subject of Section 6.

5.4. Eddy property and population estimators

The algorithm described in the preceding subsection returns estimates of the magnitude and apparent radii of individual sea surface height anomalies, but we are more interested in the magnitudes, radii, and (most importantly) number density of actual physical eddies being observed. In this subsection, the event census is used to form estimators for the number, sizes, and strengths of eddies having sea surface height anomalies exceeding a specified cutoff. Although the primary interest here is the number of eddies present, it will be found that estimates of the eddy characteristics are also necessary. At the end of this section it will be possible to constrain estimates of eddy populations within confidence intervals.

As a simplification, we consider the problem of estimating the populations of arbitrary numbers of independent monopolar eddies having the $\frac{1}{2}\lambda$ form. Furthermore the estimators will be entirely based on the output of the census algorithm (δ_* and R_*), in order to bypass additional processing of the sea surface height profiles themselves. It will be argued that this approach is adequate for the purpose of estimating eddy populations. The interpretation of these estimators for the dipolar class of events will be postponed until the next section.

While the chain of reasoning in creating these estimators is straightforward, the details are somewhat involved. In the following, we present the initial assumptions the resulting estimators. This should provide a sufficient basis for recreating the numerical algorithms, which are based on the manipulation of the sea surface height profile and the corresponding inverse function. Readers interested in addional details are referred to Lilly (2002), with some corrections to be found in Appendix D.

5.4.1. Wavelet algorithm performance

The first step is to examine how the wavelet algorithm is performing. Assume an eddy having the form of the $\frac{1}{2}\lambda$ monopole with radius R_o and maximum sea surface height excursion δ_o (assumed positive in this section) is sampled by the altimeter along a single track. The values of R_* and δ_* obtained will be functions of the track's x-intercept (denoted X) with respect to

the eddy's center

$$\delta_* = \delta_o \, d_\delta(X/R_o) \tag{5.26}$$

$$R_* = R_o \, d_R(X/R_o) \tag{5.27}$$

and will be termed the wavelet "response functions". These will be determined by numerically testing the algorithm, sampling synthetic eddies every 5.7 km alongtrack as in the actual altimeter data.

Figure 29 shows R_* and δ_* versus track x-intercept normalized by the eddy radius, for unit magnitude eddies and a variety of radii and slice locations (see figure caption for values). The estimated sea surface height anomalies δ_* and the sea surface height profile are indistinguishable from one another (Fig. 29a). This means that the wavelet transform is returning the correct value of the sea surface height anomaly when the sample monopole is sliced at any location, not only through its exact center as required by the calibration. The function $d_\delta(X/R_o)$ in (5.26) is therefore just the sea surface height profile of the eddy.

The apparent radius for the monopolar form increases with X after an initial slight decrease (Fig. 29b, thin black line). The eddy then appears broader as the slice moves farther away from the eddy center. The apparent radius estimates R_* obtained from the wavelet algorithm (symbols) show a similar trend to the true apparent radius curve, but underestimate the apparent radius at large slice distances and overestimate it at small slice distances. There is a considerable amount of scatter in the wavelet estimates, most likely due to the coarseness of the alongtrack sampling. No sign of the decrease near $X/R_o = 1$ is seen in the R_* values.

The wavelet radius estimates R_* can be approximated by a straight line between X/R_o=1 and $X/R_o \approx 5$. This suggests a curve fit of the form

$$\frac{R_*}{R_o} = d_R\left(\frac{X}{R_o}\right) \equiv \begin{cases} 1 & \frac{X}{R_o} < 1 \\ m\frac{X}{R_o} + b & \frac{X}{R_o} > 1 \end{cases} \tag{5.28}$$

which has minimum mean square error for $1 < X/R_o < 5$ when $m = 0.356$ and $b = 0.962$. This curve (thick dashed line) compares well with the symbols, and will be used to idealize the wavelet algorithm response. The bias of this curve at large values of X/R_o is not particularly important, because such events on the periphery of eddies will end up being rejected by the event census on account of their small $|\delta_*|$ values.

5.4.2. "Inverse expectation" estimators

Let the ocean be sampled by a grid of altimeter tracks, running both east–west and north–south, with an intertrack spacing L of 100 km. Assume that the location of an eddy's center is a random variable uniformly distributed over the plane, and consider all events in the altimeter data having $|\delta_*|$ greater than some cutoff value δ_c. Also, we denote the "cutoff radius" R_c by the radius within which $|\delta_*|$ exceeds δ_c for a particular choice of δ_o and R_o. From the "response functions" it is possible to determine exactly the expected value of (δ_*, R_*), for a given δ_c, due to the presence of a $\frac{1}{2}\lambda$ eddy having properties (δ_o, R_o). If one excludes the unphysical case of extremely large-amplitude but small radius eddies, one finds this relationship is invertible; that is, an expected value of (δ_*, R_*) for a given δ_c determines the properties (δ_o, R_o) of the underlying eddy. Therefore, replacing the expectation in this inverse operation with an average over samples, we now have estimators — denoted $\hat{\delta}, \hat{R}$ — for the true eddy properties based on the observations. This is accomplished numerically through the construction of the response functions and their inverse functions.

The estimator functions are shown in Fig. 30. From mean values $(\overline{|\delta_*|}, \overline{R_*})$ over a set of observations for which $|\delta_*| > \delta_c$, these curves may be used to look up the estimates $\hat{\delta}$ and $\hat{R}$

of δ_o and R_o. Also shown are the results of numerical trials in which an eddy was randomly sampled with slice x-intercept X uniformly distributed between zero and R_c. Twenty trials were performed for each of a number of different parameter sets (given in the figure caption) and the mean values $\overline{\delta_*}$ and $\overline{R_*}$ over the twenty trials are plotted as symbols. Agreement with the predicted curves is generally good, although some error is evident, particularly for R_o when $\overline{\delta_*}$ is small compared with δ_c. Also shown are the δ_o estimator curves for a 1λ and a $\frac{1}{4}\lambda$ eddy; it appears the inverse expectation estimator for δ_o is relatively insensitive to the specific choice of eddy form.

5.4.3. Eddy population estimates

Let N be the number of times the altimeter grid samples an eddy field, with each sample being termed a "cycle". The true number of eddies present within a specified region during the time period of interest is n_o, and the average number of eddy events observed per cycle is $\overline{n}_\star$. These quantities n_o and $\overline{n}_\star$ will be referred to as the "eddy population" and "event count" respectively. The goal is first to find the statistics of the event count $\overline{n}_*$ for a known eddy population n_o, and second to find an estimator for n_o in terms of $\overline{n}_*$.

Assume that one eddy exists in an $L \times L$ grid box, and that the location of its center is a random variable uniformly distributed over the box; a sketch of this situation is shown in Fig. 31a. The statistics of the eddy sampled by the entire grid (not only the tracks forming the box boundary) will be considered. Because the relevant random variable is the offset between the grid and the eddy, it is equivalent to sample a fixed eddy with a grid having a crossover point uniformly distributed over an $L \times L$ box centered on the eddy.

Figure 31b shows an eddy of radius $R_o = 10$ km and cutoff radius of $R_c = 20$ km located at the origin. Either zero, one, or two eddy events will be reported by the census algorithm during a single cycle, depending on the location of the crossover point. When the crossover point is located within the region ($|x| < 20$ km, $|y| < 20$ km), two events are reported, because both the east-west and the north-south tracks observe events having $|\delta_*| > \delta_c$. When the crossover point is located in squares of width 30 km located in the corners of the distribution box, zero events are reported because neither track will intersect the cutoff radius. In the remaining area, one of the two tracks sees an event with $|\delta_*| > \delta_c$ and the other does not.

The statistics of the number of observed events will therefore be a function of $B \equiv 2R_c/L$, the ratio of the eddy diameter to the box side length. If a single eddy is present the probability that i events are observed in a single cycle is

$$p_i^{(1)} \equiv \begin{cases} (1-B)^2 & i = 0 \\ 2B(1-B) & i = 1 \\ B^2 & i = 2 \\ 0 & i \neq 0, 1, 2 \end{cases} \tag{5.29}$$

with mean and variance given by

$$\mu_{(1)} \equiv \mathrm{E}\{n_*\} = 2B \tag{5.30}$$

$$\sigma^2_{(1)} \equiv \mathrm{var}\{n_*\} = 2B(1-B). \tag{5.31}$$

The mean is linear with B, and equals one when $R_c = L/4$. The standard deviation is parabolic, going to zero at $R_c = 0$ and $R_c = L/2$. Note we have assumed that $R_c < L/2$, that is, its cutoff radius does not span more than one grid box; this assumption is certainly valid for the parameter space under consideration.

The probability $p_i^{(N)}$ that i events will be observed during N cycles due to the presence of a

single eddy may be expressed by a convolution

$$p_i^{(N)} = p_0^{(1)} p_i^{(N-1)} + p_1^{(1)} p_{i-1}^{(N-1)} + p_2^{(1)} p_{i-2}^{(N-1)} \tag{5.32}$$

which may be solved recursively for arbitrary N using (5.29). The probability distribution function for the average number of events observed per cycle is therefore

$$f(\overline{n}_*) \equiv \sum_{i=0}^{2N} p_i^{(N)} \, \Delta(\overline{n}_* - i/N) \tag{5.33}$$

and consists of a chain of Dirac delta functions (denoted $\Delta(x)$) located at $[0, 1/N, ...2 - 1/N, 2]$. By the central limit theorem, (5.33) converges for large N to a Gaussian having mean $2B$ and variance $2B(1-B)/N$.

The next step is determining the probability density function for arbitrary numbers of eddies spread out over an arbitrary area. We assume that the eddies have identical cutoff radii, and that the observations of each eddy are unaffected by the existence of the other eddies. Although we suspect from dynamics that complete independence will not hold, it is a reasonable simplifying assumption, particularly for sparse eddy fields. Under these conditions (5.33) still determines the correct probability density function for $\overline{n}_*$, provided $n_o N$ (eddies present per cycle times number of cycles) is used in the place of N.

The expected value of the event count over N cycles for an arbitrary number n_o of independent eddies with identical R_c is then simply

$$\mu_{(N)} = \mathrm{E}\{n_*\} = 2 n_o B. \tag{5.34}$$

Rearranging and replacing the expectation with an average over samples leads to

$$\hat{n} = \frac{\overline{n}_*}{2B} = \frac{\overline{n}_* L}{4 R_c} \tag{5.35}$$

which is an estimate of n_o based on the event census. This amounts to multiplying the observed eddy count by a "bias factor", $1/(2B)$, which accounts for the linear dependence of the event count on the cutoff radius. If R_c may be taken to be a constant in (5.35), one may compute confidence intervals on the eddy population estimate $\hat{n}$ using the probability distribution of $\overline{n}_*$ (5.33).

In practice, R_c is neither known nor likely to be a constant. Randomness of R_c will influence the estimate $\hat{n}$ in two ways, first since the probability density function for $\overline{n}_*$ is modified by a random B, and second through the randomness of R_c directly in (5.35). These effects were worked out analytically by Lilly (2002), who concluded that both are generally negligible in comparison to the randomness of $\overline{n}_*$ itself. The neglect of the randomness of R_c was also tested a posteriori therein; it was found that the event count and the estimated eddy population have strongly correlated distributions, confirming that for the Labrador Sea interior region the randomness of $\hat{n}$ is primarily controlled by that of $\overline{n}_*$.

Letting $X/R_o = D_\delta(\delta_*/\delta_o)$ be the inverse function to the sea surface height profile function (5.26), the cutoff radius may be estimated by

$$\hat{R}_c = \hat{R} \, D_\delta(\delta_c/|\hat{\delta}|). \tag{5.36}$$

where $\hat{R}$ and $\hat{\delta}$ are the "inverse expectation" estimates described in the preceding subsection. Note that the estimates $\hat{n}$, $\hat{R}$, $\hat{\delta}$ are all formed by averaging over the identical set of events occurring within a specified area and time period and having $|\delta_*|$ exceeding a cutoff δ_c. After substituting $\widehat{R}_c$ for R_c in (5.33), the eddy population may be estimated and confidence limits computed, as desired.

5.5. Summary

In order to address questions of spatial representativeness, a method for a parallel eddy census using satellite altimetry was developed, which was again based on signal anomalies in the continuous wavelet transform. The development proceeded as follows:

- Estimates of "apparent" radius R_*, sea surface height anomaly δ_*, and nondimensional vorticity anomaly Z_* were created which were shown to recover correct values for sample monopolar and dipolar eddies sliced along their axes of symmetry.
- A subset of sea surface height anomalies in the Labrador Sea altimeter data with $|\delta_*| >$ 10 cm, $|Z_*| > 0.1$ was isolated for further investigation, and sorted into upward excursions, downward excursions, and odd or dipole-like forms.
- This set of "eddy-band" events compares favorably in its parameter distribution to the Irminger ring type eddies observed by the moorings, while the convective lens type eddies fall below the $|\delta_*| = 10$ cm sea surface height anomaly cutoff.
- Comparison with a noise model shows that events within this band are extremely unlikely to be the result of instrument noise, with zero such events occuring in a noise dataset ten times the same size of the original dataset.
- If events in this "eddy band" are indeed due to observations of one or a number of coherent eddies of an assumed form, it is possible to estimate the eddy populations and to constrain this estimate within confidence limits, as was shown through the use of a statistical model.

In the next section these methods are applied to the study of the Labrador Sea eddy field.

6. Application and results of the altimeter census

6.1. Introduction

The physical results of Section 4, based primarily on data from two nearby moorings in the south-central Labrador Sea, left open the important question of spatial variability. This was the impetus behind the development, in the previous section, of an algorithm for performing an automated census of eddy-like events in alongtrack altimeter data. It is hoped that from "global" measurements of a single variable— the sea surface height— questions of spatial variability can be addressed which a fixed mooring cannot answer. The present section examines the Labrador Sea eddy field using TOPEX/Poseidon altimeter data, and attempts to unify the mooring and altimeter perspectives. However, it was found in the previous section that the altimeter is able to capture eddies of the Irminger ring type, but that the convectively-formed eddies are probably below the instrument noise level. Thus we expect the present section will shed light on the origin and variability of the former type.

The Labrador Sea has a complicated boundary current system with both vertical and cross-slope structure. Nearest the surface, the shelf-break currents accumulate freshwater (Khatiwala et al. 2002) as they transit the perimeter of the Labrador Sea. Moving deeper and offshore one finds the Irminger Current, with a warm, salty core at about 500 m depth trapped inshore of the 3000 m isobath. Speed estimates for the Irminger Current range from 12–15 cm s^{-1} from isobaric floats at about 700 m (Lavender et al. 2000) to 25–35 cm s^{-1} from surface drifters (Cuny et al. 2002). The northern Labrador Sea is the site of a well-known eddy kinetic energy [EKE, defined in (5.18)] maximum near 61.5° N, 52.5° W (Fig. 24). A substantial annual cycle of EKE is observed at this location which appears to be connected to the annual cycle in wind stress (White & Heywood 1995, Eden & Böning 2002). Indeed this location is part of a relatively

small fraction of the ocean over which the wind field appears to substantially influence the EKE variability (Stammer & Wunsch 1999).

Interpreting forms in the altimeter data as one-dimensional projections of two-dimensional (x, y) structures involves a number of ambiguous situations. A one-dimensional eddy-like bump or depression in the sea surface could be the result of an azimuthally symmetric eddy in the ocean, a dipole sliced through only one of its cores, or a slice across a one-dimensional "filament". Less obviously, a "bump" in the sea surface height residual $\eta' = \eta - \eta_o$ can also be the result of displacing a step-like front from its time mean position, because the latter is indistinguishable from the geoid and is included in the reference term η_o. While the Irminger Current generally tends to be trapped inshore of the 3 km isobath, it may occasionally extend southward near the EKE maximum (Cuny et al. 2002). These difficulties in interpreting individual sea surface height anomalies should be kept in mind. For this reason we choose to deal directly with the signal forms for as long as possible, only creating a physical interpretation at the end of the analysis.

6.2. A first look at the "eddy band" events

At the end of the last section, a subset of localized sea surface height anomalies was extracted from the alongtrack data. This highly statistically significant subset of events is referred to as the "eddy band" and is expected to include sea surface anomalies due to Irminger ring type eddies, but to exclude those due to convective lens type eddies. Such sea surface height anomalies were characterized in terms of their apparent core radius R_*, peak-to-trough anomaly amplitude δ_*, evenness or oddness measured by a phase angle ϕ_*, and dimensionless vorticity or Rossby number estimate Z_*. The phase angle ϕ_* was used to further classify anomalies into three categories: positive even ("anticyclonic") events, negative even ("cyclonic") events, and odd ("dipolar") events. The term "event" is used to emphasize that this classification merely describes the form of a sea surface height anomaly, rather than being a diagnosis of the underlying physical structure.

6.2.1. Probability distributions

The probability distribution of the eddy band events in the Labrador Sea interior is shown in Fig. 32. Events in the eddy band tend to be concentrated in a range of R_* between 20 km and 30 km. The total number of events peaks at $R_* = 22.8$ km, corresponding to a diameter of eight altimeter data points (with a 5.7 km spacing). About two thousand such events occur over the seven-year period 1994–2000, with the event cores — defined as the area less than R_* distant from an event center — covering, on average, roughly 5% of the surface of the Labrador Sea interior. The populations of cyclonic and dipolar events are comparable to each other, while roughly half of all events in the eddy band are of the anticyclonic type. By comparison, in the previous section it was found that modeling the instrument noise as a 3.1 cm standard deviation Gaussian process led to zero events breaching the $|Z_*| > 0.1$, $|\delta_*| > 10$ level for a noise dataset of the same size as the original dataset.

A cumulative histogram of event strength $|\delta_*|$, summed from large to small values in logarithmically-spaced bins, is shown in Fig. 32b. This includes all events in the Labrador Sea interior having $|Z_*| > 0.1$ and $|\delta_*| > 5$ cm, and so extends below the 10 cm cutoff defined for the eddy band. At very small values of $|\delta_*|$, the curves for anticyclonic and cyclonic events are close together, meaning that the numbers of events having $|\delta_*|$ greater than that value are comparable for the two types. However for $|\delta_*| > 10$ cm, the cyclonic curve is roughly a factor of two below the anticyclonic curve, with this disparity increasing towards large $|\delta_*|$. Dipolar events, however, become more frequent with respect to anticyclonic events towards larger values of $|\delta_*|$, and account for the largest-magnitude events observed. Note the rareness of very large magnitude

events, with only 10–30 events of each type having magnitudes exceeding $|\delta_*| = 30$ cm.

The ocean surface thus tends to be organized into sea surface height anomalies having apparent radii of $\sim$ 20 km and magnitudes far exceeding the instrument noise level. This is a basic statement about the structure of the ocean surface considered as a one-dimensional time series. Even without knowledge of the existence of a deformation radius, one would begin to suspect ocean dynamics are at work.

6.2.2. Comparison with the mooring

The eddy-band events are compared with the Bravo mooring during 1998–1999 in Fig. 33. The TOPEX track segment shown in the upper panel is from the descending track nearest the mooring (passing within about 14 km), with the locations of eddy band events along this track marked as symbols. Locations of confirmed coherent eddies from the mooring census of Section 4 are marked by horizontal lines in the lower panel. In both a mooring time series and an altimeter track, an eddy is expected to be a speed minimum flanked by two speed maxima. Comparing the mooring-based eddy census to the altimeter eddy-band events, one finds a very good correspondence. Five of the six confirmed eddies from the mooring census coincide with altimeter eddy-band events. Two others eddy-band events (during April) correspond to speed maxima at the mooring that were rejected from the mooring eddy census on account of their ambiguous appearance. During this time period, the mooring tends to observe a coherent eddy when an eddy-band event is seen nearby in the altimeter data. Thus, it appears that the Irminger ring type eddies are being observed by the altimeter, and that such large-magnitude eddies are a significant contributer to the altimeter EKE in the Labrador Sea interior. However during the years 1994–1996 in which the smaller, weaker "convective lens" eddies dominated the mooring data, direct comparison between the Bravo mooring and the altimeter (not shown) is not so favorable, again suggesting these eddies are not sufficiently above the noise level to allow them to be directly identified.

6.2.3. Sample events

To illustrate the types of events which are included in the eddy band, profiles of strong events from near the eddy-band histogram peak ($R_* = 22.8$ km) are shown in Fig. 34 for the Labrador Sea interior region. These events have been aligned at their center (phase-adjusted as described in Section 5.3.3), sorted according to magnitude, and offset in the vertical. Dipolar events have been flipped so that the positive flank is consistently placed to the right of the center.

For strong anticyclonic events having $|\delta_*| > 20$ cm (shown in black), there is no question that these appear to be profiles through dynamically meaningful features. Searching through the data for eddy-like events subjectively, one would pick out these features. For many of the strong cyclonic and dipolar events, that statement may also be made. Ambiguous events do exist, however, particularly as the amplitude of the events decreases. A particular case is noticeable in many of the cyclonic profiles, which could either be interpreted as downward depressions with a high on either side, or as two highs separated by a small distance. Such ambiguities cannot be definitively sorted out using alongtrack data alone, and an observer searching through the data would also need to make a decision about how to treat them. Overall the "thought process" of the automated census in classifying these forms seems acceptable.

The mean sea surface height and geostrophic crosstrack velocity profiles for all events in Fig. 34 having $\delta_* > 20$ cm are shown in Fig. 35. The lines $\pm R_* = 22.8$ km marking the estimated edges of the monopolar events coincide with the peak velocities, showing that the census is correctly estimating the apparent radius. The anticyclonic monopole profile is similar to the model eddy profile with a radius equal to $R_o = 22.8$ km, supporting the choice of model eddy. The anticyclonic and cyclonic events are not mirror images of each other, since the composite

anticyclonic event decays almost monotonically from its peak sea surface height anomaly, while the cyclonic event exhibits a high to either side of the central low. These are associated with peak crosstrack currents of roughly 40 cm s^{-1} and 35 cm s^{-1} respectively.

Events of this magnitude are likely to have currents penetrating to a significant depth. One could imagine a sea surface height anomaly due only to lesser density of water in the surface layer, with no horizontal pressure gradient present at depth. However, a 15 cm sea surface height excursion corresponds to density anomaly over 150 m of 1 kg m^{-3}. This is a very large signal; by comparison, the range of variability of vertically-averaged density over the top 150 m in the Labrador Sea interior has is about 0.1 kg m^{-3}, and the difference between the core of the fresh Labrador Current over the Labrador Shelf and the interior is 0.5–1 kg m^{-3}. The possibility that such dynamically compensated structures contribute to the eddy band is therefore considered slight.

6.2.4. Spatial distributions

The spatial distribution of the eddy-band events are shown in Fig. 36. To make these maps, every location along the altimeter tracks is marked each time it appears to be inside an eddy core. By "eddy core" will be meant the event's center plus or minus R_* along the altimeter track, for monopolar events, or plus or minus $\sqrt{2}R_*$ for dipolar events since these will be taken for simplicity to represent two oppositely-signed cores of apparent radius R_*. Linear interpolation is then performed separately for ascending and descending tracks, and these are then averaged together. The resulting maps express the percentage of altimeter cycles during which a given point appears to be "inside" an eddy, if all eddy-band events are interpreted as being slices through the centers of monopolar or dipolar eddies.

The spatial distribution of all events (Fig. 36a) has an obvious similarity with the EKE pattern (Fig. 24), with a maximum located near 61.5° N, 53° W in the West Greenland Current and a "ridge" stretching out from this point towards the southeast. The EKE pattern thus appears to be due in part to the localized, isolated excursions of the sea surface captured within the eddy band. Note that only a very weak maximum of event concentration is seen in the far southeast, in the direction of the North Atlantic Current.

The patterns for the anticyclonic events is similar in form to that for the total, and accounts for roughly half of the total at most locations. However, a strong asymmetry exists between the anticyclonic and cyclonic events, with the latter fewer in number everywhere. The maximum value of the cyclonic event concentration is only about 4%, less than half the value for the anticyclonic events. The "ridge" in the total event concentration is clearly apparent for the anticyclonic events, but is only vaguely defined for the other two types. This ridge reaches to the southeast where it connects with a secondary maximum located to the east of the Bravo mooring between 56° N and 57° N. At that secondary maximum a concentration of ~6% is seen for the anticyclonic events and half of that for the dipolar events, with the cyclonic event concentration falling to less than 2% and showing no sign of a localized maximum.

To examine the robustness of this pattern, the spatial structure of the total event concentration is shown in Fig. 37 for a partitioning of the eddy band according to event size and strength. The left- and right-hand columns contain events with $R_* < 20$ km and $R_* > 20$ km, respectively, and the rows beginning at the top contain events in the bands $10 < |\delta_*| < 15$, $15 < |\delta_*| < 20$, and $|\delta_*| > 20$. All concentrations have been normalized to a maximum of one for comparison. As the magnitude cutoff increases, events become increasingly concentrated around the EKE maximum. The ridge reaching to the southeast from the EKE maximum is primarily reflected in the distributions of the large radius events having $|\delta_*| < 20$ cm. Note that even for the dynamically weakest events— those having $|\delta_*| < 15$ cm and $R_* > 20$ km— a similar spatial

pattern appears, with enhanced concentrations along the axis of the EKE ridge, in the vicinity of the Bravo mooring, and near the North Atlantic Current to the southeast. Thus even the weaker events appear to represent ocean dynamics; were these events due to noise one would expect to see a more homogeneous distribution, as is indeed observed (not shown) for events below the 10 cm noise level.

6.3. Annual and interannual variability

Having established the basic properties of the eddy census in the previous section, this section will focus on temporal variability including quantitative eddy population estimates, together with understanding the physical implications of these results.

6.3.1. Latitude-time plots

The annual cycle of V_{EKE} is presented in terms of a latitude-time plot in Fig. 38a. Here V_{EKE} has been averaged in longitude from $x = -200$ to $x = 200$, and in overlapping latitude bands spaced every 25 km with 100 km latitudinal extent. In time, overlapping one-month blocks spaced every half month have been used. The value of V_{EKE} at the EKE maximum takes on a minimum value in July through October, followed by a increase in both strength (peaking in January–February) and in extent (peaking in April–May). The tilted axis of the EKE ridge during January–May suggests a southward propagation speed of $\sim$5 cm s^{-1}.

The eddy event concentration, including all events in the eddy band, is shown in Fig. 38b for an identical space-time grid as that used in panel (a). In order to make averages over different time and spatial domains comparable to each other, it is useful to express the event count in terms of the number of events per unit area per unit time. Here a "normalized event concentration" $\mathcal{N}$ is defined, which is the percent of time one expects to find one event in a fixed area chosen to be a box 100 km on a side. Counting the events in an area and a time interval of interest, this becomes

$$\mathcal{N} \equiv \frac{\text{Number of events}}{\text{Area / } 10^4 \text{ km}^2} \times \frac{1}{\text{Number of cycles}} \times 100.$$

Thus the maximum value of 80% at about 61°N in the winter means that the number of eddies observed is equivalent to finding a single eddy in a 100×100 km box 80% of the time.

The form of the event concentration is the same as that of the V_{EKE}, with a ridge again appearing to show a $\sim$5 cm s^{-1} southward propagation. At the latitude of the EKE maximum ($\sim$61°N), event concentrations range from 80% in January-February to $\sim$30% in May–August. Visible near the latitude of the Bravo mooring (dotted line) is a February–May period of increased event concentration, with a maximum value of $\sim$30% occurring during April.

Interannual variability is shown in the latitude-time plots of Fig. 39. The spatial grid is the same here as for the annual cycle plot, and the time grid consists of overlapping one-year blocks spaced every six months. V_{EKE} and the event density are again similar. Eddy speed and event concentration peaks are seen centered near the beginning of 1994, late 1998, and especially early 1997. The 1997 peak is the only one that appears to extend southward, with a $\sim$2 cm s^{-1} V_{EKE} increase and a $\Delta\mathcal{N}$=10% event concentration increase visible between 59° N and 60° N. This peak is the dominant event density feature at the latitude of the EKE maximum, with values in excess of $\mathcal{N}$=70% being double those recorded prior to 1995 and after mid–1999. Also visible in both fields, but more so in the event count, is a maximum centered on about 57° N — near the latitude of the Bravo mooring— after late 1998. V_{EKE} increases by $\sim$2 cm s^{-1} relative to other time periods withing the same latitude band, while the event concentration increases by roughly $\Delta\mathcal{N}$=20%.

6.3.2. Population estimates

To examine further details of the temporal variability of the eddy band, the statistical methods developed in Section 5 will now be employed. It was shown that if a set of coherent eddies is observed through the altimeter event census, it is possible to estimate the number of eddies present having sea surface height excursions greater than a specified cutoff, and to constrain these estimates within confidence intervals. The subset of events upon which these estimates are based is specified by the amplitude cutoff $|\delta_*| > \delta_c$. The sample size of eddy observations for which $|\delta_*| > \delta_c$ is expected to increase as the eddy's strength δ_o increases, and the confidence limits consequently grow tighter. The statistics are controlled by the eddy's "cutoff radius" R_c, which is the bounding radius between the inner region where the altimeter would observe an anomaly with $|\delta_*| > \delta_c$, and the outer region where $|\delta_*| < \delta_c$.

There are two important benefits to using this approach. The first is that it accounts for a sampling bias of the eddy count which tends to misrepresent the true number of eddies present. The second is that it allows the degree of certainty about the number of eddies to be assessed, so that the estimates may be constrained within confidence intervals.

The population estimates do not account for the sorting of events by phase into anticyclonic, cyclonic, and dipolar events, which required in Section 5 a somewhat arbitrary choice of phase cutoff. Population estimates will therefore be computed for each type of event separately. For the dipolar events the computation is the same as for the monopolar events, but the interpretation is somewhat different. A dipolar event will be thought of as representing two opposing cores; the population estimator is intended to approximately recover the true number of one type of core (say the anticyclonic cores) which are present. Thus it is not intended to indicate how many dipole-type eddies are present, which would require a more sophisticated model.

If the observed events are due to a group of monopolar eddies having identical R_c and the $\frac{1}{2}\lambda$ form shown in Fig. 25a, then the population estimates and confidence intervals will be exactly correct. If the cutoff radii vary or the form departs from the assumption, the model's results can be expected to be approximately correct. Population estimates will be formed for three sets of events corresponding to three choices of cutoff δ_c. These may be interpreted as the eddy populations with $|\delta_o| > \delta_c$ which would be required to generate the observations, if all events were indeed due to coherent eddies.

Population estimates are shown in Fig. 40, Fig. 41, and Fig. 42 for cutoffs of $\delta_c = 10$, $\delta_c = 15$, and $\delta_c = 20$ respectively. Annual cycles are given in the left panels and interannual variability in the right panels for each of three regions, the northern (top panels), central (center panels), and southern (bottom panels) boxes shown in Fig. 24. These boxes are each 2° in latitudinal extent and 400 km wide, and are centered on 61°, 59°, and 57° N respectively. The error bars shown are for the 90% confidence interval. Generally speaking, a population estimate will be said to be "significantly" higher than a certain value if the lower end of the confidence interval is approximately equal to this value; within the assumptions of the statistical model, the chance that the population is less than this value is only 5%. Futhermore, the term "significant peak" will be used to mean a maximum whose confidence interval does not overlap with the convidence interval from the minimum value within the same set of samples.

The population estimates for the annual cycle are computed as follows. For each region and each type of event, all events greater than the specified cutoff δ_c and occurring within a given month (but any year) are located. From this group of events a cutoff radius R_c is estimated from (5.36), and this value of R_c is then used to convert the number of events observed into an estimated eddy population using (5.35). Confidence intervals can be computed from (5.35) together with (5.33). For interannual variability, the same procedure is applied except that instead of sorting events by month, they are sorted into overlapping year-long periods centered

on January first and July first.

In the annual cycle with a cutoff of $\delta_c = 10$ cm (Fig. 40a,b,c), a few features are apparent. During most of year in all three regions, the anticyclone population is greater than that of either the cyclones or the dipolar cores and this difference is often statistically significant. In the northern region, there is a December maximum of estimated anticyclone population of 4 eddies, which is significantly different from the minimum of 2 eddies during June and July. In the cyclone population there is no December–January peak, but a significant peak does occur in May with a value of $\sim$3.5 eddies. Variability in the dipolar core population is much reduced compared to the monopoles. In the central region, all three estimated populations behave similarly, with a peak during December and a second peak during March. In the southern region, the most noticeable feature is now a statistically significant April peak for both the anticyclone and cyclone populations, with values of $\sim$3 and $\sim$2 respectively; smaller December peaks are also visible. Generally speaking, in moving from north to south one sees April replace December as the month of greatest estimated eddy populations.

A tendency with latitude is also seen in the interannual variability. Again the estimated anticyclone populations are generally speaking significantly higher than those of the other two types. In the northern region, a broad period of enhanced anticyclone populations is apparent from early 1996 through 1997, which is significantly greater than the populations in the time periods before and after. The cyclone populations, however, show almost the opposite behavior, being reduced during this time period and somewhat higher before and after. In the central region, the time period late-1996 through 1998 exhibits a highly statistically significant increase in the anticyclone population, with comparatively minor changes in the cyclone and dipolar core populations. Finally in the southern region, the entire time period mid-1997—2000 appears to have an enhanced anticyclone population relative to the earlier period, increasing from $\sim$1.5 to $\sim$2 eddies. The dominant feature seen in the interannual variability is therefore a multi-year increase in the anticyclone population, the beginning of which is delayed by roughly one year in the southernmost region compared with the northernmost.

Population estimates using a $\delta_c = 15$ cm cutoff are shown in Fig. 41. The estimated anticyclone population has a broad period of increased population during December–March in the northern region, with the high values of $\sim$2.5 eddies being statistically different from the 1.5 eddies observed during most of the rest of the year. January–April is a period of significant increase in the cyclone and dipolar core populations as well. The behavior in the central region is similar, although the annual cycle in the anticyclone population is now less well-defined. In the southern region values of the estimated anticyclone population are between about 0.5 and 0.7 except during January and especially February; the lower values during these two months are statistically different from those during the rest of the year.

In interannual variability, each of the three regions exhibits a dominant and highly statistically significant period of increased anticyclone population. In the northern region, a broad maximum peaking at $\sim$2.5 eddies during 1996–1997 is the dominant feature, and coincides with a much weaker ($\sim$1 eddy) but still significant maximum of the cyclone population. In the central region the estimated anticyclone population during 1997–1998 is nearly three times that before 1996 or after 1999, with minimal changes seen in the estimated dipolar core or cyclone populations. The southern region has the estimated anticyclone population increasing beginning in mid-1997, reaching a value of one during 1999— roughly four times the pre-1997 values, a highly statistically significant increase relative to those earlier levels.

Finally Fig. 42 shows the population estimates for a cutoff of $\delta_c = 20$ cm. The annual cycle in the northern region has the same character as in the previous two figures, with the anticyclone population taking on a maximum of $\sim$1.4 eddies during February. A very significant peak of $\sim$1

anticyclone occurs in the central region during March. In both the northern and central region the cyclone and dipolar core population estimates take on lower values during July–October or November than during the rest of the year, with this seasonal difference being statistically significant. In the southern region, populations are very low or zero with the exception of December spikes in the anticyclone and cyclone populations.

The interannual variability for the $\delta_c = 20$ cm cutoff shows the same qualitative pattern as in the $\delta_c = 15$ cm case, but with features tending to be more isolated in time. Highly statistically significant peaks of the anticyclone population are seen in the northern region during late 1996 through early 1997 (with a value of $\sim$1.5 eddies), in the central region during 1997 ($\sim$0.75 eddies), and after late 1998 in the southern region. Weaker increases in the cyclone population and sometimes in the dipolar core populations are seen in phase with the anticyclone population maxima.

To summarize, the population estimates show that the important features seen in the latitude-time plots are quantitatively significant. A seasonal cycle, interannual variability, the difference between anticyclone populations and the other events, and a latitudinal gradient of event concentrations: all these basic features are significant within the context of the statistical model, regardless of the choice of cutoff.

Specific features are worth noting. The annual cycle time / latitude plot (Fig. 38) shows the event concentration peaking annually between December and April, with the timing of the peak being delayed in the south relative to the north. The population estimates reveal a more complicated annual cycle. A shifted peak does seem to occur in the anticyclone populations, but the cyclone and dipolar core populations peak between February and April regardless of latitude or choice of cutoff. In the interannual time / latitude plot (Fig. 39), 1997 stood out as an extreme year in the northern and central regions, with elevated event concentrations after 1997 and especially during 1999 in the southern region. These results are confirmed by the population estimates, which also show an increase of estimated anticyclone populations after 1997 in the southern region for a weak ($\delta_c = 10$ cm) or medium ($\delta_c = 15$ cm) choice of cutoff. Interannual variability appear more concentrated around these specific times as the cutoff magnitude is increased.

If some considerable fraction of the eddy-band events do indeed correspond to coherent eddies, the results of this section show the Labrador Sea eddy field undergoes substantial annual and interannual variability. In Section 6.4 a physical interpretation of the event census results will be explored. However, before doing so it is useful to study a particular time period in more detail.

6.3.3. A case study

The annual cycle latitude/time plots (Fig. 38) appear to show a southward propagation of features from the EKE maximum into the Labrador Sea interior. Here we show this is supported by tracing individual features. Figure 43a is a scatterplot of anticyclonic eddy event observations versus latitude and time for a year-and-a-half long period centered on March 1999, together with the magnitude of these events versus latitude. The concentration of events north of 59° N and between November and March represents the annual intensification of the EKE maximum described above. In both panels the size of the circle is proportional to the event magnitude $|\delta_*|$, shown in panel (b) versus latitude. A set of events has been highlighted for emphasis, as will be discussed below.

Notice the two "stripes" south of 57.5° N during 1999, each representing a "chain" of multiple occurrences of large-amplitude upward sea excursions of $\sim$ 20 km radius. In plan view (Fig. 44) it can be seen that these two events are observed along two separate tracks, about 100 km apart,

in the vicinity of the Bravo mooring. It is difficult to escape the conclusion that these represent two separate, quasi-stationary anticyclonic eddies. Indeed, returning to Fig. 33, one finds that some of the altimeter events corresponding to the southern feature coincide with observations of Irminger ring type eddies at the Bravo mooring.

Looking backwards in time, the northern eddy can be traced backwards into large-magnitude features emanating from the EKE maximum. The path of the southern eddy, however, appears to be broken, with a lack of observations between 58.5° N and 57° N. The origin of these two eddies is more apparent in the plot of event magnitude versus latitude (Fig 43b). Here a continuous chain of events reaches backwards from the two persistent eddies south of 58.5° N to the very largest-magnitude events occurring in the source region. A gap is evident, both in latitude and in magnitude, between small-magnitude events that do not significantly extend south of 58.5° N, and large-magnitude events that do. In other words it is difficult to find a region in parameter space these two eddies could have evolved from, other than from the larger-magnitude events. To emphasize this apparently continuous chain of events, a combined magnitude, location, and time criterion has been used to highlight the same set of events in both panels.

Thus by looking at individual events, it appears we can trace back several of the Irminger ring type eddies to the very largest-amplitude eddy-band events in the EKE maximum of the boundary current. Similar continuous chains of cyclonic events (not shown) are seen extending southward to the vicinity of the Bravo mooring, particularly in 1993, just prior to the observations of the two cyclonic eddies at the mooring in late 1994. Thus it appears likely that the cyclonic events in the altimeter census contain as a subset a class of cyclonic eddies such as those observed at the mooring during 1994. This is consistent with the inferred origin of the warm eddies based on their θ/S properties (Lilly & Rhines 2002), which identifies them as containing water of Irminger current origin (though not their exact formation location as with the anticyclonic eddies).

6.4. A physical hypothesis

The accumulated evidence of the past section is that the eddy band of altimeter events, examined in different ways, does indeed appear to be largely representative of coherent eddies in the ocean. The results of the previous section then naturally imply the following scenario: the annual cycle of the intensification of the West Greenland Current EKE maximum during December–February is associated with an enhanced generation of anticyclonic Irminger ring type coherent eddies (and their cyclonic counterparts), which then propagate or are advected southward at about 5 cm s^{-1} until they reach the vicinity of the Bravo mooring around April–May, where some persist for six months or more. This scenario is in agreement with the water mass analysis of Section 4.4.1, which independently concluded that the Irminger rings originate in the vicinity of EKE maximum during winter. The decrease in the number of eddy-band events with time and with distance from the source region implies the destruction of eddies and/or their decay to parameter values outside the limits of the eddy band. The ratio of anticyclonic to cyclonic events increases with distance from the source region, suggesting the preferential destruction or decay of cyclonic eddies. In particular, a secondary EKE maximum to the east of the Bravo mooring which occurs during some years coincides with a concentration of exclusively anticyclonic eddies.

6.4.1. Comparison with the mooring variability

With this physical hypothesis in mind, it is useful to examine the relationship of the altimeter V_{EKE} measurements to the mooring observations (Fig. 45); wind stress forcing, derived from the NCEP model as described in Section 2, is also shown. Altimeter V_{EKE} from the three boxes marked in Fig. 24 are presented together with the V_{EKE} obtained by averaging EKE over

the 20 altimeter points nearest the mooring. The annual cycle, as already seen in Fig. 38, exhibits a January peak in the northern region but a smaller March–April peak in the central and southern regions. As discussed in Section 2, the mooring speed has a peak in May, with a sharp rise between March and April evident from both the Bravo / K1 mooring and other moorings. The altimeter V_{EKE} curve for the 20 points nearest the mooring is similar in form to the mooring speed annual cycle, but has a much smaller magnitude. (Lilly (2002) shows the agreement between these two curves becomes much better if temporal sampling and averaging are performed identically.) Thus the annual cycle of the mooring speed appears to be an expression of this larger-scale annual cycle of EKE and eddy populations, and therefore seems to have its origin in wintertime intensification of the boundary current EKE maximum.

Interannual altimeter V_{EKE} variations are roughly one-half the magnitude as in the annual cycle. In the northern and especially the central region, a maximum around 1997 stands out. A smaller maximum during 1999 occurs in the northern region but not in the central region. The most noticeable feature is a maximum during 1999 observed in the vicinity of the Bravo mooring, corresponding to an increase of $\sim$7 cm s^{-1}. However, averaging over the entire southern region, the magnitude of this maximum is much reduced. The mooring records, as mentioned earlier, show a tendency towards higher values at the Bravo / K1 mooring throughout the time period, with 1999 in particular standing out as a year of extremely strong currents; however, at the other moorings, current speed levels maintain those of the 1994–1996 Bravo / K1 moorings. The altimeter V_{EKE} picture is basically in agreement with this, showing a localized maximum near the Bravo / K1 location but only a small increase when a larger region is considered. Notice in particular in Fig. 24 that the locations of the additional moorings fall outside the limits of the secondary EKE maximum. It therefore appears that the interannual variability observed at the Bravo mooring is a localized feature, related to the increase in anticyclonic eddy populations in the southern region discussed above.

This last statement can be supported with estimates of the V_{EKE} due to the observed change in eddy populations. The observed average change in summertime (May–October) V_{EKE} between the two time periods 1994–1996 and 1997–1999 is $\sim$1.5 cm s^{-1}, where we have averaged over a circle of 160 km radius centered to the east of the Bravo mooring which encompasses the region of increased V_{EKE} (not shown). The corresponding increase in eddy population is roughly one (anticyclone), whether a 15 cm or a 10 cm cutoff is used. Considering a representative eddy of the $\frac{1}{2}\lambda$ eddy form having maximum azimuthal currents of $|V| = 40$ cm s^{-1} and a radius of $R_* = 20$ km, one finds the area-averaged speed of this eddy from its center to 160 km is $\sim$1.9 cm s^{-1}. This is about 25% higher than the observed speed increase. While these numbers are crude, it appears that the observed increase in eddy kinetic energy in the southern Labrador Sea is primarily due to existence of a few long-lived anticyclonic eddies.

Note that the annual V_{EKE} peak in the northern region— within the boundary current— is in phase the with annual peak in wind stress forcing, suggesting a wind-forcing induced instability of the boundary current. However, the interannual variability of V_{EKE} in the northern region does not show a simple relationship to the interannual variability of the wind stress forcing, as such a mechanism would imply. The issue of the cause of this interannual variability will be considered further in Section 7.

6.4.2. Heat transport

The annual and interannual variability of the EKE and eddy generation appears to have an impact on the hydrographic structure of the Labrador Sea. Recall in Section 2 (Fig. 3c,d) estimates of lateral heat fluxes were presented. Estimated lateral heat fluxes during 1997, derived from P-ALACE floats in the southern Labrador Sea, showed an April–May peak of $\sim$200 W m^{-2}.

This is precisely the timing of the arrival of the EKE signal and elevated eddy populations into this region. Further, interannual estimates of lateral heat fluxes have their maximum between June 1996 and June 1997, with a value of 84 W m^{-2}. This is again precisely the timing of the peak in the strong ($|\delta_*| > 15$ cm) and very strong ($|\delta_*| > 20$ cm) estimated anticyclonic eddy populations in the northern region.

One can estimate quantitatively whether the coherent eddies themselves appear to contain enough heat to account for the observed heat flux. In Section 4.4.5 it was estimated that an Irminger ring observed during July of 1998 had an anomalous heat content equivalent to 18 MJ m^{-2} when distributed over the entire interior of the Labrador Sea. At 5 cm s^{-1} it would take roughly 50 days for an eddy to cross one of the three regional boxes from north to south, so this is the approximate "flushing time" for all eddies to exit a region. Assuming that both anticyclonic eddies and dipolar cores have θ/S anomalies but cyclonic cores do not, the maximum number of heat-containing cores observed in the northern region during winter is between two and six, depending upon whether $|\delta_*| > 10$ cm or $|\delta_*| > 20$ cm is the appropriate choice of magnitude cutoff for heat-containing sea suface height anomalies. This gives a "flux" of eddies from the northern region to the central region of 2–6 eddy cores every 50 days, or one eddy every eight to twenty-five days, which corresponds to a heat flux of 0.26–0.82 GJ m^{-2} $year^{-1}$ or 8–26 W m^{-2}.

In the annual cycle during 1997, then, the eddies appear capable of accounting for at most about 12.5% of the maximum observed heat flux (200 W m^{-2}). Since the lateral fluxes during 1997 appear to be rougly twice as high as during the remainder of the 1990's, the contribution of coherent eddies to the lateral heat flux during an "average" year is at most ~25%. If the propagation velocity of 5 cm s^{-1} is appropriate for other times of year as well, then the heat flux estimate for the annual average during the one-year time period centered on January 1997 is also 8–26 W m^{-2}. This number is at most about 30% of the estimated average heat flux (84 W m^{-2}) during that time period. These numbers should be considered very rough; for example, if the "average" eddy radius is 30 km instead of 20 km, all heat fluxes are increased by over 100%. Nevertheless, based on these estimates it does not appear that coherent eddies whose sea surface height excursion magnitudes exceed ten centimeters can account for the bulk of the heat flux from the boundary current into the Labrador Sea interior.

6.5. Summary

An automated method for finding sea surface height anomalies in alongtrack TOPEX / Poseidon altimeter data, developed in Section 5, was applied to the Labrador Sea. This allowed a definition based on the form of a signal to substitute for the usual search for long-lived trackable features, which is particularly useful in a location such as the Labrador Sea where the dominant eddies are small comparable to the altimeter grid spacing. After examining basic features of the distribution and variability of the eddy band, a combination of the eddy-band results with the results from the previous sections of this study suggests a physical scenario of eddy formation and propagation which is consistent with all available information.

Close examination of the "eddy band" events in this and the preceding section supports their use as a proxy for localized oceanic structures. In particular, sea surface height profiles through Irminger ring type eddies are expected to be included as a subset of the eddy band. While ambiguous situations do exist, especially near the boundary current where excursions of the mean current could be aliased into the eddy band, in general one expects the distributions and variability of the eddy band to reflect those of the underlying eddy field.

Examining the distribution and variability of events in the eddy band, the following basic results were obtained:

- The spatial pattern of eddy-events concentrations (defined as the estimated percent time within one radius of an eddy's center) mimics that of the eddy kinetic energy, with maximum values of 20% within the West Greenland EKE maximum, a "ridge" of high values extending to the southeast, a secondary maximum of 10% located to the east of the Bravo mooring.

- The eddy-event concentrations exhibit a strong asymmetry between "anticyclonic" (upward) events and "cyclonic" (downward) events, with the former occurring roughly twice as frequently as the latter.

- An annual cycle of intensification of the West Greenland EKE maximum begins in November–December and peaks in January, with contemporaneous increases in the eddy-event concentrations, and a southward expansion of both fields during January–March of $\sim$' 5 cm s^{-1}.

- Interannual variability in both V_{EKE} and eddy-event concentration is dominated by a very large magnitude and broad (in latitude) 1997 maximum, together with the development of a secondary maximum in the southern Labrador Sea after 1997 and especially after 1999.

- Apparently continuous chains of eddy-band events are traceable backwards from Irminger rings at the Bravo mooring during 1999 to the very largest magnitude anticyclonic events in the West Greenland EKE maximum the previous December–January.

This last point agrees exactly with the location of the Irminger ring formation inferred independently from water mass properties in Section 4.4.1. A physical hypothesis suggested by these results, and consistent with the results of Section 2 and Section 4, is that the variability of eddy-event concentrations reflects the seasonal formation, propagation, and decay of (primarily anticyclonic) coherent eddies, together with the interannual modulation of this process.

Applying the statistical methods of Section 5 to infer eddy populations then leads to the following additional statements:

- Generally speaking, the important features of seasonal and interannual variability, spatial distributions, and differences between "anticyclonic" and "cyclonic" events mentioned above are significant within the context of the statistical model.

- The estimated eddy populations were found to decrease from a maximum of 2–8 in the northern region to 0–2 in the southern region, with an estimated associated heat transport of 8–26 W m^{-2}, at most about 25% of the estimated lateral heat flux inferred in Section 2.

- The observed 1.5 cm s^{-1} V_{EKE} increase during 1997–1999 relative to 1994–1996 is quantitatively consistent with the predicted 1.9 cm s^{-1} V_{EKE} due to the estimated population increase of $\sim$1 anticyclonic eddy.

The second point suggests an interesting mystery: why the heat and eddies arrive in the southern Labrador Sea contemporaneously (March–April) if the eddies are unable to carry the bulk of the heat within themselves. The apparent persistence of Irminger ring type eddies after 1997, inferred from the last point above, explains why only those mooring locations observed a speed increase, as documented in Section 2. The important unsolved mystery here is why the anticyclones persist in the later time period, specifically, whether the additional eddies are to be seen as a cause of the shallow convection or as a consequence. These issues will be returned to in the concluding discussion.

7. Discussion

This paper has examined the coherent eddy field in the Labrador Sea from an observational point of view. After an initial motivational look at basic features of the water mass and current variability, the bulk of the paper was concerned with the investigation of coherent eddy features in mooring and altimeter data, which necessitated the development of new analysis methods. Summaries of the main conclusions were given at the end of each section. In this section the main physical results and their implications will be discussed in more detail, together with an assessment about the current state of knowledge and suggestions for the future. Issues related to the convective lens type eddies will be discussed first, followed by the those related to the Irminger ring eddies.

7.1. Convective lenses

The analysis of eddy features in moored current meter data (Section 4) revealed about a dozen instances of a type of eddy termed a "convective lens" during 1994 through early 1998. These eddies have middepth-intensified currents of typically ~15–30 cm s^{-1} and radii of 5-15 km, with θ/S properties identifying them as originating in the interior Labrador Sea during deep convection. Three particularly interesting issues regarding these eddies are the details of their origin, the absence of cyclonic partners, and the frequent occurrence of vertically-aligned composite cores, each of which will now be discussed in turn.

7.1.1. Origin

The eddies of this type were shown to compare favorably with anticyclonic eddies observed in a numerical model involving the baroclinic instability of a dense column of water in the presence of a realistic background stratification. This supports the idea that such eddies could be formed by baroclinic instability of a localized region of especially deep convection, such as has been seen to exist on the Labrador side of the Labrador Sea during winter (Clarke & Gascard 1983, Pickart et al. 2002). It should be emphasized that these eddies are not expected to be a direct product of the geostrophic adjustment of a region of dense water, which would lead to barotropic currents having a cyclonic component; rather, they appear to be an indirect product of deep convection, with baroclinic instability providing the intermediate step.

The recent work of Dewar (2002) on convection in small basins [hereafter "CSB"] compares favorably with the structure of the anticyclonic eddies observed here, and offers additional clues as to their origin and importance. CSB examined in particular partial water column convection over a sloping bottom, the situation expected in the Labrador Sea. It was found that the sloping bottom disables the formation of first baroclinic mode hetons, so that eddy formation and geostrophic-turbulence type vortex interactions are primarily limited to second-mode structures. In our observations as well, the convective lenses are essentially second (or higher) mode structures. This is evidenced by their small scale, generally around the first deformation radius[11], as well as by their middepth velocity maxima [compare with the baroclinic mode vertical structures shown in Lilly and Rhines (2002)]. Additionally, as discussed below, the results of CSB bolster the interpretation of the composite core features, and also suggest a potential mechanism for explaining the absence of cyclonic eddies. The comparison between our results and those of CSB highlight areas for future work, clarifying the fundamental dynamics at work controlling Labrador Sea convection and its aftermath, with the meaning of the missing cyclones being an outstanding issue.

[11] One expects a "first mode" eddy to have a radius several times the first baroclinic deformation radius; see McWilliams (1985).

7.1.2. The missing cyclones

In models of the instability of a convected "patch", such as the one presented in Section 4.3.3, equal numbers of cyclones and anticyclones are generated. In our model, these cyclones are seen to contain a mixture of ambient water and convective water and so may be termed "cold cyclones". No example of such a feature is seen in the eddy census; the only two cyclones observed had warm, salty θ/S properties characteristic of the influence of the Irminger boundary current. With thirteen convective lens anticyclones observed over a five-year period and zero convected cyclones, one can be fairly certain this result is not merely due to chance. These observations should be understood as describing an "evolved state" of the eddy field, since we are usually unable to resolve coherent structures during the months of March and April when the currents are highly variable.

This fundamental difference between model and observation is one of the major major mysteries emerging from this work. It is an important point to clarify, as the structure of the eddy field will have implications for the eddy-driven water-mass dispersal and restratification. For instance, CSB proposes a mechanism by which the upper-layer cyclones could be drained from a region of deep convection through interaction with the shelf-break front followed by image propagation along a boundary, thus "stranding" anticyclones in the region of deep convection. This mechanism, while promising, was studied under idealized conditions — in particular, no boundary current was present — and therefore requires scrutiny in a more realistic setting in order to ascertain its importance in the Labrador Sea. Nevertheless, this illustrates that the dispersal of convected water could be substantially different than the now well-understood "hetonic" dispersal involving pairs of cyclones and anticyclones (Legg & Marshall 1993, Send & Marshall 1995, Jones & Marshall 1997). The residual eddy field left behind after convection thus offers clues to the nature of this dispersal process.

The greater populations of anticyclonic versus cyclonic coherent eddies is a well-established observational result in many areas of the world ocean (McWilliams 1985). However, there are many different physical reasons why this may be the case, so it is important to consider the observed asymmetry in the Labrador Sea within the context of the local dynamics. The most important question is whether the difference in populations is a matter of some difference in the formation of cyclones versus anticyclones, or whether it is a consequence of different evolution pathways between these two types of eddies; we mention several possible explanations below.

One possibility is nonlinear topographic "beta drift". Quasigeostrophic models show initially monopolar cyclonic (anticyclonic) eddies propagating to the northwest (southwest) due to a combination of the linear beta-drift (Nof 1981), and the formation of a weak dipole through "grabbing" fluid from the background gradient (Lam & Dritschel 2001). Such a mechanism may in fact sort anticyclonic from cyclonic eddies of Mediterranean water ("Meddies"). Schauer (1989) describes a cyclonic Meddy in detail and locates several other likely cyclonic Meddies in hydrographic and mooring data. All of these occur to the northwest of the Strait of Gibraltar, while anticyclonic Meddies are observed to the southwest. It is possible a similar "polarity sort" occurs in the Labrador Sea due to the analogous influence of the topographic β-effect, such as was seen in the numerical experiments of LaCasce (1998). The Bravo / K1 site is near a local maximum of the ocean depth, therefore even a relatively small amount of nonlinear topographic drift would be expected to trap anticyclones in this region. A second type of "polarity" sort is the shelf-break cyclone-draining mechanism of CSB, described above.

Another possibility is that convectively-generated cyclones are formed but have shorter lifetimes than the anticyclones. In fact, a handful of impulse-like features are observed at the mooring during March through May that could be due to self-advecting pairs of oppositely-signed eddies; such features are rejected by the eddy census since they have neither the form

of advected eddies nor water discernible mass anomalies with respect to the background. In the Mediterranean Sea as well, wintertime float tracks appear to show formation of both cyclones and anticyclones (Gascard 1978). This scenario is supported by modeling evidence that for deformation-scale eddies, anticyclones are more stable than are cyclones (Arai & Yamagata 1994). More specifically, cyclones may experience a convectively-induced instability (Legg and McWilliams, 1998) which could account for their rarity in the interior Labrador Sea.

Finally, it is possible that the instability of a narrow front, as in the chimney-collapse models, may lead to different kinds of eddy fields than do the gyre-scale variations in mixed layer depth observed in wintertime Labrador Sea. The model chimney in the numerical study reported here (Section 4.3.3) resembles the region of deepest convection observed during February of 1997 across the AR7W line in both size ($\sim$100 km) and the density difference between the chimney and the ambient Labrador Sea ($\sim$0.06 kg m^{-3}) but the width of the density front is less than 10 km in the model versus O(100) km in the observations. The importance of the frontal width to the eddies is perhaps suggested by the θ/S cores of the model cyclones (such as that in Fig 19), which are intermediate products resulting from vigorous near-surface mixing of the dense chimney with the ambient water during the initial stages of baroclinic instability.

7.1.3. Composite cores

An important detail of the structure of these convective lens is worth noting. More than half of the convective lenses — and all such events (eight) observed by three or more instruments over the depth interval 500–2500 m— had multiple (generally two) vertically aligned θ/S cores, some of which appear to have been formed during different winters. Although we are not aware of a formal survey of the occurrence of multiple cores in coherent eddies, an informal survey of the very large literature on Meddies [e.g, (Armi & Zenk 1984, Hebert, Oakey & Ruddick 1990, Pingree & LeCann 1993)] and other types of eddies [e.g., (Elliott & Sanford 1986, Riser, Owens, Rossby & Ebbesmeyer 1986, D'Asaro, Walker & Baker 1994)] turned up only a handful of reports of multiple cores. These are a very well observed double Meddy reported by Prater and Sanford (1994), another Meddy observed by Richardson, Walsh, Armi, Schröder & Price (1989), and two different types of double eddies observed in East Australia Current by Nilsson & Cresswell (1981) and Cresswell (1982). Therefore it appears that the convective lens eddies of the Labrador Sea are unusual in this sense.

An obvious way to make a double eddy is convection within a previously existing structure, which appears to explain those observed by Nilsson and Cresswell (1981). However, this is expected to lead to vertically uniform mixed layers, while the anticyclonic lens cores appear as extreme θ/S anomalies with smooth gradients both above and below (see Fig. 16a). The existence of double cores in the Meddies, on the other hand, is taken to indicate their formation (Richardson et al. 1989) in a region when the Mediterranean Undercurrent itself has a double maximum. Neither of these mechanisms explain the multiple cores of the Labrador Sea convective lenses.

Such composite instead appear to be a product of eddy-eddy interaction resulting in vertical alignment of originally distinct eddies of different densities, as seen in the laboratory and numerical experiments of Nof and Dewar (1994) and as was inferred to have occurred for two East Australia Current eddies by Cresswell (1982). This interpretation is supported by the fact that for some of the anticyclonic lenses, such as the one shown in (Fig. 16a), the θ/S properties of the upper and lower cores identify then as having been formed in two different winters, suggesting they were initially two separate eddies. Such a phenomenon may be seen as a manifestation of the tendency for baroclinic geostrophic turbulence to evolve into a more barotropic state (Rhines 1977, McWilliams 1984), that is, alignment of vortices reflects the tendency for vortex merger

(the "upscale cascade") for the case in which vortices have different densities. One expects the weakly stratified Labrador Sea environment to allow more barotropic currents and a greater degree of interaction between vertically-separated cores than is seen in other locations, as is also suggested in CSB. In that study, it was shown that like-signed vortex merger is expected for second-mode structures even in the presence of a sloping bottom, because (quoting CSB) "strong stratification under weak stratification makes second deformation [radius] anomalies behave as if in a flat-bottomed two-layer model." Thus the existence of composite cores in the convective lenses appears to have a consistent physical interpretation between model and observations.

7.2. Irminger rings

The mooring results showed that after mid-1997, a second type of eddy occurs with surface intensified currents of ~30–80 cm s^{-1} currents and radii of roughly 15–25 km. In Section 6, the census of eddy-like events in the TOPEX / Poseidon altimeter data revealed a seasonal cycle of the generation and propagation of these eddies, together with details of their interannual variability. Important issues regarding this type of eddy are the details of the generation, their tendency to be anticyclonic in polarity, the frequent occurrence of composite cores, their role in determining the energetics and water mass properties of the interior region, and the causes and implications of their interannual variability. These issues will be discussed in turn below.

7.2.1. Origin

In Section 4 it was shown that the θ/S properties of the "Irminger ring" type eddies identify them as originating in the West Greenland Current EKE maximum. The altimeter analysis (Section 6) confirmed the formation region, and revealed an annual cycle with an increase in anticyclonic eddies in the source region during December–February, followed by a southward propagation into the Labrador Sea interior at about 5 cm s^{-1}. In particular, long-lived eddies in the Labrador Sea interior during 1999 appear to evolve from the very strongest eddy events (25–40 cm sea surface height anomalies) observed in the source region the previous winter. This identification of the eddy formation region is also consistent with a previous study (Prater 2002) which observed eddy formation at the EKE maximum using both a sea surface temperature image and acoustically tracked floats. The sea surface temperature clearly shows a dipole being injected into the interior, the anticyclonic member of which contains boundary current water while the cyclonic member appears to wrap up interior water.

A scenario remarkably similar to that described above is apparent in the high-resolution numerical experiments of Eden and Böning (2002) [EB]. In that study, a region of enhanced eddy kinetic energy was found over the West Greenland Current, as in the altimeter observations, with good agreement in the EKE values between model and observations. The modeled EKE maximum has a seasonal cycle with a January–February maximum, as in the observations, and is associated with the generation of large-amplitude, primarily anticyclonic eddies. Both EKE and sea surface height variance show a tongue extending southward into the Labrador Sea interior, although the elongation of these patterns along the isobaths appears more pronounced in the model than in the observations. The anticyclonic eddies appear to propagate both around the isobaths, as well as drifting southward into the interior. Thus many of the essential results of our observational study appear to be well captured by the EB model.

Since the EB model was forced with monthly wind stresses, it is clear that the (high frequency) EKE maximum is due to an internal oceanic instability. A diagnosis of the energy transfer terms in that model shows the instability grows via a conversion of mean kinetic energy into eddy (perturbation) kinetic energy, and thus may be classified as a barotropic instability. The annual cycle in the EKE may thus be ascribed to a modulation of the strength of this barotropic instability, resulting from wind-induced changes in the current strength.

Exploring the nature of this instability and its role in the Labrador Sea is an important area for future research, in particular, the cause of interannual variability in eddy kinetic energy, eddy generation, and the associated heat fluxes. Here we saw that while the magnitude of annual and interannual variability of V_{EKE} are comparable, the annual cycle of wind stress far exceeds the magnitude of the interannual variability (Fig. 45), questioning the role of the wind on interannual time scales. However, it should be pointed out that the domain we have chosen for averaging the wind stress includes regions both positively and negatively correlated with the West Greenland Current EKE (Peter Brandt, personal communication), and thus may underestimate the interannual variability. The relationship of the eddy generation and EKE to the boundary current strength are discussed further below.

7.2.2. Polarity

In the mooring-based study (Section 4), the Irminger ring type eddies were found to be almost exclusively anticyclonic. The only exceptions were two cyclones having θ/S properties characteristic of the boundary current, observed during 1994. The altimeter study (Section 6) also showed an asymmetry in the populations of downwards versus upwards eddy-like excursions of the sea surface height. The altimeter "cyclonic events" were found to be fewer in number everywhere and more localized in their distribution around the EKE maximum. In particular, the secondary EKE maximum located to the east of the Bravo mooring during 1997–1999 was shown to be associated exclusively with anticyclonic events. The anticyclonic Irminger rings observed from the mooring are expected to be a subset of the anticyclonic events in the altimeter census, and the two cyclones to be a subset of the cyclonic events. Thus the asymmetry observed in the altimeter census suggests a generation of the anticyclonic Irminger rings at the EKE maximum together with their cyclonic counterparts, followed by a preferential destruction or decay of the cyclonic eddies with distance from the source region.

A number of studies have shown that anticyclones are more stable than cyclones on scales larger than the Rossby radius (Matsuura & Yamagata 1982, Cushman-Roisin & Tang 1990, Arai & Yamagata 1994, Cho & Polvani 1996). Additionally, for large "modon" type dipoles, the anticyclonic member is seen to be more stable, and such structures can evolve into anticyclonic monopoles (Dewar & Killworth 1995). Heat loss is also expected to have differing effects on cyclones and anticyclones. Most obviously, the buoyant eddies such as the Irminger rings, which have surface-trapped domes of warm, buoyant water, would be more resistant to convection than ambient water or cold-core eddies. Further, the effect of convection on a cyclone was examined numerically by Legg et al. (1998), showing that after the application of convective forcing the eddy became baroclinically unstable and soon disintegrated. While the reason for the observed difference in the anticyclone and cyclone distribution is not yet known, the effect of convection is certainly a leading candidate. Observations of the Irminger rings from the mooring and hydrographic data show roughly half of the heat content is eroded after a winter's convection. Since the cyclones most likely consist of a mixture of the Irminger water and interior Labrador Sea water, their heat content will be less than the anticyclones' and therefore they will be more susceptible to convection.

The anticyclonic rotation of these eddies is presumably due to the fact that, at the time of formation, these buoyant lenses occupy isopycnals which are nonexistent in the Labrador Sea interior, and consequently are expected to generate anticyclonic relative vorticity through vortex "squashing". An important point here is that intuition from subtropical currents such as the Gulf Stream is probably not useful. Such currents can develop large meanders, leading to "pinch-off" eddies that can take either sign depending on whether they are formed on the offshore or onshore side of the current. This does not appear to be the formation mechanism in

the Labrador Sea, where the currents appear to be trapped to the topography— drifter tracks, for example, follow bathymetric contours in smooth curves until they reach the EKE maximum, at which point their paths become more disordered (Cuny et al. 2002). It is more likely that the eddy formation in this region involves the sort of "injection" event captured by Prater (2002).

As was seen in Section 4, such long-lived, buoyant anticyclones are able to survive for over a year, resulting in initial deep mixed layers in a second winter after their thin surface stratification has been eroded. This method of generating relatively deep mixed layers is opposite from the usual notion that the deepest convection will initially occur within cyclonic eddies on account of their uplifted isopycnals. The existence of such long-lived, twice-convected anticyclones could be expected to have an impact on both the geography of deep convection and also on its integral effects. The interaction between the eddy field and convection, such as examined in the numerical experiments of Legg and McWilliams (2001) for roughly equal populations of cyclones and anticyclones, could be substantially different in the Labrador Sea.

7.2.3. Propagation

Another important issue is the mechanism by which the eddies propagate into the central Labrador Sea. The effect of the mean flow is only a few centimeters per second, and in any case appears to be flowing in the wrong direction to account for the movement of the eddies (Lavender et al. 2000). The most important issue here is whether the propagation occurs primarily due nonlinear topographic beta-drift (described above in connection with the convective cyclones), or due to dipolar-like self-advection of opposing cores. Within these two classes, there are a wide variety of dynamical possibilities, ranging from linear (westward) planetary beta-drift (Nof 1981), nonlinear (northwest/southwest) planetary (Lam & Dritschel 2001) and topographic (LaCasce 1998, Sutyrin 2001) beta-drift, f-plane dipoles, f-plane "quasi-monopoles" (Radko & Stern 2000), and beta-plane dipoles (Larichev & Reznik 1976, Sutyrin, Hesthaven, Lynov & Rasmussen 1994). While in theory one may be able to distinguish eddies organized into dipoles from those organized as monopoles using some statistical considerations, our simple categorization only permitted the classification of alongtrack sea surface height anomalies according to their form.

The location of the secondary EKE maximum to the east of the Bravo mooring, and the tendency for anticyclonic Irminger rings to persist there, can be understood as a "stalling" of these eddies regardless of their propagation mechanism. In this region cyclonic events in the altimeter census were shown to be very rare, apparently due to a lesser stability of cyclonic eddies as discussed above. The anticyclonic Irminger rings therefore have no opposing cyclonic features to pair with, and consequently can at most advect each other in circles. Furthermore, the region of this secondary EKE maximum corresponds to the localized depression of the topography, as seen in Fig. 2, and so anticyclones in this region could not escape via nonlinear topographic beta drift. However, it is unclear what combination of these two mechanisms conspires to make the region east of the Bravo / K1 mooring a preferential site for the persistence of long-lived anticyclones.

7.2.4. Vertically-aligned cores

As with the convective lenses, at least half of the twelve anticyclonic Irminger ring eddies appear to have double vertically-aligned cores. Unlike the convective lens eddies, temperature time series through both cores of the Irminger rings are often completely flat, evidence that these cores are homogenized in the vertical. In one case of a hydrographic profile through the center of an Irminger ring, the θ/S properties showed two ~400–500 m thick cores which must have been in contact with the surface for most of the winter in order to achieve such deep mixed layers; however, from the altimeter survey it was shown that the formation time of these eddies is early in the winter, around January. From these two lines of evidence it appears that the two

cores observed in this anomalous hydrographic cast were formed as two separate eddies, which later became vertically aligned after being exposed to several more months' worth of surface heat loss.

The explanation for the multiple cores in the observations of Nilsson and Cresswell (1981) — repeated cycles of convection followed by summertime restratification — can be ruled out here. The upper core of the eddy observed by the anomalous hydrographic profile (Fig. 20) is both too buoyant and too salty to have been created by one-dimensional restratification and then repeated convection, and the formation of an initially ~1.5 km deep mixed layer having the observed temperature of the lower core would be impossible in this region given realistic heat fluxes. However, it should be mentioned that eddy formation late in the winter could potentially also account for such double mixed-layer eddies. In this case, a core of partly convected Irminger Water ejected from the boundary current would find itself more buoyant than the already deep mixed layers in the Labrador Sea interior, perhaps leading to such "stacked" mixed layers. The inferred early winter formation time of the eddies, when convection is too shallow to have created the lower core, appears to discount this possibility. Thus, as in the case of the convective lenses, the most likely mechanism for explaining these multiple cores appears to be the alignment of initially distinct eddies having different densities.

7.2.5. Energetics and heat fluxes

A question of some importance to the study of deep convection is, "What is the energy source in a convecting region?" In "cold patch" type numerical experiments in which a localized buoyancy forcing is applied to the ocean (Jones & Marshall 1993), kinetic energy is seen to be generated locally though a conversion from potential energy via baroclinic instability. Legg and McWilliams (2001) extended such "cold patch" type experiments by applying a uniform cooling to a preexisting eddy field. In that experiment the domain-averaged kinetic energy was seen to level off to a constant value within a few days after the cessation of surface cooling. The kinetic energy then remained at a constant value for the remainder of the experiment, up to a month later. This was shown to be due to the transfer of energy from a large reservoir of available potential energy into kinetic energy. By contrast, the present results show that the springtime (March–May) increase in mooring speed and altimeter V_{EKE} in the southern Labrador Sea, which occur as the surface heat fluxes are changing sign and are beginning to warm the ocean, originate in an instability of the boundary current some three months prior to and four hundred kilometers distant from the time and place of deepest convection. This is a significant departure from the idea that the dominant source of energy in a convecting region is the conversion of locally-generated available potential energy.

Although the phase of the eddy population peaks are coincident with the March–April peak in the estimated lateral heat fluxes, the eddies themselves appear to be able to account for at most 25% of the necessary heat transport in the annual cycle. Similarly, the large interannual lateral heat flux spike in June 1996–July 1997 coincided with very large V_{EKE} values and estimated eddy populations in the vicinity of the West Greenland EKE maximum, yet again the eddies themselves were estimated to account for at most 30% of the necessary heat flux. Some other mechanism, such as eddies below the "noise level" of the altimeter observations, or a more disorganized filamentation process, or perhaps a change in the mean flow, appears necessary to account for the estimated heat fluxes. This presents a mystery, because while coherent eddies are capable of propagating at large velocities in the absence of a mean flow, as discussed above, such mechanisms would not be available to small-scale disorganized structures. On the other hand, another possibility is that the NCEP-derived lateral heat fluxes are biased. The question of why the heat arrives with the eddies, yet the eddies do not appear to be able to carry it

themselves, is an
important issue for future research.

7.3. Interannual variability

A brief discussion of existing observations in Section 2 showed the 1990's to be a time of remarkable change in the Labrador Sea. The early 1990's were characterized by deep convection to ~2 km, while in the later part of the decade convection was only half as deep. This change coincided with a deep warming of the water column, and with a freshening of the water column above the convection depth and salinization below. At the same time, currents at the Bravo / K1 site became increasingly more energetic; yet this appears to be a localized phenomenon, not observed at other mooring locations. The subsequent analysis of the eddy field showed these changes in the Labrador Sea interior to be related to fluctuations in the boundary current, and to a shift into a regime of long-lived Irminger ring type eddies in the interior.

7.3.1. Currents and altimeter V_{EKE}

It was shown that a tripling of speed from ~10 cm s^{-1} to about 30 cm s^{-1} at the Bravo / K1 moorings between 1994 and 1999, the absence of such an increase at other nearby moorings, and the ~1.5 cm s^{-1} rise in southern Labrador Sea altimeter V_{EKE} between 1994–1996 and 1997–1999, are all attributable to the persistence in the later time period of a handful of large-magnitude anticyclonic Irminger ring type eddies in the vicinity of the Bravo mooring. The development of a persistent eddy feature in the southern Labrador Sea after 1997 also has implications for interpreting the results of Lavender et al. (2000). Analyzing measurements from over 200 P-ALACE floats in the Labrador Sea region during 1997–1999, those authors found an O(100 km) anticyclonic feature in the central Labrador Sea with maximum currents of ~3 cm s^{-1}. The present results suggest that this large-scale circulation pattern may partly be a manifestation of the persistent anticyclonic eddies during this time period, reflecting the spatially averaged effect of energetic organization on the O(10 km) scale.

7.3.2. Transition to long-lived Irminger rings

The reason for the transition to long-lived Irminger ring type eddies after 1997, and the relationship of this transition to the shoaling of the depth of convection, is another important unanswered question. One possibility is that anticyclonic eddy persistence in the southern Labrador Sea is related to the magnitude of V_{EKE} or eddy generation at the source region; however, this idea does not appear to be supported by the available evidence. June 1996–June 1997 was a year of unusually high numbers of strong ($|\delta_*| > 15$ cm) anticyclone-like sea surface height excursions in the northern region (surrounding the EKE maximum), suggesting the generation of more strong eddies than usual during this time period and /or possibly an offshore shift in the boundary current from its time-mean position. These strong eddies were observed in the central region as well during roughly the same time period. In the southern region, however, no isolated peak during this time period is apparent— rather, the calendar year 1999 stands out as having exceptionally high anticyclonic eddy populations, which was not preceded by an unusually strong winter at the EKE maximum. The elevated numbers of anticyclones in the southern region is therefore ascribed to a greater longevity of these eddies, but does not appear related to any increase in the number or strength of eddies generated at the source region; conversely an increase in the number of strong eddies generated does not necessarily lead to increased populations in the southern region.

A more likely hypothesis is that the weak heat fluxes and shallow convection of the later part of the 1990's permitted the persistence of eddies which otherwise would have been destroyed. As discussed above, eddies of both signs would be expected to be destroyed by sufficiently deep

convection. However, support for this argument would require a greater understanding of the evolution of the anticyclonic eddies in the presence of convection. Therefore, the reason for the persistence of anticyclonic Irminger rings in the latter part of the 1990's remains an open question.

7.3.3. A boundary current-modulated heat pathway

The interannual variability of estimated lateral heat flux, eddy kinetic energy, and eddy generation suggests a mechanism by which the boundary current dynamics could modify the depth of convection. Here our attention is focussed on June 1996–June 1997, during which time period the estimated lateral heat flux (Section 2) was 84 W m^{-2}, twice the average value of all other years. A massive spike in EKE and in large-amplitude eddy events was observed by the altimeter in the vicinity of the EKE maximum during the same time period, suggesting an intensified boundary current instability during this time. It is natural to expect that the enhanced heat flux was a result of the enhanced instability. Therefore, extrapolating from the comparison with the Eden and Böning model described above, one has a scenario in which modifications of the strength of the boundary current lead to great instability and greater lateral heat fluxes, possibly impacting the depth of convection. However, as pointed out in Section 2, the majority of the additional 42 W m^{-2} during 1997 contributed to warming the water column without change in its stability against convection, although the depth of convection was still estimated to have been decreased by roughly 200 m on account of the additional (stabilizing) fluxes. Thus while the possibility of a boundary current-modulated heat pathway seems well established, its potential impact on deep convection is less clear.

7.4. Concluding remarks

The most important theme emerging from this work is the dominant role of the boundary current in shaping the energetics and water mass properties of the interior region. Following this observational study, attention may now turn to detailed comparison with numerical models, with particular emphasis on sampling models in similar ways to the available observations (current meter "moorings", for instance). Some important areas for future research are (i) the nature of the dispersal mechanism, and the meaning of the absence of convectively-generated cyclones, (ii) the mechanism of eddy propagation and associated heat transport into the Labrador Sea interior, (iii) the interaction between buoyant anticyclonic eddies and deep convection, and (iv) the nature of the boundary current instability and its potential role in modulating deep convection. Answering these questions would shed considerable light on the role of the Labrador Sea in the climate system.

Acknowledgments– The first author wishes to acknowledge helpful and inspiring conversations with the following people: Knut Aagaard, Boris Boubnov, Karl Bumke, Jerome Cuny, William Dewar, Jürgen Fischer, Rolf Käse, Jody Klymak, Sonya Legg, Seelye Martin, Felix Mosdorf, Donald Percival, Robert Pickart, Carlos Sena-Martins, Fiammetta Straneo, and Igor Yashayaev. Hydrographic data was collected, processed, and provided for use in this research by Allyn Clarke, Igor Yashayaev, Robert Pickart, and others. Mitsuhiro Kawase and Charles Eriksen read early versions of this manuscript and greatly improved it through their comments. The detailed comments of an anonymous reviewer were also much appreciated. J. Lilly and P. Rhines acknowledge the support of the Office of Naval Research (ONR) Physical Oceanography Program and the National Oceanic and Atmospheric Agency (NOAA) Atlantic Climate Change Program (ACCP). F. Schott and U. Send acknowledge Special Research Project (SFB) 460, "Dynamics

of Thermohaline Circulation qVariability", funded by Deutsche Forschunggemeinschaft (DFG). E. D'Asaro acknowledges Office of Naval Research (ONR) grant #N00014-94-1-0025

Appendix A. Processing of hydrographic data

It is useful to form a "mean" interior Labrador Sea water column from each of the springtime AR7W hydrographic sections. To do this, only those hydrographic profiles extending to at least 3300 m are used, and casts are rejected which have isopycnal depth anomalies greater than 300 m when trend of isopycnal depth with latitude is removed. The latter criterion excludes isolated eddies or boundary current contamination, but permits large-scale gradients; only a half-dozen points are rejected during the period 1990–1999. The end results is profiles of salinity and potential temperature for each year from 1990 to 1999 excluding 1991.

From the set of representative profiles, the depth of convection can be estimated as follows. Data are interpolated onto surfaces of constant potential density, and the thickness of each isopycnal layer is computed. The year-to-year thickness change as a function of isopycnal layer is then found by differencing the profiles in time at a fixed value of the potential density. Beneath the influence of surface restratification ($\sim$ 300 m), deep convection results in a thickening of isopycnals, but isopycnal exchange between convected interior water and boundary current water leads to a thinning of isopycnals. The depth of this boundary between thickening and thinning isopycnals— that is, the depth at which the time derivative of isopycnal layer thickness changes sign— is therefore a reasonable estimate of the depth of convection.

Appendix B. One-dimensional mixing and oceanic heat storage

A one-dimensional mixing model is often useful to assess the first order effects of convection on water mass properties. Expanding the *in situ* density ρ in terms of changes in potential temperature θ and salinity S yields the familiar equation

$$\Delta\rho = \rho_o\beta\Delta S - \rho_o\alpha\Delta\theta \tag{B.37}$$

Here α and β are the thermal expansion and haline contraction coefficients, respectively,

$$\alpha = -\frac{1}{\rho_o}\left.\frac{\partial\rho}{\partial\theta}\right|_{S,p} > 0 \quad \beta = \frac{1}{\rho_o}\left.\frac{\partial\rho}{\partial S}\right|_{\theta,p} > 0, \tag{B.38}$$

and $\rho(\theta, S, z)$ is the *in situ* density of a water parcel observed at depth $-z$. Note that the vertical coordinate z is defined positive upwards and that α and β are both functions of potential temperature θ.

It is helpful to consider a mechanically mixed layer of depth $-z_m$, the properties $(\bar{\theta}, \bar{S})$ of which are simply vertical averages

$$\bar{\theta}(z_m) = \frac{1}{-z_m}\int_{z_m}^{0}\theta(z')dz' \tag{B.39}$$

$$\bar{S}(z_m) = \frac{1}{-z_m}\int_{z_m}^{0}S(z')dz' \tag{B.40}$$

of the original water column; note that z_m is negative in the ocean so that $-z_m$ is a depth. The vertically-averaged properties can be considered a function of mixed layer depth, $\bar{\theta}(z_m)$ and $\bar{S}(z_m)$, which should not be confused with a vertical profile since z_m will be a function of time.

The properties of a marginally stable, vertically homogeneous mixed layer of depth $-z_m$ are denoted $\theta^*(z_m)$ and $S^*(z_m)$. In this simple model, vertical mixing will be assumed to be

complete, with no entrainment across the base of the mixed layer at depth $-z_m$. The difference between the properties of this mechanically-mixed layer and the marginally stable mixed layer are then

$$\Delta\Theta(z_m) = \bar{\theta}(z_m) - \theta^*(z_m) \tag{B.41}$$

$$\Delta\mathbf{S}(z_m) = \bar{S}(z_m) - S^*(z_m) \tag{B.42}$$

and will be referred to as the temperature change function and salinity change function, respectively. Since vertical mixing does not change the vertically-averaged properties, the difference between the vertically-averaged properties at a given depth and the properties of a marginally stable mixed layer must be due to surface fluxes. For simplicity, the surface fluxes are assumed to change the vertically-averaged salinity and temperature in a constant ratio $\gamma = \Delta\mathbf{S}/\Delta\Theta$.

The temperature change function can be found by comparing the density of the mechanically-mixed layer to that of the original water column:

$$\Delta\Theta(z_m) = \frac{\rho(\theta, S, z_m) - \rho(\bar{\theta}, \bar{S}, z_m)}{\rho_o\alpha\left(1 - \frac{\beta}{\alpha}\gamma\right)}$$

where α and β are now assumed to be constants or functions of pressure only. $\Delta\Theta(z_m)$ is therefore the temperature change necessary for a mechanically mixed layer of depth $-z_m$ to become marginally stable with respect to the underlying original water column at depths greater than $-z_m$. This change $\Delta\Theta(z_m)$ is a function of the surface fluxes, expressed through the ratio γ, and is defined to be positive when the water column cools.

The properties of the convective mixed layer (θ^*, S^*) are then given by (B.41) and (B.42). θ^* and S^* trace out a curve on the θ/S diagram followed by the evolving mixed layer. From a set of initial profiles these trajectories describe the envelope of variability expected by one-dimensional mixing.

The water column heat content H

$$\begin{aligned} H(z_m) &= \rho_o c_p \int_{z_m}^{0} \theta(z')dz' \\ &= -\rho_o c_p z_m\ \bar{\theta}(z_m) \\ &= -\rho_o c_p z_m\ \Delta\mathbf{\Theta}(z_m) - \rho_o c_p z_m\ \theta^*(z_m) \\ &= \mathbf{H}(z_m) + H^*(z_m) \end{aligned}$$

(where ρ_o is a reference density and c_p the specific heat of water at constant pressure) can then be partitioned into two terms, $\mathbf{H}$ and H^*. The "available heat storage" $\mathbf{H}(z_m)$ is the heat loss necessary to generate a mixed layer of depth $-z_m$, and describes the stability of the water column against convection; $\mathbf{H}(z_m)$ is proportional to the familiar buoyancy storage if α and β are constant. The residual or "unavailable" heat storage $H^*(z_m)$ reflects heat storage bound up in the temperature of the convective product of a certain depth (analagous to "spiciness"); it cannot be extracted from the ocean through local convection.

The mixed layer properties (θ^*, S^*) as well as the available and unavailable heat storage terms $\mathbf{H}$ and H^* depend upon the surface forcing through γ

$$\gamma = \frac{\Delta\mathbf{S}}{\Delta\Theta} = \rho c_p S^* \frac{P - E}{Q_T}$$

where Q_T is the net heat flux (positive upwards), E is the evaporation rate, and P is the precipitation rate. If $E - P > 0$ this can be rewritten as

$$\gamma = \frac{\Delta\mathbf{S}}{\Delta\Theta} = -\frac{c_p}{L_v} S^* \frac{\tilde{Q}_L}{Q_T}$$

where $\tilde{Q}_L$ is the latent heat flux due to the excess of evaporation over precipitation and L_v is the latent heat of vaporization; latent and sensible heat loss have been assumed to dominate the surface heat flux, a fair approximation in the wintertime Labrador Sea. Since S^* varies only a few percent over the interior during convection, a representative surface salinity can be substituted on the right hand side. A constant ratio of $\tilde{Q}_L$ to Q_T then implies a constant ratio of $\Delta\mathbf{S}$ to $\Delta\Theta$.

The ratio $\gamma = \Delta\mathbf{S}/\Delta\Theta$ defines the slope of a line in the θ/S space along which surface fluxes are attempting to move the properties of the mixed layer; the actual trajectory on the θ/S plane followed by the evolving mixed layer is a result of the competition between the surface fluxes and the entrainment of denser water as the mixed layer deepens. The dependence of the mixed layer properties on γ turns out to be weak for depths greater than a few hundred meters, however, due to the overwhelming influence of mixing with denser water as the mixed layer deepens.

Ship-based observations from a wintertime cruise in the Labrador Sea (Bumke, Karger & Uhlig 2002, Bumke, Uhlig, Berndt & Clemens 2001) can be used to estimate the ratio γ. Average values during the cruise at the ship location were: $Q_S = 200$ W m^{-2}, $E - P = 2.4$ mm day^{-1}, and $E = 5.5$ mm day^{-1}. From these we find the average latent heat loss $Q_L = 160$ W m^{-2}, latent plus sensible heat loss $Q_T = 360$ W m^{-2}, and heat loss due to excess evaporation $\tilde{Q}_L = 70$ W m^{-2}. Using $c_p/L_v = 1.6e^{-3}$°C^{-1} and $S_o = 35$ psu, one finds $\gamma \sim -0.01$ psu (°C)$^{-1}$.

Appendix C. Estimating strengths and sizes of advected eddies

A set of measures used to characterize coherent eddies in mooring data will now be defined. The actual peak azimuthal velocity at any depth is V, the half-width or "apparent" radius is X, and the eddy is moving with a speed U in (mathematical) direction Θ. One would like to form estimates of these quantities, denoted $\tilde{V}$, $\tilde{X}$, and $\tilde{U}$, $\tilde{\Theta}$.

Estimation of the eddy azimuthal velocity V requires a separation of the flow into a "mean" component and an eddy component. Owing to the nonstationarity of the mean flow and the departure of the eddy forms from the idealized model, determining the correct mean flow vector is difficult. It is much more straightforward to determine the apparent average direction for the mean flow, and then to recognize that the flow component perpendicular to this direction is almost entirely due to the eddy. Therefore our estimator $\tilde{V}$ will actually estimate not V itself but VXR^{-1}, the component of the eddy flow perpendicular to the advection direction. We choose the resulting bias towards low values over the additional errors which would arise from estimating the eddy speed by subtracting an estimated mean flow.

The edges of an eddy's velocity core are expected to be a local maximum of the velocity difference between two points. Given initial guesses (supplied by the wavelet analysis) for the eddy's center t_o and half-duration ΔT, refined values are found which maximize

$$\tilde{V} \equiv \frac{1}{2}|\xi(t_o + \Delta T) - \xi(t_o - \Delta T)|$$

over a time window encompassing each eddy, where ξ is the complex velocity $u + iv$. Since the parallel velocity u_p is even, $\tilde{V}$ is expected to be largest in the direction perpendicular to the advecting flow and is an estimation of the eddy velocity magnitude. The direction (on the complex plane) of $\xi(t_o + \Delta T) - \xi(t_o - \Delta T)$ is expected to be perpendicular to the advecting flow. Maximizing this equation therefore leads to refined estimates of the eddy's temporal center t_o and duration ΔT, as well as an estimate $\tilde{V}$ of the eddy's velocity magnitude and an estimate $\hat{\Theta}$ (± 180 °) of the advecting flow's direction.

If the eddies are weak relative to the advecting flow, and if the advecting flow varies slowly relative to the eddy's duration, then the advecting flow can be recovered simply by filtering the

time series. This estimate $\tilde{U}_f e^{i\tilde{\Theta}_f}$ is defined as the low-passed filtered velocity times series $u+iv$ at the eddy center t_o. The filter must be chosen to remove fluctuations on the time scale of the eddy, so here a Hanning window whose width is three times the width of the eddy core is used. This estimate is formed at the instrument level corresponding to the depth of the eddy's maximum currents.

A second way to estimate the advection velocity $Ue^{i\Theta}$ is to compare the observed currents with the observed shear. For an eddy whose velocity and density fields are azimuthally symmetric, the geostrophic vertical shear must be everywhere parallel to the total eddy currents. However, if the eddy is advected by a background flow $Ue^{i\Theta}$ that is independent of depth, the total currents will not be parallel to the shear, since the eddy currents are offset by the advecting flow $Ue^{i\Theta}$ but the shear is not. Therefore the advecting flow can be estimated by finding the depth-independent offset that makes the observed shear and observed total currents parallel to each other. The estimate $\tilde{U}_a e^{i\tilde{\Theta}_a}$ minimizes the angle difference

$$\Delta\Theta = |\arg\{\xi_{z_{max}} - \tilde{U}_a e^{i\tilde{\Theta}_a}\} - \arg\{\xi_{z_{max}} - \xi_{z_{min}}\}|$$

between the estimated eddy currents at z_{max} and the observed shear between z_{max} and z_{min} over a time window encompassing the eddy, chosen to be $(t_o - 2\Delta T, t_o + 2\Delta T)$. Here z_{max} is the depth at which the eddy currents are largest in magnitude and z_{min} is the depth at which the eddy currents are smallest in magnitude.

The advection speed can also be estimated indirectly through the momentum equation. In steady-state for an azimuthally symmetric pressure field $p = p(r, z)$, the radial momentum equation for inviscid flow is

$$f\tilde{v} + \frac{\tilde{v}^2}{r} = \frac{1}{\rho_o}\frac{\partial p}{\partial r}$$

where $\tilde{v}$ is the azimuthal velocity, r is the radial direction, ρ_o is a constant reference density, and the radial and vertical velocities are assumed to be zero. Because of azimuthal symmetry, the equation for the component of the radial momentum in the positive x direction along a chord (constant y) can be written as

$$fv\frac{r}{x} + \frac{v^2}{x}\frac{r}{x} = \frac{1}{\rho_o}\frac{dp}{dx}\frac{r}{x},$$

or equivalently

$$fv + \frac{v^2}{x} = \frac{1}{\rho_o}\frac{dp}{dx}, \tag{C.43}$$

since $\tilde{v} = vrx^{-1}$ and $\partial p/\partial r = dp/dx\ rx^{-1}$, where v is the velocity component in the y-direction and considering $p = p(r(x, y), z)$.

Equation $(C.43)$ describes the balance along a slice through an eddy located at the origin. If the eddy is in steady state balance but is advected past a fixed point by a constant advecting flow, then the same balance would be observed at the point. Substituting $-U(t - t_o)$ for x into (C.43) where U is a constant (eastward) advecting flow, and considering $p = p(x, y, t, z)$ since the eddy's location varies in time, yields

$$fU = -\frac{1}{v\rho_o}\frac{dp}{dt} + \frac{v}{t - t_o} \tag{C.44}$$

from which U can be determined given measurements of p and v. If the density field ρ' is sufficiently resolved in the vertical then dp/dt can be reconstructed through the hydrostatic relation $\partial p/\partial z = -\rho' g$.

The advected flow can therefore be found by assuming a cyclogeostrophic balance between the velocity observations and the density observations, and solving for the two terms on the right hand side of (C.44); this estimate of the advecting flow is denoted $\tilde{U}_w$. Note that in forming this estimate the orientation of the advecting flow must already be known, so the estimate $\tilde{\Theta}$ found in determining $\tilde{V}$ is used.

These three estimates of the advection flow lead to three corresponding estimates of the eddy size ($\tilde{L}_f$, $\tilde{L}_s$, and $\tilde{L}_a$) since $U\Delta T = L$. It should be emphasized that the apparent eddy size as observed from the mooring will tend to be smaller than the actual radius, since the eddies will generally be sliced off-center. However, since it is difficult to know the location of the eddy slice, it is not reasonable to expect that the eddy's true radius can be inferred from the apparent size. It should be pointed out that these estimates are necessarily rough. Therefore it would be preferable to average over a large number of eddies.

During 1994–1995, eddies observed at the Bravo mooring were advected by a strong background flow. The filtering and the equivalent barotropic method yielded virtually identical results; the average plus or minus one-half the difference of these estimates is given in Table 2. However, since the eddy duration was short relative to tidal noise and since the density signals were weak relative to instrument noise, the thermal wind method did not yield satisfactory results.

During 1998–1999 at the Bravo mooring, the eddies were very long in duration and had large density signals, so solving for the advecting flow in the thermal wind method provided a good match between the density and shear terms. A measure of the robustness of this method can be found by solving for a constant U (by minimizing the RMS error) over three different time windows: $[-\Delta T, \Delta T]$, $[-\Delta T, 0]$, and $[0, \Delta T]$. The mean plus or minus the standard deviation of these three estimates is reported in Table 2. However, since the other two methods both rely on a direct separation of the eddy and advecting currents, both failed during 1998–1999 when the eddy currents were much larger than the advection speeds.

During all other years, the combination of small advection speeds and coarse instrument spacing in the vertical made estimation of the size impossible.

Appendix D. Expressions for eddy property estimators

The estimator functions for eddy properties presented in Section 5.4 may be computed numerically beginning with the wavelet "response functions" (5.26,5.27). However, it may be useful to obtain analytic expressions for some of the probability density functions (pdfs) involved. Expressions for the pdfs of slice location X, observed anomaly strength δ_*, and observed apparent radius R_* were given in Section 5.5 of Lilly (2002) but unfortunately contained some errors. Equation (5.15), (5.17), and (5.18) from that text should read

$$f_X(X/R_o) = \frac{R_o}{R_c} B\left(\frac{X}{R_o}\frac{R_o}{R_c}\right) = \frac{R_o}{R_c} B\left(\frac{X}{R_c}\right) \tag{D.45}$$

$$f_\delta(\delta_*/\delta_o) = \frac{R_o}{R_c}\frac{1}{\left|d'_\delta\left(D_\delta(\delta_*/\delta_o)\right)\right|} B\left(\frac{\delta_*/\delta_o - \delta_c/\delta_o}{1-\delta_c/\delta_o}\right) \tag{D.46}$$

$$f_R(R_*/R_o) = \begin{cases} \Delta\left(\frac{R_*}{R_o}-1\right) & R_c < R_o \\ \Delta\left(\frac{R_*}{R_o}-1\right)\frac{R_o}{R_c} + \frac{1}{m}\frac{1}{R_c} B\left(\frac{R_*/R_o-(m+b)}{mR_c/R_o-m}\right) & R_c > R_o \end{cases} \tag{D.47}$$

where

$$B(x) \equiv \begin{cases} 0 & x < 0 \\ 1 & 1 \geq x \geq 0 \\ 0 & x > 1 \end{cases} \tag{D.48}$$

is known as the "boxcar" or "top-hat" function, and it has been assumed that δ_o is positive. The pdf for slice location X (D.45) is uniformly distributed between zero and the cutoff radius R_c. The pdf for observed anomaly strength δ_* (D.46) is obtained by the usual "chain rule" for pdfs, and is proportional to the inverse of the sea surface height slope magnitude for $\delta_o \geq \delta_* \geq \delta_c$ and zero otherwise. Finally the pdf for R_* (D.47) with $R_c > R_o$ consists of a boxcar with a delta-function on its left-hand edge, corresponding to the sloping and constant portions of the wavelet response function (5.28), respectively. The B function in (D.47) sets this term to zero outside the range $mR_c/R_o + b > R_*/R_o > m + b$ which is equivalent through (5.28) to $R_c > X > R_o$. It may be easily verified that all thes integrate to unity as required; the integral of (D.46) is simple after making a substitution for the differential $d(\delta_*/\delta_o) = d'_\delta(X/R_o)dX/R_o$, cancelling the similar term in the denominator on the right-hand-side of (D.2). The expected value of δ_*/δ_o may be similarly evaluated to be

$$\mathrm{E}\{\delta_*/\delta_o\} = \frac{R_o}{R_c}\int_0^{R_c/R_o} d_\delta(x)\,dx \tag{D.49}$$

which expresses taking the average value of $d_\delta(x)$ over the specified interval.

References

Arai, M. & Yamagata, T. (1994), 'Asymmetric evolution of eddies in rotating shallow water', *Chaos* **4**(2), 163–175.

Armi, L. & Zenk, W. (1984), 'Large lenses of highly saline Mediterranean water', *Journal of Physical Oceanography* **14**, 1560–1576.

Armi, L., Hebert, D., Oakey, N., Price, J. F., Richardson, P. & Rossby, H. (1989), 'Two years in the life of a Mediterranean salt lens', *Journal of Physical Oceanography* **19**, 354–370.

Bear, L. K., Pavlis, G. L. & Bokelmann, G. H. R. (1999), 'Multi-wavelet analysis of three-component seismic arrays: application to measure effective anisotropy at Piñon Flats, California', *Bulletin of the Seismological Society of America* **89**(3), 693–705.

Bumke, K., Karger, U. & Uhlig, K. (2002), 'Measurements of turbulent fluxes of momentum and sensible heat over the Labrador Sea', *Journal of Physical Oceanography* **32**(2), 401–410.

Bumke, K., Uhlig, K., Berndt, H. & Clemens, M. (2001), 'Measurements of snow fall over the Labrador Sea'. Unpublished.

Byrne, D. A., Gordon, A. L. & Haxby, W. F. (1995), 'Algulhas eddies: a synoptic view using Geosat ERM data', *Journal of Physical Oceanography* **25**, 902–917.

Cho, J. Y.-K. & Polvani, L. M. (1996), 'The emergence of jets and vortices in freely-evolving, shallow-water turbulence on a sphere', *Physics of Fluids* **8**(6), 1531–1552.

Clarke, R. A. & Gascard, J.-C. (1983), 'The formation of Labrador Sea water. Part I: Large-scale processes', *Journal of Physical Oceanography* **13**, 1764–1778.

Cresswell, G. (1982), 'The coalescence of two East Australian Current warm-core eddies', **215**(5), 161–164.

Cuny, J., Rhines, P. B., Niiler, P. P. & Bacon, S. (2002), 'Labrador Sea boundary currents and the fate of the Irminger Sea Water', *Journal of Physical Oceanography* **32**, 627–647.

Curry, R. G., McCartney, M. S. & Joyce, T. M. (1998), 'Oceanic transport of subpolar climate signals to mid-depth subtropical waters', *Nature* **391**, 575–577.

Cushman-Roisin, B. & Tang, B. (1990), 'Geostrophic turbulence and the emergence of eddies beyond the radius of deformation', *Journal of Physical Oceanography* **20**, 97–113.

D'Asaro, E. A., Walker, S. & Baker, E. (1994), 'Structure of two hydrothermal megaplumes', *Journal of Geophysical Research* **99**(C10), 20361–20373.

Dewar, W. K. (2002), 'Convection in small basins', *Journal of Physical Oceanography* **32**, 2766–2788.

Dewar, W. K. & Killworth, P. D. (1995), 'On the stability of oceanic rings', *Journal of Physical Oceanography* **25**, 1467–1487.

Dickson, R., Lazier, J., Meincke, J., Rhines, P. & Swift, J. (1996), 'Long-term coordinated changes in the convective activity of the North Atlantic', *Progress in Oceanography* **38**, 241–295.

Dickson, R., Meincke, J., Malmberg, S.-A. & Lee, A. J. (1988), 'The "Great Salinity Anomaly" in northern North Atlantic 1968–1982', *Progress in Oceanography* **20**, 103–151.

Eden, C. & Böning, C. (2002), 'Sources of eddy kinetic energy in the Labrador Sea', *Journal of Physical Oceanography* **32**(12), 3346–3363.

Elliott, B. & Sanford, T. (1986), 'The subthermocline lens D1. Part I: Description of water properties and velocity profiles', *Journal of Physical Oceanography* **16**(3), 532–548.

England, M. H. & Rahmstorf, S. (1999), 'Sensitivity of ventilation rates and radiocarbon uptake to subgrid-scale mixing in ocean models', *Journal of Physical Oceanography* **29**, 2802–2827.

Farge, M. (1992), 'Wavelet transforms and their application to turbulence', *Annual Review of Fluid Mechanics* **24**, 395–457.

Flierl, G. R., Larichev, V., McWilliams, J. C. & Reznik, G. (1980), 'The dynamics of baroclinic and barotropic solitary eddies', *Dynamics of Atmospheres and Oceans* **5**, 1–51.

Fu, L.-L. (2001), *Satellite altimetry and earth sciences*, Academic Press, San Diego.

Fu, L.-L., Christensen, E., Yamarone, C., Lefebvre, M., Ménard, Y., Dorrer, M. & Escudier, P. (1994), 'TOPEX/Poseidon mission overview', *Journal of Geophysical Research* **99**, 24369–24381.

Gascard, J.-C. (1978), 'Mediterranean deep water formation, baroclinic instability, and oceanic eddies', *Oceanol. Acta.* **1**(3), 315–330.

Gascard, J.-C. & Clarke, R. A. (1983), 'The formation of Labrador Sea water. Part II: Mesoscale and smaller-scale processes', *Journal of Physical Oceanography* **13**, 1779–1797.

Gonella, J. (1972), 'A rotary-component method for analyzing meteorological and oceanographic vector time series', *Deep-Sea Research* **19**, 833–846.

Haidvogel, D., Wilkin, L. & Young, R. (1991), 'A semi-spectral primitive equation ocean circulation model using vertical sigma and orthogonal curvilinear horizontal coordinates', *Journal of Computational Physics* **94**, 151–185.

Häkkinen, S. (1999), 'A simulation of the effects of a Great Salinity Anomaly', *Journal of Climate* **12**, 1781–1795.

Häkkinen, S. (2000), 'Decadal air-sea interaction in the North Atlantic based on observations and modeling results', *Journal of Climate* **13**, 1195–1219.

Hallberg, R. & Rhines, P. (1996), 'Buoyancy-driven circulation in an ocean basin with isopycnals intersecting the sloping boundary', *Journal of Physical Oceanography* **26**(6), 913–940.

Harcourt, R. R. (1999), Numerical simulation of deep convection and the response of drifters in the Labrador Sea, PhD thesis, University of California.

Hebert, D., Oakey, N. & Ruddick, B. (1990), 'Evolution of a Mediterranean salt lens: scalar properties', *Journal of Physical Oceanography* **20**, 1468–1483.

Hillaire-Marcel, C., de Vernal, A., Bilodeau, G. & Weaver, A. J. (2001), 'Absence of deep-water formation in the Labrador Sea during the last interglacial period', *Nature* **410**, 1073–1077.

Jones, H. & Marshall, J. (1993), 'Convection with rotation in a neutral ocean: a study of open-ocean deep convection', *Journal of Physical Oceanography* **23**, 1009–1039.

Jones, H. & Marshall, J. (1997), 'Restratification after deep convection', *Journal of Physical Oceanography* **27**, 2276–2287.

Keigwin, L. D., Jones, G., Lehman, S. J. & Boyle, E. (1991), 'Deglacial meltwater discharge, North Atlantic deep circulation, and abrupt climate change', *Journal of Geophysical Research* **96**(C9), 16811–16826.

Kelly, K. A., Beardsley, R. C., Limeburner, R., Brink, K. H., Paduan, J. D. & Chereskin, T. K. (1998), 'Variability of the near-surface eddy kinetic energy in the California Current based on altimetric, drifter, and moored current data', *Journal of Geophysical Research* **103**(C6), 13067–13083.

Khatiwala, S., Schlosser, P. & Visbeck, M. (2002), 'Rates and mechanisms of water mass transformation in the Labrador Sea as inferred from tracer observations', *Journal of Physical Oceanography* **32**(2), 666–686.

Koblinsky, C., Ray, R., Beckley, B. D., Tsaoussi, A. B. L. & Wang, Y.-M. (1999*a*), NASA ocean altimeter pathfinder project report 2: Data set validation, Technical report, Goddard Space Flight Center.

Koblinsky, C., Ray, R., Beckley, B. D., Wang, Y.-M., Tsaoussi, L., Brenner, A. & Williamson, R. (1999*b*), NASA ocean altimeter pathfinder project report 1: Data processing handbook, Technical report, Goddard Space Flight Center.

Labrador Sea Group (1998), 'The Labrador Sea Deep Convection Experiment', *Bull. Amer. Meteor. Soc.* **79**, 2033–2058.

LaCasce, J. H. (1998), 'A geostrophic vortex over a slope', *Journal of Physical Oceanography* **28**, 2362–2381.

Lam, J. S.-L. & Dritschel, D. (2001), 'On the beta-drift of an intially circular vortex patch', *Journal of Fluid Mechanics* **436**, 107–129.

Larichev, V. & Reznik, G. (1976), 'Strongly nonlinear, two-dimensional isolated Rossby waves', *Oceanology* **16**, 547–550.

Lavender, K. L., Davis, R. E. & Owens, W. B. (2000), 'Mid-depth recirculation observed in the interior Labrador and Irminger seas by direct velocity measurements', *Nature* **407**, 66–69.

Lavender, K. L., Davis, R. E. & Owens, W. B. (2002), 'Observations of open-ocean deep convection in the Labrador Sea from subsurface floats', *Journal of Physical Oceanography.*

Lazier, J., Hendry, R., Clarke, A., Yashayaev, I. & Rhines, P. (2002), 'Convection and restratification in the Labrador Sea, 1990–2000', *Deep-Sea Research* **49**, 1819–1835.

Lazier, J. R. N. (1980), 'Oceanographic conditions at Ocean Weather Ship Bravo, 1964–1974', *Atmosphere-Ocean* **18**(3), 227–238.

Legg, S. & Marshall, J. (1993), 'A heton model of the spreading phase of open-ocean deep convection', *Journal of Physical Oceanography* **23**, 1040–1056.

Legg, S. & McWilliams, J. (2001), 'Convective modifications of a geostrophic eddy field', *Journal of Physical Oceanography* **31**, 874–891.

Legg, S., McWilliams, J. & Gao, J. (1998), 'Localization of deep ocean convection by a mesoscale eddy', *Journal of Physical Oceanography* **28**, 944–970.

Lehman, S. J. & Keigwin, L. D. (1992), 'Sudden changes in the North Atlantic circulation during the last deglaciation', *Nature* **356**, 757–762.

Lilly, J. M. (2002), Observations of the Labrador Sea eddy field, PhD thesis, University of Washington.

Lilly, J. M. & Park, J. (1995), 'Multiwavelet spectral and polarization analysis', *Geophysical Journal International* **122**, 1001–1021.

Lilly, J. M. & Rhines, P. B. (2002), 'Coherent eddies in the Labrador Sea observed from a mooring', *Journal of Physical Oceanography* **32**(2), 585–598.

Lilly, J. M., Rhines, P. B., Visbeck, M., Davis, R., Lazier, J. R., Schott, F. & Farmer, D. (1999), 'Observing deep convection in the Labrador Sea during winter 1994–1995', *Journal of Physical Oceanography* **29**, 2065–2098.

Liu, P. C. & Miller, G. S. (1996), 'Wavelet transforms and ocean current data analysis', *Journal Atmospheric and Oceanic Technology* **13**, 1090–1099.

Mallat, S. (1999), *A wavelet tour of signal processing*, Academic Press, San Diego.

Marshall, J. & Schott, F. (1999), 'Open-ocean convection: observations, theory and models', *Reviews of Geophysics* **37**(1), 1–64.

Martin, S. (2003), *Ocean remote sensing*, Cambridge University Press. In press.

Matsuura, T. & Yamagata, T. (1982), 'On the evolution of nonlinear plantary eddies larger than the radius of deformation', *Journal of Physical Oceanography* **12**, 440–456.

Maxworthy, T. & Narimousa, S. (1994), 'Unsteady, turbulent convection into a homogeneous, rotating fluid, with oceanographic applications', *Journal of Physical Oceanography* **24**, 865–887.

McDowell, S. & Rossby, H. (1978), 'Mediterranean water: An intense mesoscale eddy off the Bahamas', *Science* **202**, 1085–1087.

McWilliams, J. C. (1984), 'The emergence of isolated coherent vortices in turbulent flow', *Journal of Fluid Mechanics* **146**, 21–43.

McWilliams, J. C. (1985), 'Submesoscale coherent vortices in the ocean', *Review of Geophysics* **23**(2), 165–182.

Mooers, C. N. K. (1973), 'A technique for the cross spectrum analysis of pairs of complex-valued time series, with emphasis on properties of polarized components and rotational invariants', *Deep-Sea Research* **20**, 1129–1141.

Nilsson, C. & Cresswell, G. (1981), 'The formation and evolution of East Australian Current warm core eddies', *Progress in Oceanography* **9**(3), 133–183.

Nof, D. (1981), 'On the beta-induced movement of isolated baroclinic eddies', *Journal of Physical Oceanography* **11**, 1662–1672.

Nof, D. & Dewar, W. (1994), 'Alignment of lenses: Laboratory and numerical experiments', *Deep-Sea Research* **92**(41), 1207–1229.

Park, J. & Mann, M. E. (2000), 'Interannual temperature events and shifts in global temperature: A "multiwavelet" correlation approach', *Earth Interactions*. Online paper.

Park, J., Lindberg, C. R. & Vernon, III, F. L. (1987), 'Multitaper spectral analysis of high-frequency seismograms', *Journal of Geophysical Research* **92**(B12), 12675–12684.

Percival, D. B. & Walden, A. T. (1993), *Spectral Analysis for Physical Applications*, Cambridge University Press, New York.

Pickart, R. S., Torres, D. J. & Clarke, R. A. (2002), 'Hydrography of the Labrador Sea during active convection', *Journal of Physical Oceanography* **32**(2), 428–457.

Pingree, R. & LeCann, B. (1993), 'Structure of a Meddy (Bobby 92) southeast of the Azores', *Deep-Sea Research* **40**(10), 2077–2103.

Prater, M. D. (2002), 'Eddies in the Labrador Sea as observed by profiling RAFOS floats and remote sensing', *Journal of Physical Oceanography* **32**(2), 411–427.

Prater, M. D. & Sanford, T. (1994), 'A Meddy off Cape Vincent, I: Description', *Journal of Physical Oceanography* **24**, 1572–1586.

Radko, T. & Stern, M. E. (2000), 'Self-propagating eddies on the stratified f-plane', *Journal of Physical Oceanography* **30**, 3134–3144.

Rahmstorf, S. (1996), 'On the freshwater forcing and transport of the Atlantic theromhaline circulation', *Clim. Dyn.* **12**, 799–811.

Rahmstorf, S. & Ganopolski, A. (1999), 'Long-term global warming scenarios computed with an efficient coupled climate model', *Clim. Change* **43**, 353–367.

Renfrew, I., Moore, K., Guest, P. & Bumke, K. (2002), 'A comparison of surface layer and surface turbulent flux observations over the Labrador Sea with ECMWF analyses and NCEP reanalyses', *Journal of Physical Oceanography* **32**(2), 383–400.

Rhines, P. B. (1977), The dynamics of unsteady currents, *in* E. Goldberg, ed., 'The Sea: ideas and observations on progress in the study of the seas', John Wiley and Sons, Inc., New York, pp. 189–318.

Rhines, P. B. (1979), 'Geostrophic turbulence', *Annual Review of Fluid Mechanics* **11**, 404–441.

Rhines, P. B. (1998), Circulation, convection, and mixing in rotating stratified basins with sloping topography, *in* J. Imberger, ed., 'Physical processes in lakes and oceans', American Geophysical Union, pp. 435–451.

Richardson, P., Walsh, D., Armi, L., Schröder, M. & Price, J. F. (1989), 'Tracking three Meddies with SOFAR floats', *Journal of Physical Oceanography* **19**, 371–383.

Riser, S. C., Owens, W. B., Rossby, H. T. & Ebbesmeyer, C. C. (1986), 'The structure, dynamics, and origin of a small-scale lens of water in the western North Atlantic thermocline', *Journal of Physical Oceanography* **16**, 572–590.

Ruddick, B. (1992), 'Intrusive mixing in a Mediterranean salt lens— intrusion slopes and dynamical mechanisms', *Journal of Physical Oceanography* **22**, 1274–1285.

Sarnthein, M., Winn, K., Jung, S. J. A., Deplessy, J.-C., Labeyrie, L., Erlenkeuser, H. & Ganssen, G. (1994), 'Changes in east Atlantic deepwater circulation over the last 30,000 years: eight time-slice reconstructions', *Paleoceanography* **9**(2), 209–267.

Schauer, U. (1989), 'A deep saline cyclonic eddy in the West European Basin', *Deep-Sea Research* **36**(10), 1549–1565.

Send, U. & Käse, R. H. (1998), Parameterization of processes in deep convection regimes, *in* E.Chassignet & J. Verron, eds, 'Ocean Modelling and Parameterization', Kluwer Academic Publishers, Dordrecht, pp. 191–214.

Send, U. & Marshall, J. (1995), 'Integral effects of deep convection', *Journal of Physical Oceanography* **25**, 855–872.

Slepian, D. (1978), 'Prolate spheriodal wave functions, Fourier analysis, and uncertainty– V: The discrete case', *Bell System Technical Journal* **57**(5), 1371–1430.

Smith, R. B. (1993), 'A hurricane beta-drift law', *Journal of the Atmospheric Sciences* **50**, 3123–3215.

Stammer, D. & Böning, C. W. (1992), 'Mesoscale variability in the Atlantic Ocean from Geosat altimetry and WOCE high-resolution numerical modeling', *Journal of Physical Oceanography* **22**, 732–752.

Stammer, D. & Wunsch, C. (1999), 'Temporal changes in eddy energy of the oceans', *Deep-Sea Research* **46**, 77–108.

Stammer, D., Hinrichsen, H.-H. & Käse, R. H. (1991), 'Can Meddies be detected by satellite altimetry?', *Journal of Geophysical Research* **96**(C4), 7005–7014.

Steffen, E. & D'Asaro, E. A. (2002), 'Deep convection in the Labrador Sea as observed by Lagrangian floats', *Journal of Physical Oceanography* **32**(2), 475–492.

Stephens, J. C. & Marshall, D. P. (1999), 'Dynamics of the Mediterranean salinity tongue', *Journal of Physical Oceanography* **29**, 1425–1441.

Straneo, F. & Kawase, M. (1999), 'Comparisons of localized convection due to localized forcing and preconditioning', *Journal of Physical Oceanography* **29**, 55–68.

Sutyrin, G. (2001), 'Effects of topography on the beta-drift of a baroclinic vortex', *Journal of Marine Research* **59**, 977–989.

Sutyrin, G. G., Hesthaven, J., Lynov, J. & Rasmussen, J. (1994), 'Dynamical properties of vortical structures on the beta-plane', *Journal of Fluid Mechanics* **268**, 103–131.

Talley, L. & McCartney, M. (1982), 'The distribution and circulation of Labrador Sea Water', *Journal of Physical Oceanography* **12**, 1189–1205.

Thomson, D. J. (1982), 'Spectral estimation and harmonic analysis', *Proceedings of the IEEE* **70**(9), 1055–1096.

White, M. A. & Heywood, K. J. (1995), 'Seasonal and interannual changes in the North Atlantic subpolar gyre from Geosat and TOPEX/Poseidon altimetry', *Journal of Geophysical Research* **100**(C12), 24931–24941.

Figure captions

Figure 1

Orientation map of the Labrador Sea and its surroundings. Major surface and deep currents are shown schematically. Also marked are are the locations of the Bravo mooring and of the AR7W World Ocean Circulation Experiment (WOCE) hydrographic line. This map was modified from one kindly provided by Samar Khatiwala.

Figure 2

Locations of moorings (circles), the AR7W WOCE section (triangles), and an additional parallel line from February 1997 (squares). The thick solid line is the coastline, and thin solid lines are the isobaths in 500 m intervals; the innermost isobath intersected by the AR7W line is for 3.5 km. The thick dashed line is a region defined as the "Labrador Sea interior", which is the 3 km isobath cut off at the southeast corner. Boundary currents tend to be trapped shoreward of the 3 km isobath. Distances are shown in terms of a Mercator expansion about a point near the center of the region mostly enclosed by the 3 km isobath. A small rectangle west of the Bravo mooring indicates the site of a ship-surveyed eddy to be discussed later.

Figure 3

Basic features of the annual and interannual variability in the Labrador Sea during the 1990's. The left-hand column contains monthly means while the right hand column contains June-to-June annual means for the same quantity. Y-axis limits for (e) and (f) are the same, as are those for (g) and (h); the y-axis ranges and y-tick mark intervals in (b) and (d) are smaller those in (a) and (c), respectively, with vertical black lines on the left hand plot marking the axis range for the corresponding right-hand plot.

Panels (a) and (b) are wind stress from the NCEP model reanalysis; units are cN($= 10^{-2}$N) m^{-2}. In (a) the thick black line is the monthly mean during 1992-2000, averaged over the "subpolar gyre" region defined in the text, with the gray envelope denoting plus or minus one standard deviation. In (b) the black line is the June-to-June annual mean over this same area, while the thick gray line is an average over the "Labrador Sea interior" defined in the text.

Panels (c) and (d) are the ocean heat gain from the NCEP model during 1992–2000. The thick black line and gray envelope in (c) are the monthly-mean surface heat gain plus or minus one standard deviation over the Labrador Sea interior region, and the dashed black line is an estimate of heat gain due to lateral fluxes during 1997 (see panel (g) and Section 2.4). In (d), the thick gray line is the June-to-June integrated surface heat gain from the NCEP model, the thin black line is the heat flux implied by differencing the heat content between the surface and 2000 m observed in springtime hydrographic sections, and the dashed line is the second of these lines minus the first. Note that no data point was available during 1991 for the ocean heat content, so the data points near January 1991 represent the average fluxes over the two-year period June 1990–June 1992.

Panels (e) and (f) show the annual cycle and interannual variability of the detided speed observed by the shallowest available instrument at each mooring (see Table 1). In (e) the symbols and lines show the mean value and standard deviations among sets of monthly-mean speed observations at the Bravo / K1 mooring (black circles) and other moorings (gray triangles); see text for details. Panel (f) shows the mean and standard deviation of the detided speed over each mooring

deployment for the Bravo mooring (filled circles), K1 mooring (open circles), and other moorings (gray triangles). Vertical lines are the standard deviations of speed and horizontal lines show the duration of each mooring record. In both (e) and (f) the location of the symbols and the vertical lines have been offset slightly in time for clarity. Some standard deviation bars extend off the top of the page in (f).

Panels (g) and (h) show Labrador Sea heat content variability. Monthly-mean values of the interior "convection region" (see text) heat content during 1997 are shown in (g). Here the thick gray line is the heat content observed by P-ALACE float profiles between the surface and 1300 m depth, as described in the text; the thick dashed black line is the observed heat content down to 200 m; and the thin black line is the integral of the NCEP surface heat gain (offset to be zero in March). The gray triangles and vertical lines are the means and standard deviations for the heat content between the surface and 1300 m depth from two hydrographic sections. The original value of the gray line during March has been subtracted from all other data. Panel (h) shows a partitioning of the interior Labrador Sea heat content between the surface and 2000 m as observed by the springtime hydrographic sections: the thin black line, thick gray solid line, and thick dashed black line are the total, available, and residual heat contents as defined in the text. Each line has been offset to be zero in 1990. Finally, the depth of convection (in kilometers), estimated as described in Appendix A, is shown by the squares. Note that there is no data point during 1991.

Figure 4

A nearly continuous five year record of potential temperature (a) and current speed (b) from the central Labrador Sea, near the site of the former OWS Bravo. Gray horizontal lines correspond to 3°C in (a) and zero current speed in (b). Additionally the location of each gray line on the right-hand axis marks the depth of the corresponding instrument in the absence of currents. This record combines the UW/BIO Bravo mooring (years 1994–1995, 1995–1996, and 1998–1999 shown) with the IFM Kiel K1 mooring (years 1996–1997 and 1997–1998 shown). The two moorings are located about 20 km apart, the Bravo mooring at 56°45' N, 52°27' W and the K1 mooring at 56°34' N, 52°40' W. Note the increase in speed in recent years.

Figure 5

With panel (a) showing the average monthly-mean heat loss for reference, the remaining panels show the potential temperature during 1994–1995 (b), 1996–1997 (c), and 1998–1999 (d) at the depths marked with crosses. Shading differs for each panel as shown, but the black contour is always 2.8°C and the white contours are always 3.2, 3.6, and 4.0°C.

Figure 6

Potential temperature during February 1997 along the northern line shown in Fig 2. The contour interval is 1°C for labeled contours and 0.2°C for unlabeled contours. The gray line with triangles marks the mixed layer depth (estimated as the shallowest depth at which the 20-meter smoothed potential density exceeds the average of the top 20 m by at least 0.01 kg m^{-3}). Note the extension of warm temperatures into the Labrador Sea from the Greenland side in the upper ~700 m.

Figure 7

The average springtime salinity (a) and potential temperature (b) of the Labrador Sea interior during the 1990's, formed by averaging within realizations of the AR7W hydrographic line as

described in the text. The estimated depth of convection (See Appendix A) is also shown, with the circle at, say, 1995 indicating the depth of convection during the winter encompassing January 1 1995. In panel (a) the contour interval is 0.01 psu with contours for values 34.82 psu and less being white. For (b), the contour interval is 0.1, with values 3.4°C and greater being white.

Figure 8

The hydrographic structure of the Labrador Sea interior from springtime CTD sections: potential density anomaly referenced to 1000 m σ_{1000} kg m^{-3} (a), potential temperature (b), salinity (c), and the first baroclinic normal mode of the horizontal velocity (d), normalized to unit energy (for the 50 m decimated data used in the computation). In all panels, the thick black line refers to 1994 and the thick gray line to 1999.

Figure 9

Monthly-mean P-ALACE profiles of potential temperature in the convection region (see text) for the four months February (thin black line), March (thick gray line), April (thin dashed line) and May (thick gray dashed line).

Figure 10

An illustration of the heat storage partitioning discussed in Appendix B. An initial water column having a potential temperature profile shown by the thin solid line is numerically "convected", leading to a trajectory of mixed layer temperatures indicated by the thick dashed line. For instance, when the mixed layer is one kilometer deep, its temperature is about 2.8 °C (the border between the black and gray areas). The amount of heat required to convect to a given depth z is simply proportional to the area between the original profile and the profile of the mixed water column, assumed vertically homogeneous above z and unchanged below z, and is referred to as the "available" heat $\mathbf{H}(z)$; for $z = 1$ km, the available heat is the darkly shaded area in the figure. The area between the mixed layer temperature at z and a reference temperature (here two degrees) down to a depth a z is termed the residual heat content $H^*(z)$, and is shown for $z = 1$ km as the lightly shaded area.

Figure 11

Comparison of a Rankine vortex (see Section 3.3.1) sliced along a line midway between its center and its rim (a), with a 2π wavelet (b) having $m = 2/3$. In (a) the thin black (thick gray) line is the velocity component parallel (normal) to the advecting flow. Vertical dashed lines in this and the following panel mark the edges of the eddy core. In (b) the thin black (thick gray) line is the real (imaginary) part of the wavelet, the thick dashed line is the wavelet modulus, and the thick dashed line is the envelope function h.

Figure 12

Currents due to an east-west section through a Rankine vortex (a) and the resulting cosine $\mathcal{A}_c$ (b), sine $\mathcal{A}_s$ (c), and total $\mathcal{T}$ (d) wavelet transforms. The eddy has $V = 10$ cm s^{-1} and $R = 10$ km and is sliced along a straight line passing midway between the center and the rim. The eddy edges are marked with dashed vertical lines. In (a), the speed is a thin black line, the eastward velocity component u is a thick gray line, and the northward velocity component v is a thick dashed black line. In b–d, the contour interval is 0.25 cm s^{-1} for the gray lines and 1 cm s^{-1} for the black lines (each beginning with zero).

Figure 13

Current speed (a) observed during June–August 1994 at the 1010 m (solid line) and 3476 m (dashed line), together with the cosine $\mathcal{A}_c$ (b), sine $\mathcal{A}_s$ (c), and total $\mathcal{T}$ (d) wavelet transforms of the 1010 m data. Dashed vertical lines in (a) mark the edges of eddies identified in LR. In b–d, the contour interval is 0.25 cm s^{-1} for the gray lines and 1 cm s^{-1} for the black lines (each beginning with zero). Additional information in (d) is introduced in Section 3.3.4. Thin gray lines are modulus maxima lines and dashed white-gray lines are those maxima lines containing significant velocity anomalies. Black circles are the locations (τ, a) of the velocity anomalies passing the eddy-finder criterion, and black triangles mark the temporal location and duration of the eddies as determined in LR.

Figure 14

Currents observed during a five-year period at the Bravo / K1 mooring location. Stickvectors are shown in (a,b) and speed in (c,d). Years 1996–1997 and 1997–1998 are from the K1 mooring, with the other three years from the Bravo mooring. The depths of the measurements shown are 1260 m, 2500 m, 469 m, 209 m, and 100 m for each of the five years respectively, chosen to correspond to the maximum currents of the observed eddies during each year. In (a–d) the currents have been detided using a 24-hour Hanning filter. Black bars at the top of (a,b) mark the months March–April, in which vertical homogenization of the water column due to deep convection is at its most extreme. Panels (e,f) show the square root (for display purposes) of the total wavelet transform $\mathcal{T}$. Small symbols mark the locations of events identified by the automated eddy finder (Section 3.3.4), with white circles being events that are judged to be eddies and black triangles being non-eddies.

Figure 15

Annual cycle (a) and interannual variability (b) of the magnitude of velocity anomalies identified by the wavelet method, sorted into eddy-like (open circles) and non-eddy-like (closed triangles) forms by comparison with idealized eddy models. Horizontal lines in (b) mark the amplitude cutoff χ_a used for each year, below which no apparent eddies were found to occur.

Figure 16

Thermal structure (a) and velocity structure (b) of an anticyclone (left) and a cyclone (right) from a numerical model. The contour intervals are the same as in Fig. 16a–b. In (b), black lines correspond to velocity out of the page and gray lines to velocity into the page.

Figure 17

Results of the eddy census for the Bravo / K1 mooring. Eddy-like events are color-coded by the mooring at which they were observed (black for the Bravo mooring, gray for the K1 mooring), and their categorization is reflected in the symbol shape (circles for convective lenses, triangles for Irminger rings, squares for other or unknown types). (a) Estimated magnitude $\tilde{V}$ of the normal velocity, with negative values here meaning anticyclonic rotation. (b) Depth of the maximum eddy currents, together with lines showing the depths and times at which velocity measurements were taken. (c) Potential temperature of each eddy at two depths, connected by a vertical line. The upper symbol of each pair is the eddy's temperature at the closest depth to 250 m but greater than 150 m, and the lower symbol is the minimum temperature inside the eddy above ~1250 m. For reference, horizontal lines show the mean values, from the springtime hydrographic sections, of the 250 m (dashed lines) and 1000 m (solid lines) potential

temperature; standard deviations are indicated by the pairs of dotted lines. These lines extend from the time the section was taken until the time of the next year's section. Note the absence of suitable temperature measurements during 1995–1996.

Figure 18

A comparison of the velocity structure of the "convective lens" (a) and "Irminger ring" (b) type eddies. Currents at both the leading and trailing eddy edges (see text for definition) are shown, with open circles representing depths of measurements. The current component v_n normal to the estimated advection direction is shown, with positive currents directed ninety degrees counterclockwise from the advection direction.

Figure 19

Thermal structure (a,c) and velocity structure (b,d) for a "convective lens" and an "Irminger ring", respectively. In all panels the x-axis is time in days from the estimated center of the eddy, and the y-axis is depth. In (a) thick contours are every 0.25°C and thin contours every 0.05°C; in (c) the contour interval is double that in (a). The "normal" velocity v_n is shown in (b,d). For an anticyclone such as these events one expects the initial signature of the eddy to be to the right of the advecting flow ($v_n < 0$). Black contours are for $v_n > 0$ and grey contours for $v_n < 0$, with the zero contour a heavy dashed black line. The thick contours in (b) are every 20 cm s^{-1} and the thin contours every 4 cm s^{-1} per second. In (d) the thick contours are every 25 cm s^{-1} and the thin contours every 5 cm s^{-1} per second. Approximate locations of instruments are marked by symbols on both the right- and left-hand edges of each panel; circles are for measurements of temperature, salinity, and pressure, and triangles for measurements of temperature and velocity. In all panels, fields have been contoured versus the time-varying instrument depths, estimated from measurements of pressure. The vertical motion of the mooring is the cause of the "wave" of white space at the top of (d) and a similar, barely discernable fluctuation in (b).

Figure 20

Thin black lines surrounded by gray envelopes are the mean potential density (a) potential temperature (b) and "available heat content" **H** (c), plus or minus one standard deviation, for the AR7W hydrographic line during June–July 1998 is shown. These profiles are computed from the "de-eddied" dataset described in Appendix A. The available heat content at a given depth is the surface heat loss necessary to create a mixed layer of that depth, given initial vertical profiles of potential temperature and salinity as well as a fixed ratio of latent to total heat loss; see Appendix B for more details. The thick black line in each panel is the corresponding field for an anomalous profile observed along the AR7W line in July 1998. In (a) and (b) potential density (referenced to 1000 m) and salinity profiles through Irminger ring type eddies observed by the mooring during 1998–1999 are given as thin black lines with circles marking instrument depths. The properties of the two mixed layers of the anomalous hydrographic profile are marked in each panel, and in (c) the horizontal gray line marks the estimated depth of convection the previous winter.

Figure 21

Station locations for the February–March 1997 hydrographic cruise; each symbol type denotes one of the seven different hydrographic lines.

Figure 22

Mixed layer potential temperature versus latitude (a) and versus mixed layer depth (b) for the February / March 1997 hydrographic cruise, after applying 0.5 GJ m^{-2} surface heat loss as described in the text. Different symbols indicate different hydrographic lines as shown in Fig. 21. Vertical lines mark the potential temperature of the two cores of the July 1998 eddy shown in Fig. 20. The best matches to the properties of this eddy are found along the "triangle" line between 59° N and 61.5° N.

Figure 23

An eddy observed during January of 1998 by the R/V Knorr. (a) Plan view. The x and y axes are as shown in the small rectangle in Fig. 2. Ship-intake sea surface temperature (SST) is contoured, linearly interpolated from the ship-tracks shown as dots. Small circles are locations of XBT casts, and a triangle marks the center of the eddy as estimated from the SST contours. The large white circle is the estimated eddy radius (15 km) as inferred from the mixed layer depth and temperature. (b) Average potential temperature from the surface to the base of the mixed layer, versus distance from the eddy center. (c) Mixed-layer thickness versus distance from the eddy center. See text for a definition of mixed-layer thickness.

Figure 24

V_{EKE} for the Labrador Sea during the seven-year period 1994–2000. The shading and contours are as given in the legend. TOPEX / Poseidon ground tracks are shown by dotted lines and the coastline is shown with a thick black line. V_{EKE} has been set to zero for depths shallower than 500 m due to concerns about altimeter performance in coastal regions. A region defined as the "Labrador Sea interior" is shown by the thick dashed line, and follows the 3000 m isobath except for where it cuts between two bathymetric ridges to form a closed loop. The three rectangular boxes define regions referred to as the northern, central, and southern regions respectively. The location of the Bravo / K1 moorings are indicated by the circles, and those of other moorings by triangles. The AR7W WOCE hydrographic section is shown by the thick black line. Latitude and longitude are shown on the right-hand and top axes edges, with distance (in units of 100 km) based on a Cartesian expansion about a point (58.5° N, 52° W) near the center of the Labrador Sea interior shown on the left and bottom edges.

Figure 25

The sea surface height anomaly (a) and crosstrack geostrophic currents (b) for a sample monopole solution (thin black lines) and sample dipolar solution (thick gray lines), when each eddy has been "sliced" along a line about which it is symmetric. Vertical dotted lines mark the edges of the monopole core at ±10 km and the dipole's "radius of discontinuity" at ±40 km.

Figure 26

The real (thin black line) and imaginary (thick gray line) of a time-concentrated wavelet with scale $a = 10$ km. Other parameter values are given in the text. Vertical lines mark the "radius" of the wavelet, given by the eddy scale $\pm a$. The dashed line traces out the modulus of the wavelet.

Figure 27

Illustration of the SSH anomaly definition. (a) Detrended sea surface height for one cycle during October 1999 along the descending track passing nearest the Bravo mooring. (b) The

modulus of the wavelet transform $|\mathcal{W}|$, with shading and contours as indicated in the legend. Symbols denote anticyclonic (upward triangles), cyclonic (downward triangle), and dipolar (circles) events having $|Z_*| > 0.1$ and $|\delta_*| > 5$ cm. Those events having $|\delta_*| > 10$ cm are shown with large symbols, and others with small symbols. Dashed boxes are the space-scale region over which each event has been required to be a local maximum by (5.21).

Figure 28

Histogram of all even (i.e., monopole-like) events within the Labrador Sea interior as a function of scale a_* and sea surface height anomaly $|\delta_*|$, for (a) the data and (b) a noise dataset as described in the text. Bins of both a_* and $|\delta_*|$ are of uniform width along the logarithmically scaled axes. Black triangles are estimated values for eddies as reported in Section 4. The thick black line is the contour at which events occur ten times as frequently in the data as in the noise dataset. Thin black lines mark the edges of the "eddy band" (see text for details).

Figure 29

Actual and wavelet-estimated sea surface height anomaly (a) and apparent radius (b) for eddies having the sample monopole form. In both plots the x-axis has been normalized by the eddy radius. The thin solid line is the eddy's peak sea surface height anomaly (a) and apparent radius (b) as a function of slice location. Symbols are the δ_* (a) and R_* (b) values obtained by applying the wavelet algorithm to a variety of unit-magnitude eddies sliced at a variety of locations. The thick dashed line in (b) is a least squares fit to the data. In both panels eddies having radii of 5, 10, 15, ... 30, 40, and 50 km have been sampled at slice locations of 0.25, 0.5, 0.75, 1, 1.5, 2.5, ... 9.5 km.

Figure 30

Estimators for δ_o and R_o based on the sample monopole form. Panel (a) shows the relationship between the expected value of samples $E\{\delta_*\}$ and the true eddy sea surface height anomaly δ_o, with both normalized by the cutoff value δ_c. The solid line is for the $\frac{1}{2}\lambda$ eddy, and the dashed and dash-dotted lines are for a 1.5 layer eddy with $R_o = \lambda$ and $R_o = \frac{1}{4}\lambda$ respectively. Panel (b) shows the ratio between the true radius R_o and the expected value of the observations $\mathrm{E}\{R_*\}$, as a function of $\mathrm{E}\{\delta_*\}/\delta_c$.

Figure 31

A sketch of the eddy-in-a-box model. Panel (a) shows a single eddy uniformly distributed over a 100×100 km box, with the dashed lines showing the locations of altimeter lines. In panel (b) a fixed eddy of radius 10 km and $R_c = 20$ km is observed by a randomly placed altimeter grid. The number of events observed during a single cycle depends upon where a crossover point of the altimeter grid happens to fall. Dashed vertical and horizontal lines mark out nine regions, with numbers indicating the number of events observed when the crossover point falls within each region.

Figure 32

Histogram of TOPEX / Poseidon eddy-band events ($|\delta_*| > 10$ cm, $|Z_*| > 0.1$) versus apparent radius R_* in the Labrador Sea interior region (a); the bin spacing is 5.7 km, corresponding to one altimeter data point. The vertical line marks the peak of the sum of these three curves at $R_* = 22.8$. Panel (b) is the cumulative histogram of interior events with $|Z_*| > 0.1$ versus magnitude $|\delta_*|$, summed from large magnitude; note the log-log axes. The vertical line marks the cutoff of the "eddy-band" events at $|\delta_*|$=10 cm. In both panels, positive even or anticyclone-

like events (thin solid line), negative even or cyclonic-like events (thick gray line), and odd or dipole-like events (dashed thick black line) are shown.

Figure 33

Comparison of the TOPEX eddy-event census and the mooring eddy census for the time period July 1998–July 1999. Panel (a) shows altimeter V_{EKE} along the ascending track passing nearest the mooring for the indicated time period. The dashed line marks the nearest approach of the track to the mooring, about 14 km distant. Symbols denote anticyclonic (upward triangles), cyclonic (downward triangle), and dipolar (circles) eddy-band events. Panel (b) is the speed at the uppermost instrument of the Bravo mooring, with horizontal bars marking the locations of confirmed eddy cores— all of which are anticyclones.

Figure 34

All events from eddy-band histogram peak at $R_* = 22.8$ km (four data points at 5.7 km spacing) from the central Labrador Sea. Anticyclonic events are shown in (a), cyclonic events in (b), and dipolar events in (c). Within each panel events have been aligned at their phase-adjusted centers as described in Section 5.3.3 and sorted according to magnitude $|\delta_*|$, with the largest-magnitude events at the bottom of the panel and successive events offset by 10 cm. Black lines are events having $|\delta_*| > 20$ cm and gray lines are events having $|\delta_*| < 20$ cm. For clarity, dipolar events have been flipped so that positive flank is always to the right of the center. Dashed vertical lines show $R_* = \pm 22.8$.

Figure 35

Composite anticyclonic, cyclonic, and dipolar events for all events in the Labrador Sea interior having $R_* = 22.8$ km and $\delta_* > 20$ cm, which are the black lines in Fig. 34. Panel (a) shows the average sea surface height anomaly profiles for the anticyclonic events (thin black line), cyclonic events (thick gray line), and dipolar events (dashed black line), and panel (b) shows the corresponding crosstrack velocity profiles assuming geostrophy. Vertical gray lines in both panels show the standard deviation at alongtrack locations spaced every 50 km, and dotted vertical lines show the estimated apparent radius R_*. For comparison, a sea surface height profile and associated currents for an anticyclonic eddy solution of the type used to calibrate the event census (see Fig. 25), with a radius of 22.8 km, are shown by the triangles.

Figure 36

The percentage of TOPEX cycles inside (a) all eddy event cores (divided by two for comparison with other panels), dipolar events (b), anticyclonic events (c), and cyclonic events (d) for the seven-year period 1994–2000. See text for details. Since there are about 37 T/P cycles per year, the maximum 20% event coverage corresponds to $20 \times 37/100 \times 7 \approx 50$ separate events. A square marks the location of the Bravo mooring; other lines are as in Fig. 24.

Figure 37

Each panel is the percentage of TOPEX cycles inside a subset of the eddy-band events, divided by the maximum occurring percentage for that subset. The left column contains "small" events ($R_* < 20$ km), the right column "large" events ($R_* > 20$ km). Rows are for different strength events, with panels (a) and (b) for 10 cm$< |\delta_*| <$15 cm, panels (c) and (d) for 15 cm$<$ $|\delta_*| <$20 cm, and panels (e) and (f) for $|\delta_*| >$20 cm. In all panels the shading and contours are identical, as given in the legend.

Figure 38

Latitude-time plots of the annual cycle of the TOPEX / Poseidon "eddy speed" V_{EKE} (a) and normalized eddy event count concentration $\mathcal{N}$ (b), averaged over the seven-year time period 1994–2000 and between $x = \pm 200$ km. In both panels the slanting line corresponds to a southward propagation speed of 4.7 cm s^{-1}, and the horizontal dotted line marks the latitude of the Bravo mooring. The contoured fields have semimonthly temporal spacing with overlapping one month-wide bins centered on the first and 15th of each month, and 25 km latitudinal spacing with overlapping 100 km wide bins centered at ... $-50, 0, 50$... km. Contours are spaced every 2 cm s^{-1} in (a) and every 10 units in (b), and are drawn at the values indicated on the colorbars.

Figure 39

Latitude-time plot of the interannual variability of the eddy speed V_{EKE} (a) and the event concentration $\mathcal{N}$ (b). Here averaging is performed over yearlong bins spaced every six months; all other parameters are as in Fig. 38, including axes limits and contour levels.

Figure 40

Variability of the estimated eddy population, computed as described in the text, with a cutoff of $\delta_c = 10$ cm. Panels (a,b) are for the northernmost box in Fig. 24, panels (c,d) are for the central region, and panels (e,f) are for the southern region. In each panel, anticyclonic events are denoted by upward triangles, cyclonic events by downward triangles, and dipolar events by squares. Panels (a,b,c) show the eddy populations for each type during a given month, while panels (d,e,f) show the estimated populations in one-year long period overlapping by six months. In the left column, a point at January denotes a time period from the first until the end of January; in the right column, a point at 1996 denotes a time period centered on January first 1996. The ninety percent confidence intervals are shown by the vertical lines, with only every third line shown for clarity.

Figure 41

As with Fig. 40 but choosing a cutoff of $\delta_c = 15$ cm; note the change in axis limits from Fig. 40.

Figure 42

As with Fig. 40 but choosing a cutoff of $\delta_c = 20$ cm; note the change in axis limits from Fig. 41.

Figure 43

A close-up of the eddy census from August 1999 through December 2000, for all anticyclonic events between $x = -200$ km and $x = 200$ km. Each circle represents one event, with the size of circle proportional to the magnitude of event's estimated sea surface height anomaly $|\delta_*|$. (a) Event time versus north-south location. The diagonal line corresponds to a southward velocity of $\sim$4.7 cm s^{-1}. (b) Event magnitude versus north-south location; this panel also acts as the key for converting circle size into a sea surface height. A combined location, magnitude, and time criterion has been used to identify certain events, shown as the filled black circles in each panel, which appear to reflect the southward propagation and decay of several individual eddies.

Figure 44

Plan view of the features shown in Fig. 43. Circles are the (x, y) locations for all anticyclonic events from August 1999 through December 2000, with the size of circle proportional to the magnitude of event's estimated sea surface height anomaly $|\delta_*|$. The rectangular box encompasses the locations of events shown in Fig. 43. Filled black circles inside the box are the same as those shown in Fig. 43.

Figure 45

A summary of wind stress and current variability. (a) The annual cycle of monthly-mean wind stress forcing from the NCEP model over the Labrador Sea (thick solid line) plus or minus one standard deviation (shaded envelope), together with the wind stress curl over the same region (thick dashed line). (b) Interannual variability of the wind stress (solid line) and wind stress curl (dashed line). In both (a) and (b) wind stress is measured in N m^{-2} and wind stress curl in 10^{-6} N m^{-2}.

Panels (c) and (d) show the altimeter V_{EKE} in four regions: the 20 altimeter points nearest the Bravo /K1 mooring (thin dashed line) and the three boxes indicated in Fig. 24, from north to south (thin solid line, thick gray line, and thick dashed line). The boxes are bounded by $x = \pm 200$ km, have a 2°latitudinal extent, and are centered at 61, 59, and 57° N respectively. The thin dashed lines are repeated in panels (e) and (f) below.

Panels (e) and (f), repeated from Fig. 3, show the annual cycle and interannual variability of the detided speed observed by the shallowest available instrument at each mooring (see Table 1). In (e) the symbols and lines show the mean value and standard deviations among sets of monthly-mean speed observations at the Bravo / K1 mooring (black circles) and other mooring (gray triangles). Panel (f) shows the mean detided speed and its standard deviation over each mooring deployment (shown by the horizontal lines) for the Bravo mooring (filled circles), K1 mooring (open circles), and other moorings (gray triangles). Dashed lines are the same as the dashed lines in panels (c) and (d). Vertical lines are the standard deviations of speed and horizontal lines show the duration of each mooring record. In both (e) and (f) the location of the symbols and the vertical lines have been offset slightly in time for clarity. Vertical bars mark the vertical axis limits for panels (c) and (d).

Table captions

Table 1

Mooring location is indicated along with nominal depths (in meters) of instrumentation. Record period is indicated by the date (in "year:day" format) at the beginning and end of the time series. ADCPs are acoustic Doppler current profilers, ACMs are acoustic current meters, RCMs are Aanderraa RCM-8 current meters, and Seacats are Seabird Seacat 16 temperature and conductivity sensors. All instruments measure temperature. "P" indicates a pressure sensor, and for ADCPs "U" denotes upward-looking and "D" downward-looking.

Table 2

Results of the eddy census for the Bravo mooring. "Time" is the time of the eddy center in "Year:Yearday:Hour" format. "ΔT" and "$\tilde{V}$" are the eddy duration in hours and estimated azimuthal velocity in centimeters per second, respectively, as defined in the text. "Rot" is the eddy rotation sense, "C" for cyclone and "A" for anticyclone. "Type" is an assesment of the eddy type, "I" for convective lenses, "II" for Irminger rings, and "U" for eddies of unknown or other type. Finally "$\tilde{L}$" is the estimated apparent radius as described in the text, in kilometers.

Table 3

As with Table 2 but for the K1 mooring. No size estimates were possible with the K1 mooring.

Table 1
(Table 1)

Interior Labrador Sea moorings 1994–1999

Name	Record period	Lat	Lon	ADCP	ACM	RCM	Seacat
Bravo	94:147 – 95:162	56:45.20	-52:27.30	300 U	——	110 P	260
						760	510
						1260	1010 P
						1760	1510
						2510	2010
						3476	2512
Bravo	95:165 – 96:142	56:45.15	-52:27.36	——	——	102 P	68
						2500	2610
						3468	
Bravo	96:298 – 97:144	56:44.62	-52:26.61	——	——	763	96 P
						1263	263 P
						2513	513 P
						3479	1013
							1513
							2013
Bravo	98:182 – 99:191	56:43.63	-52:28.83	——	——	110	83 P
						750	250 P
						1250	500
						1750	1000
						2500	1500 P
							2000
							2490
K1	96:224 – 97:144	56:33.60	-52:39.50	487 U	1077	——	75
					1793		425
							869
							1281
							2096
K11	97:204 – 98:190	56:33.60	-52:39.50	192 D	550	2590	——
					1370		
K21	98:218 – 99:198	56:33.60	-52:39.50	200 D	2591	561	——
						1482	
K4	96:225 – 97:191	58:30.00	-50:34.66	——	590	——	——
K5	96:224 – 97:143	57:29.80	-51:39.60	80 D	——	——	——
K15	97:201 – 98:189	57:06.10	-54:40.00	70 D	——	3023	——
K17	97:200 – 98:189	57:24.80	-55:40.00	261 D	——	——	——
K20	98:215 – 99:201	56:58.80	-54:34.80	67 D	——	3121	——

Table 2
(Table 2)

The eddy census: Bravo

Time	ΔT	$\tilde{V}$	Rot	Type	$\tilde{L}$
94:162:08	53	17	A	I	18±6
94:182:11	17	9	A	I	6±1
94:192:06	35	16	C	U	14±1
94:217:14	25	16	C	U	14±3
94:303:11	17	14	A	I	5±1
95:309:05	42	27	A	I	—
95:325:04	91	29	A	I	—
95:334:00	120	31	A	I	—
96:057:09	38	19	A	U	—
96:131:06	44	22	A	U	—
96:330:06	51	29	A	I	—
96:358:11	56	32	A	I	—
97:013:15	78	25	A	I	—
98:233:22	142	77	A	II	24±2
98:297:06	308	43	A	II	21±8
98:327:12	134	63	A	II	11±6
99:022:12	27	30	A	II	14±3
99:120:19	122	70	A	II	32±7
99:165:03	115	41	A	II	—

Table 3
(Table 3)

The eddy census: K1

Time	ΔT	$\hat{V}$	Rot	Type
96:337:06	55	20	A	I
97:022:17	40	17	A	I
97:252:04	51	43	A	II
97:266:12	122	39	A	II
97:343:18	26	30	A	II
97:362:02	92	20	A	I
98:019:05	45	20	A	I
98:137:05	48	40	A	U
98:146:21	49	31	A	U
98:232:04	118	37	A	II
98:299:05	275	47	A	II
99:019:08	31	30	A	II
99:111:19	127	57	A	U
99:160:06	141	36	A	U

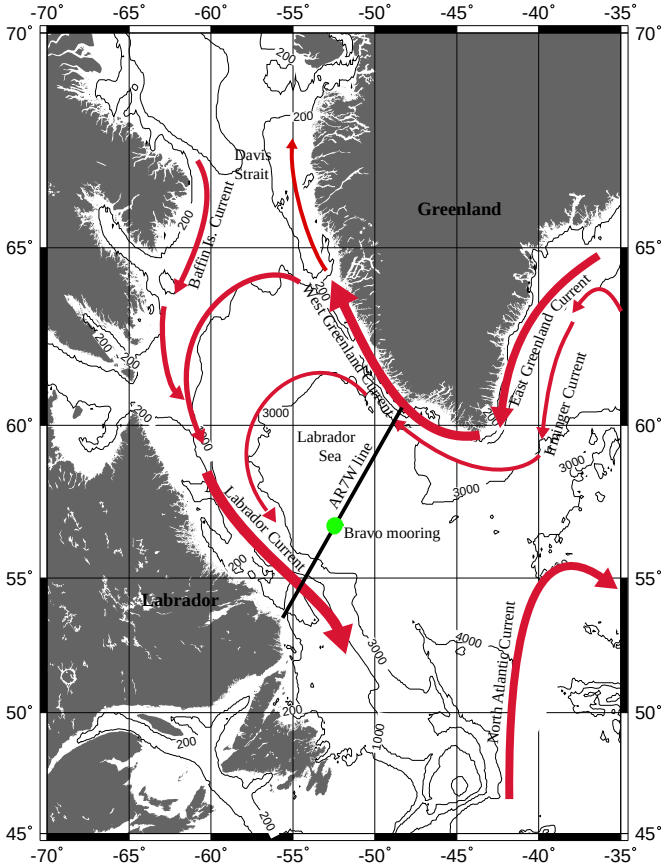

Figure 1. (Fig.1)

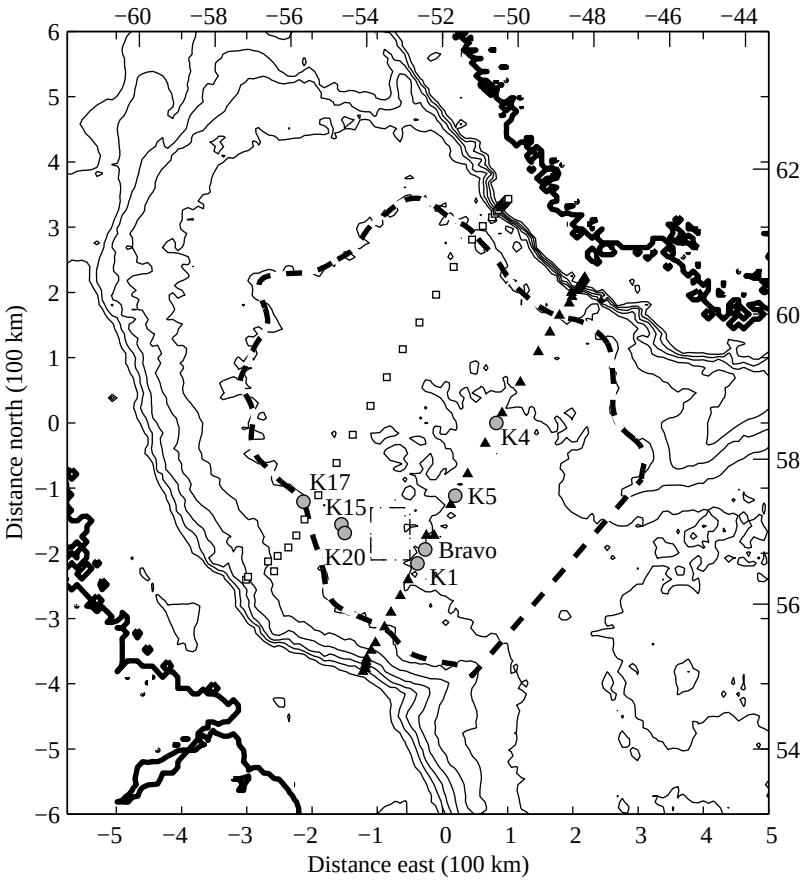

Figure 2. (Fig.2)

Figure 3. (Fig.3)

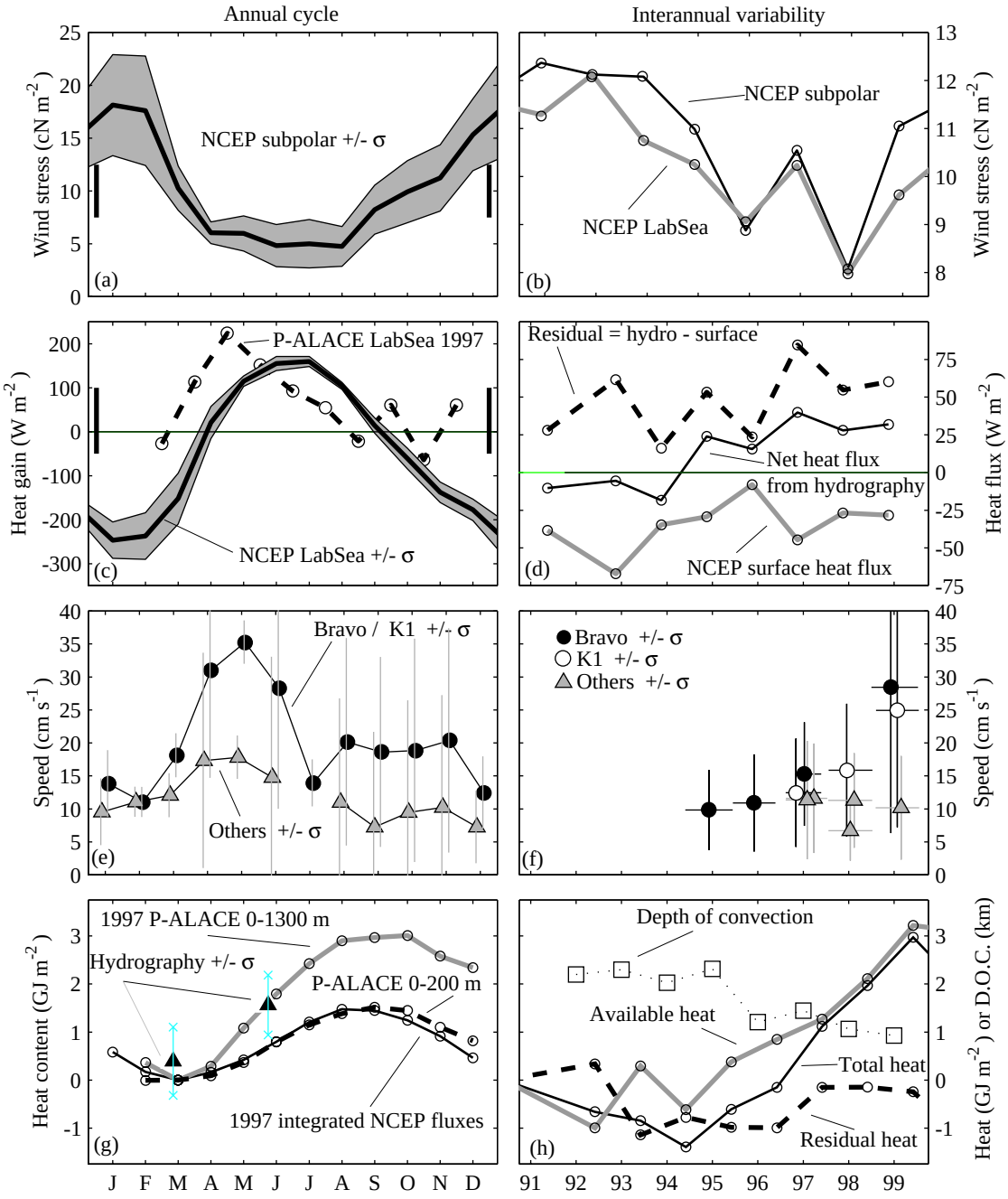

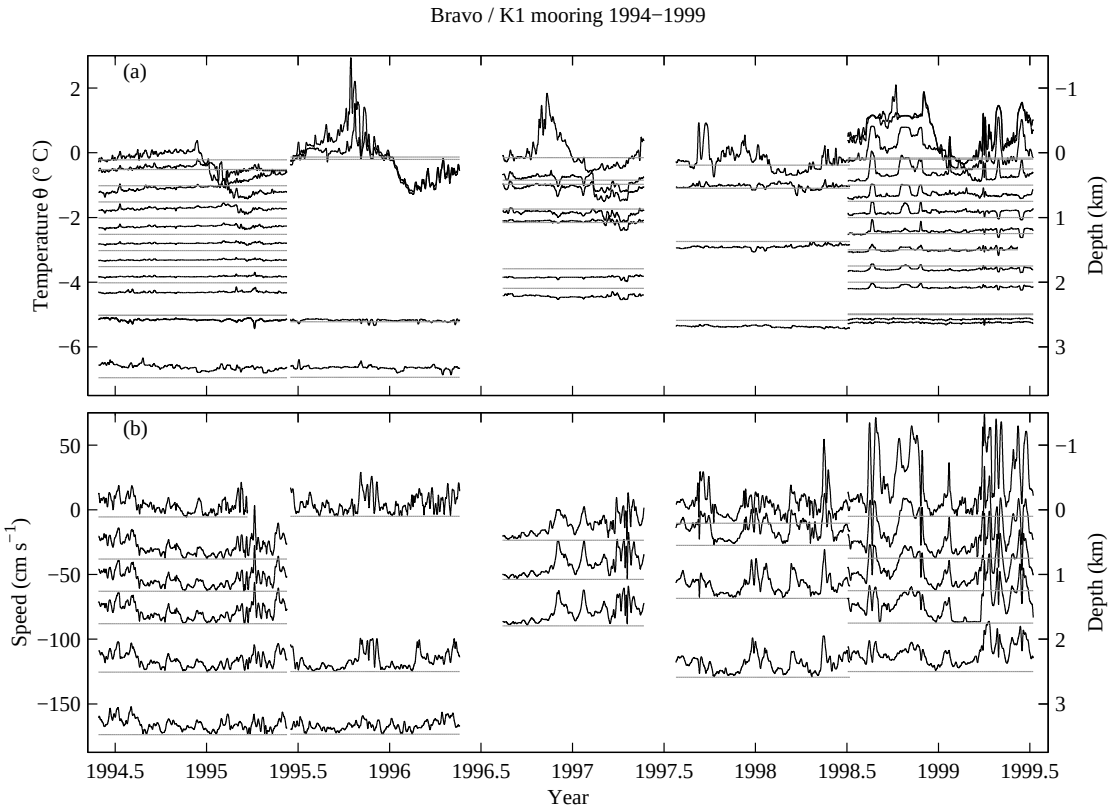

Figure 4. (Fig.4)

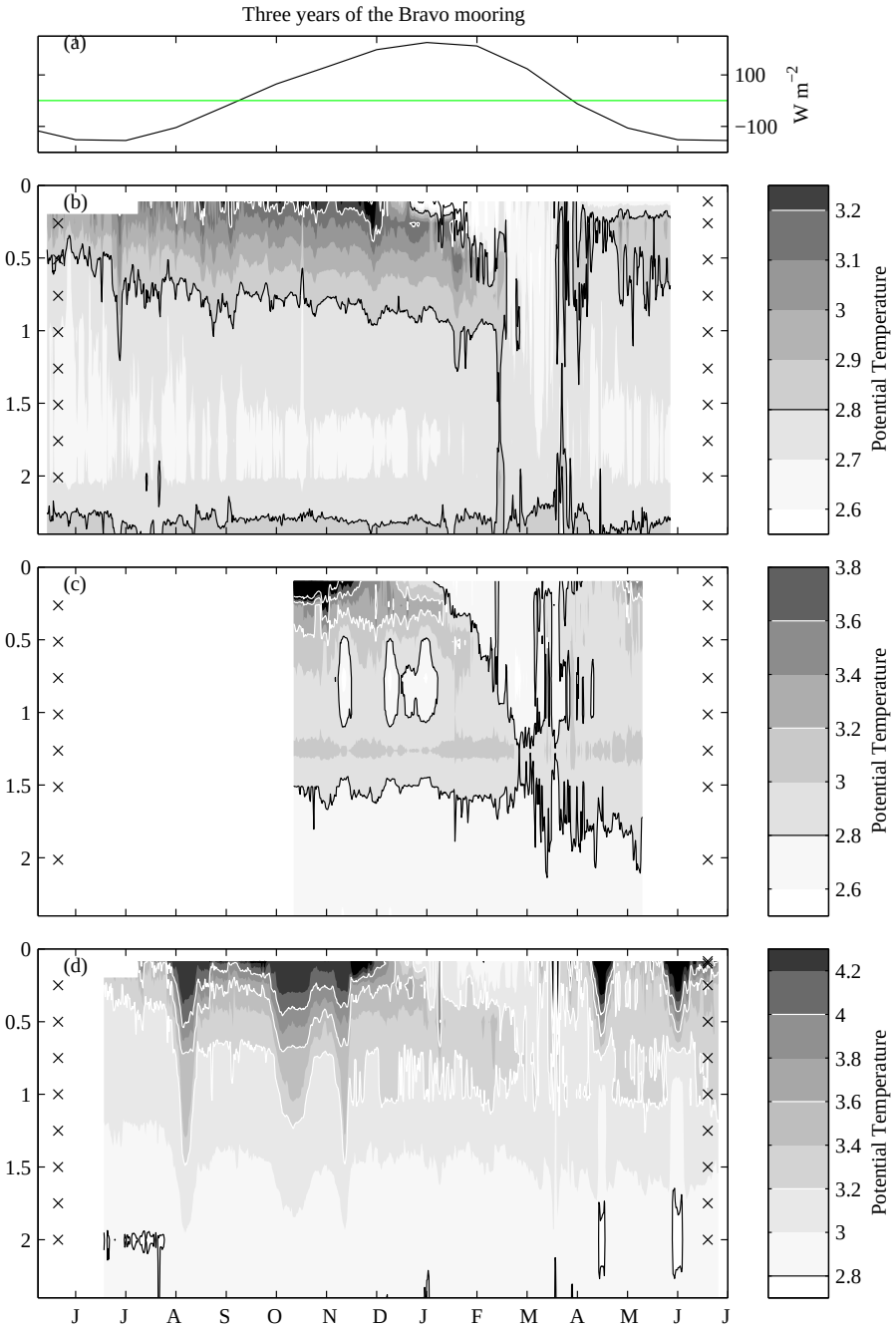

Figure 5. (Fig.5)

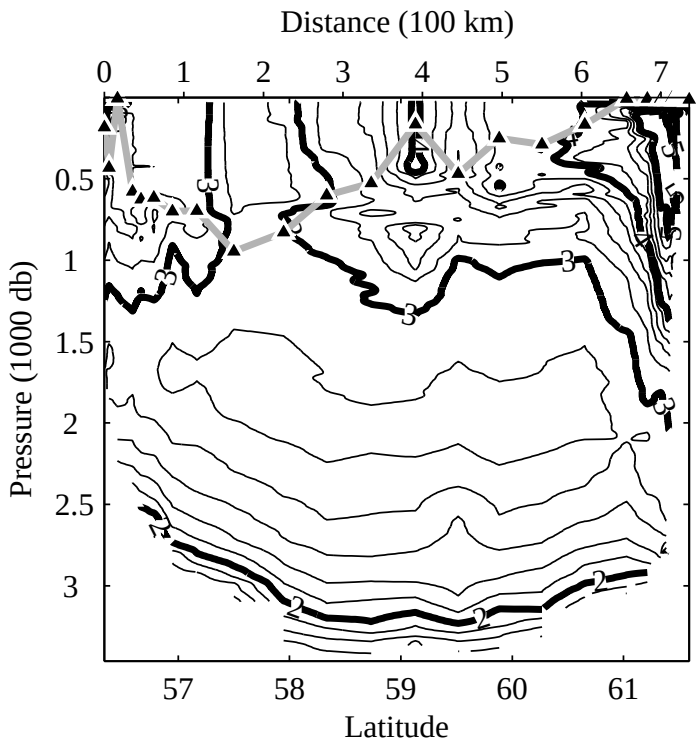

Figure 6. (Fig.6)

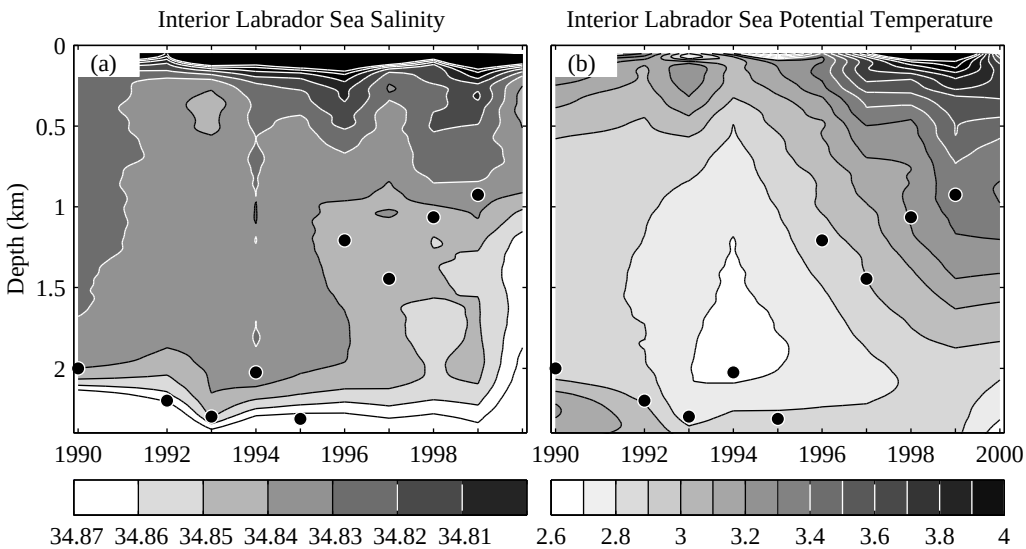

Figure 7. (Fig.7)

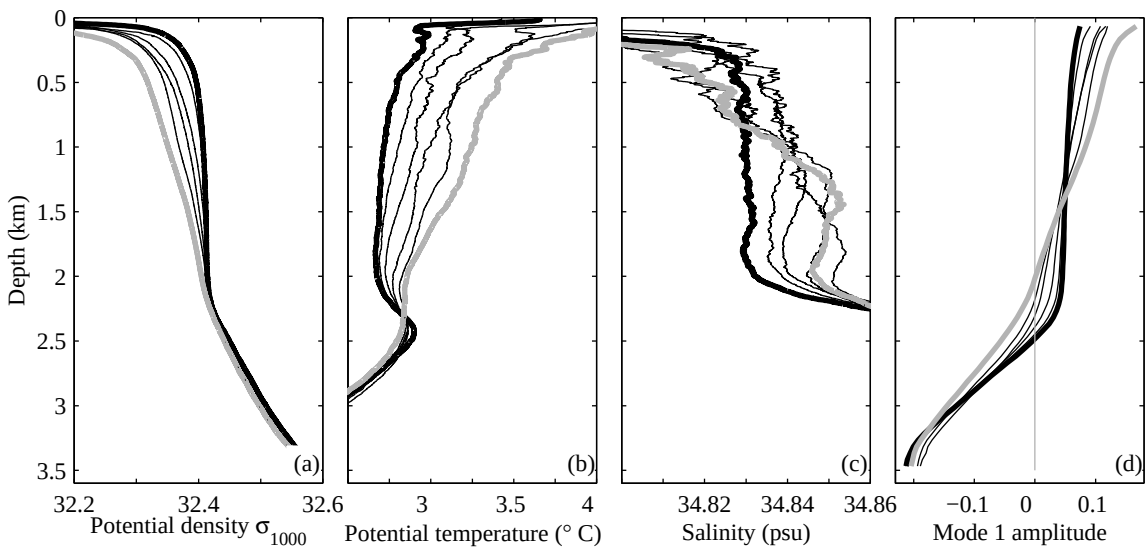

Figure 8. (Fig.8)

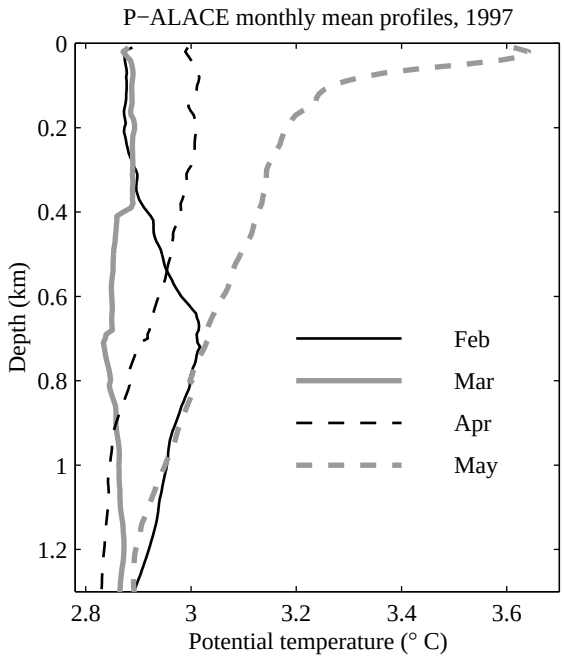

Figure 9. (Fig.9)

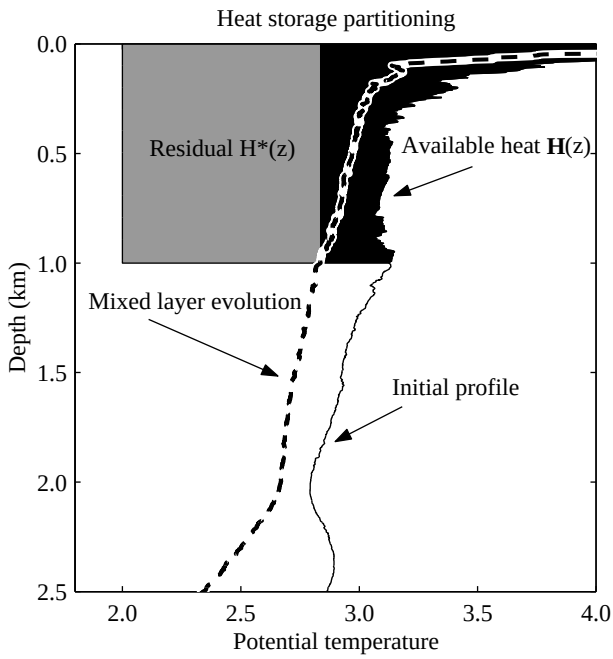

Figure 10. (Fig.10)

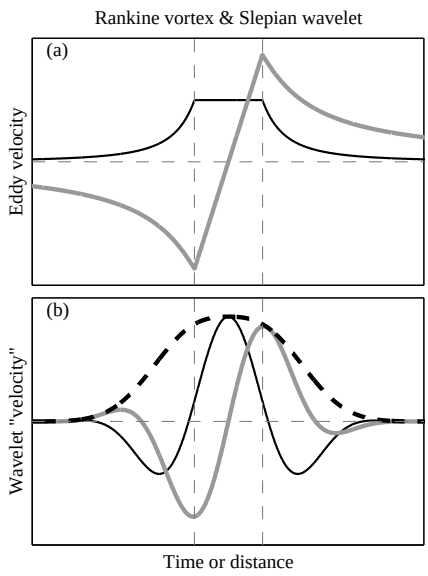

Figure 11. (Fig 11)

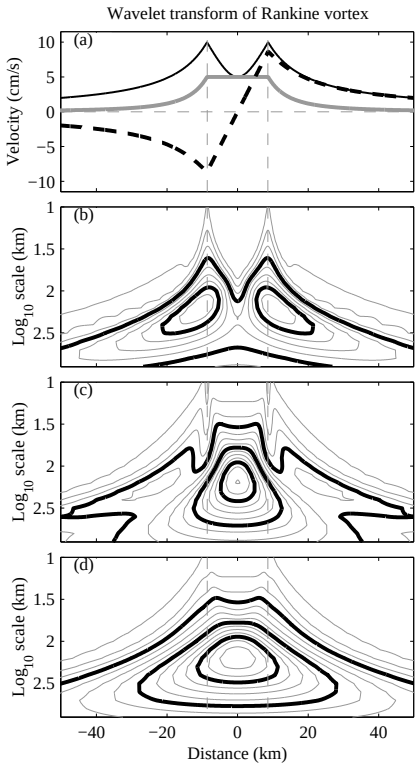

Figure 12. (Fig.12)

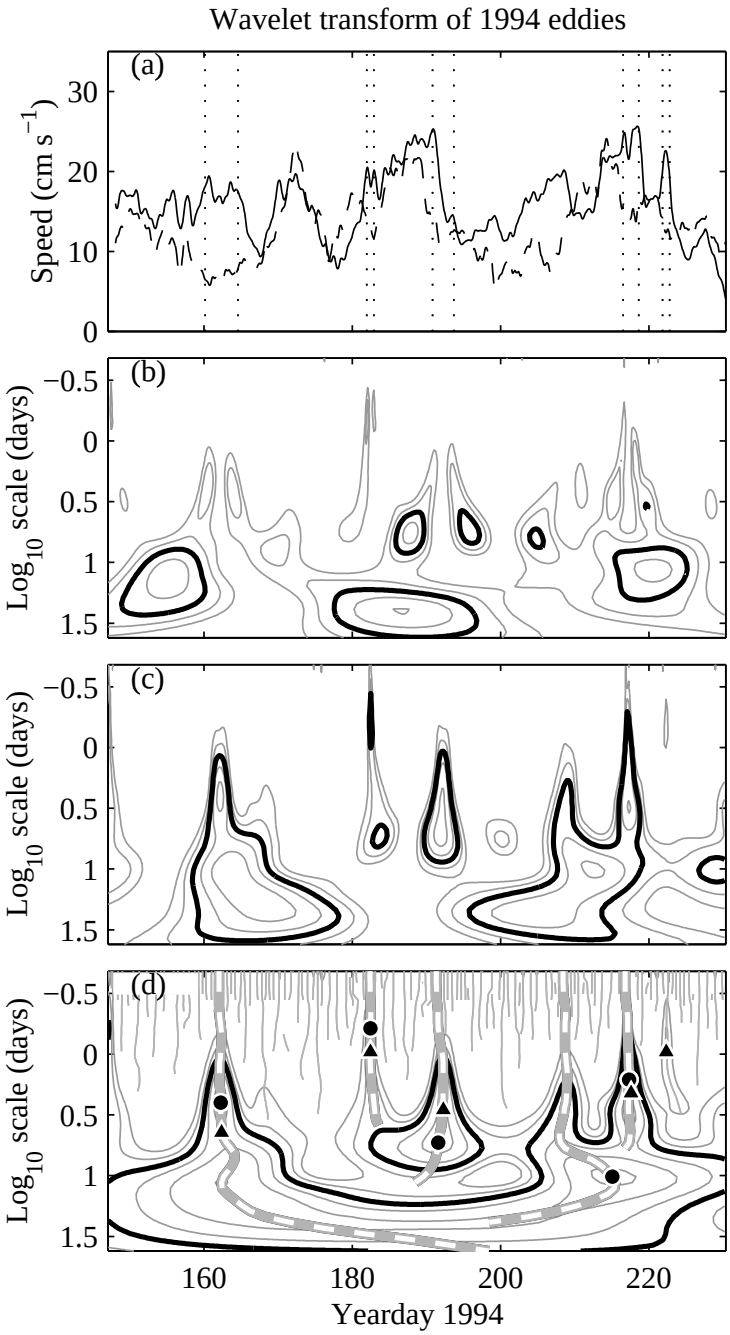

Figure 13. (Fig.13)

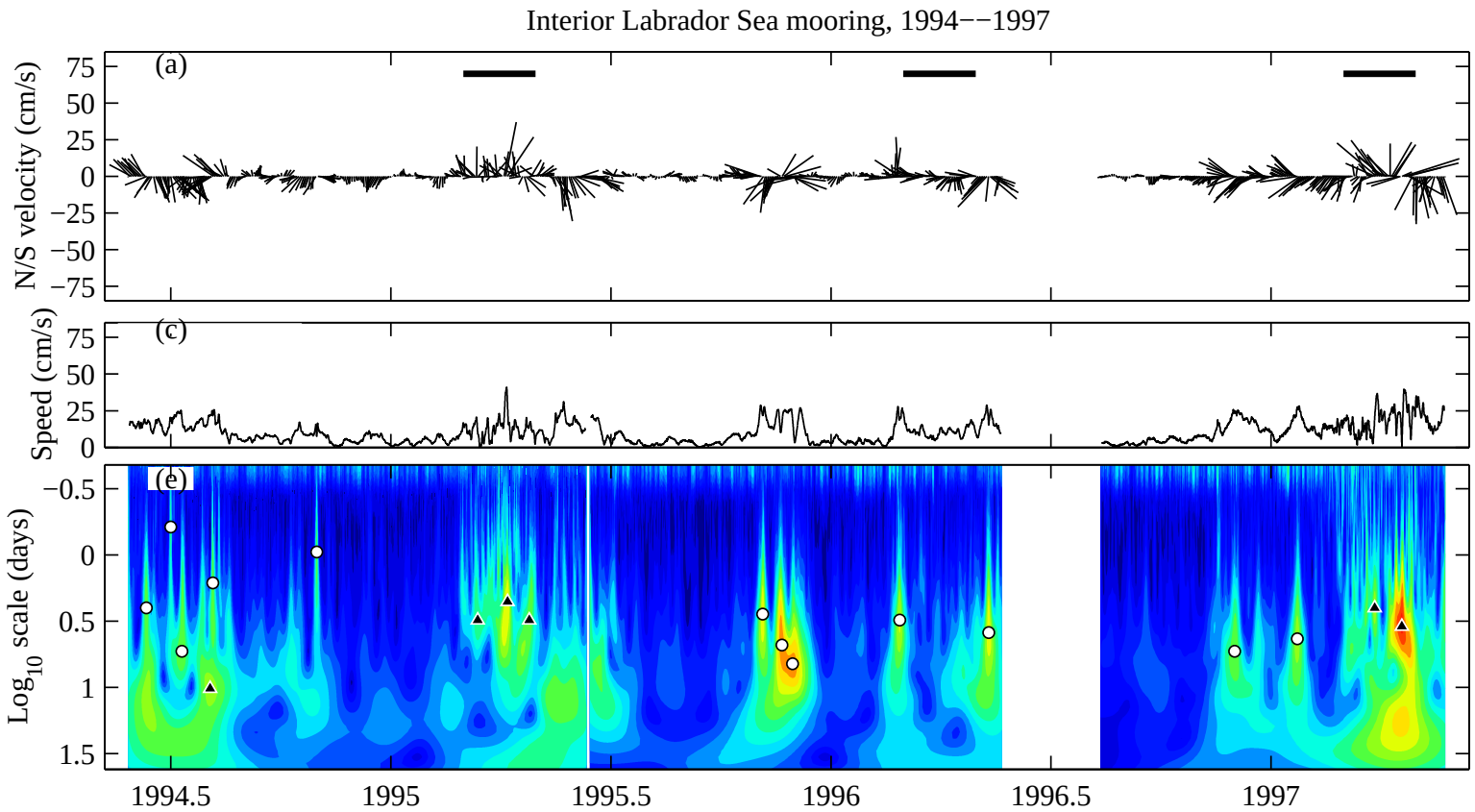

Figure 14: (Fig.14 pt1)

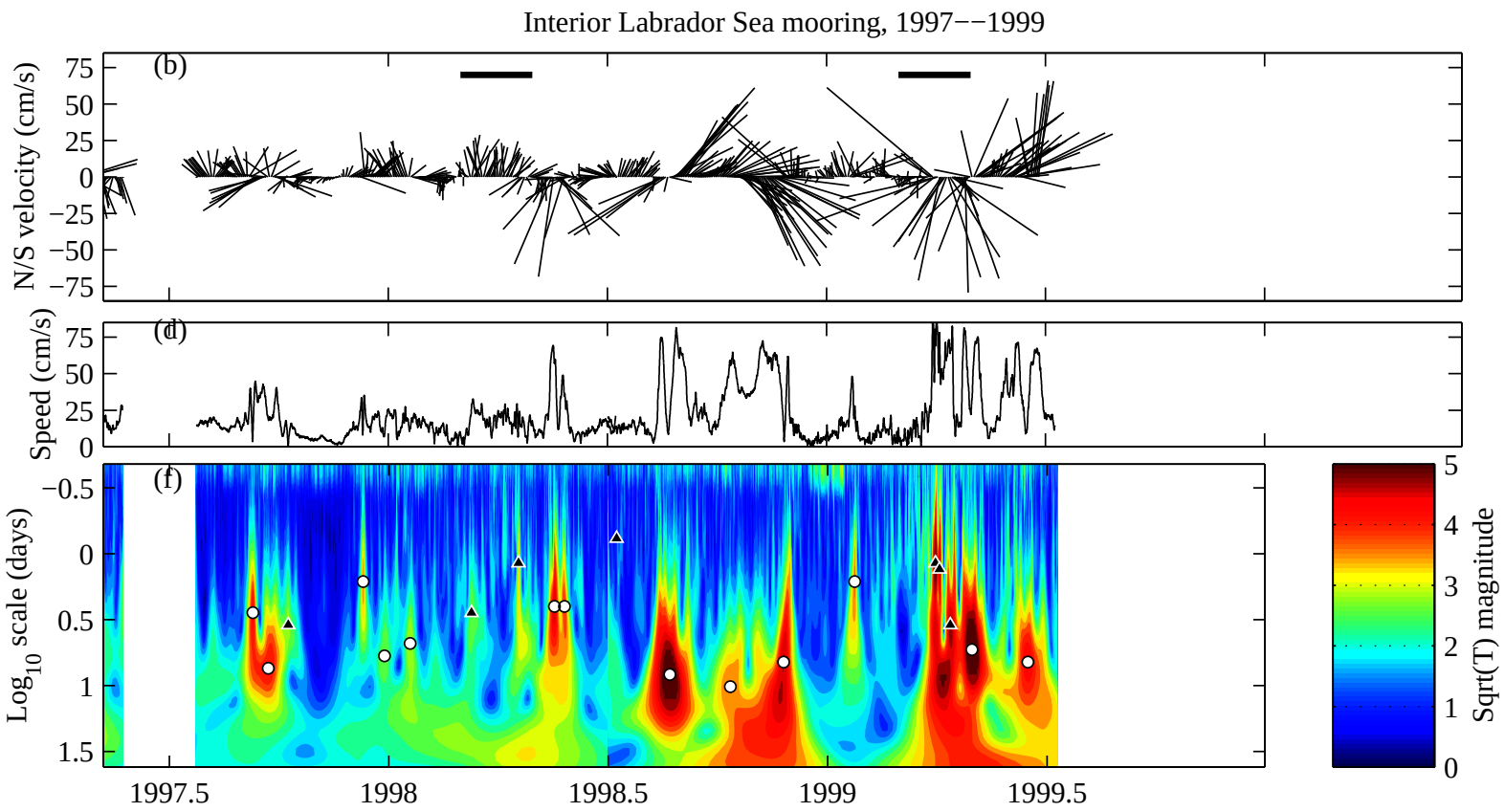

Figure 14: (Fig.14 pt 2)

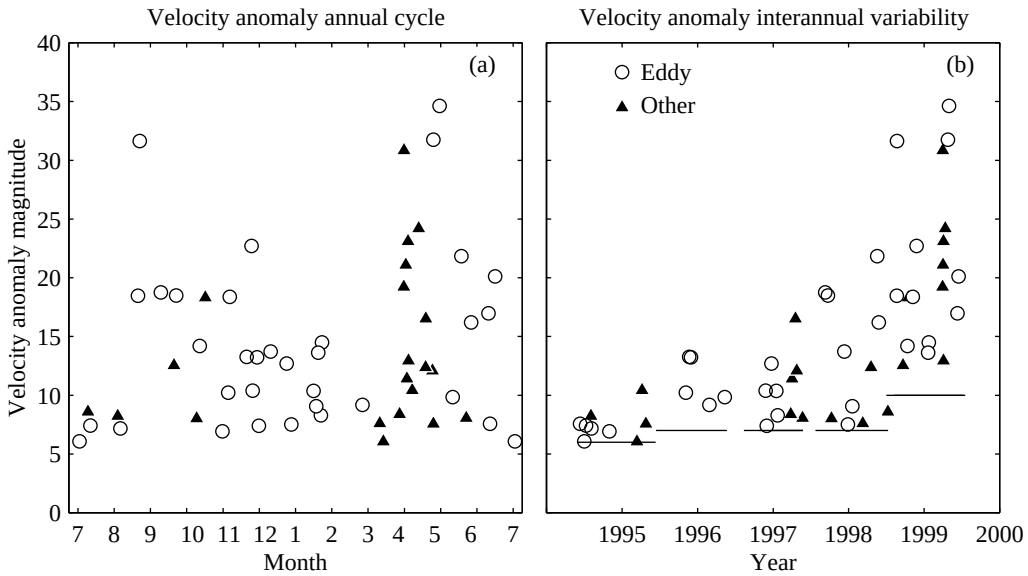

Figure 15. (Fig.15)

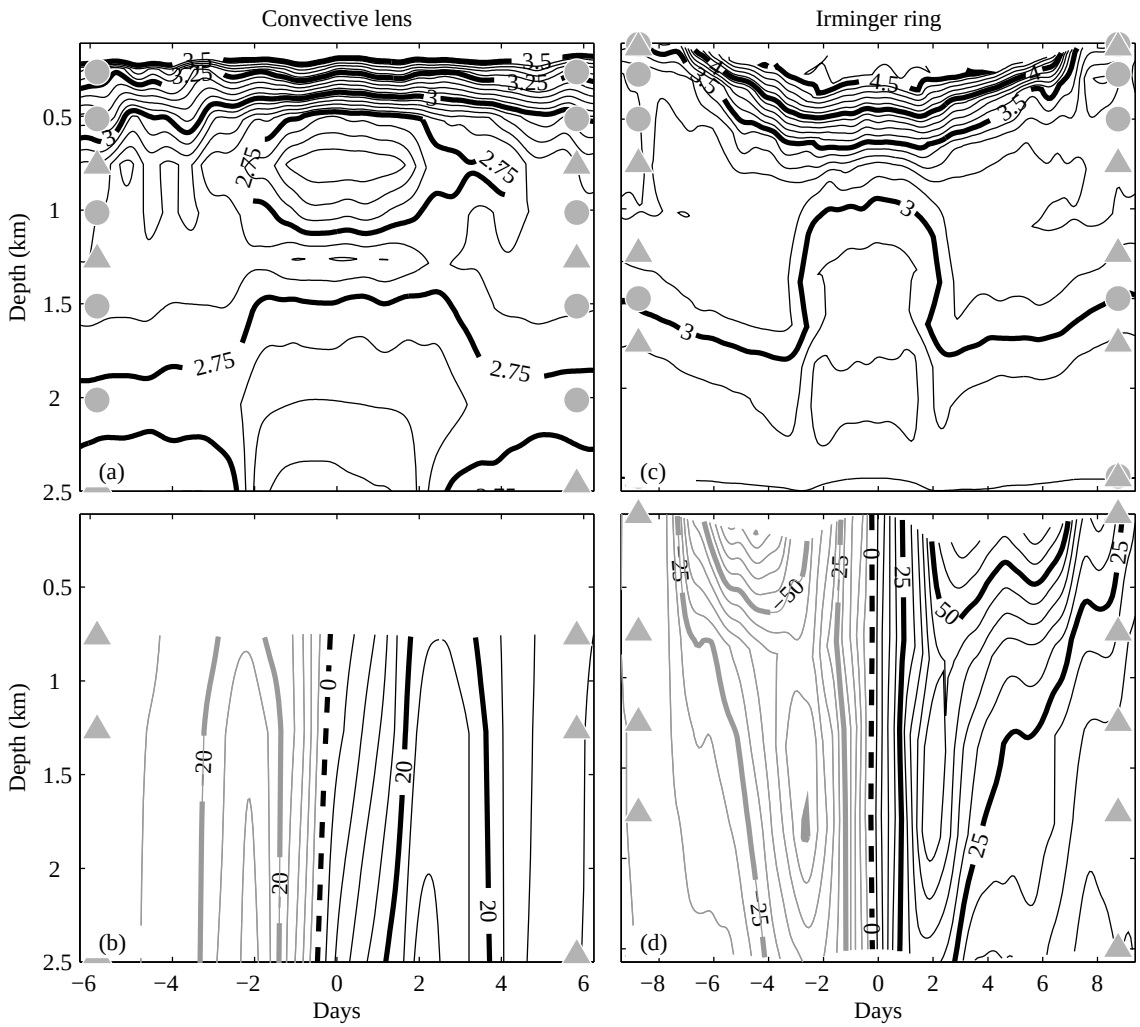

Figure 16. (Fig.16)

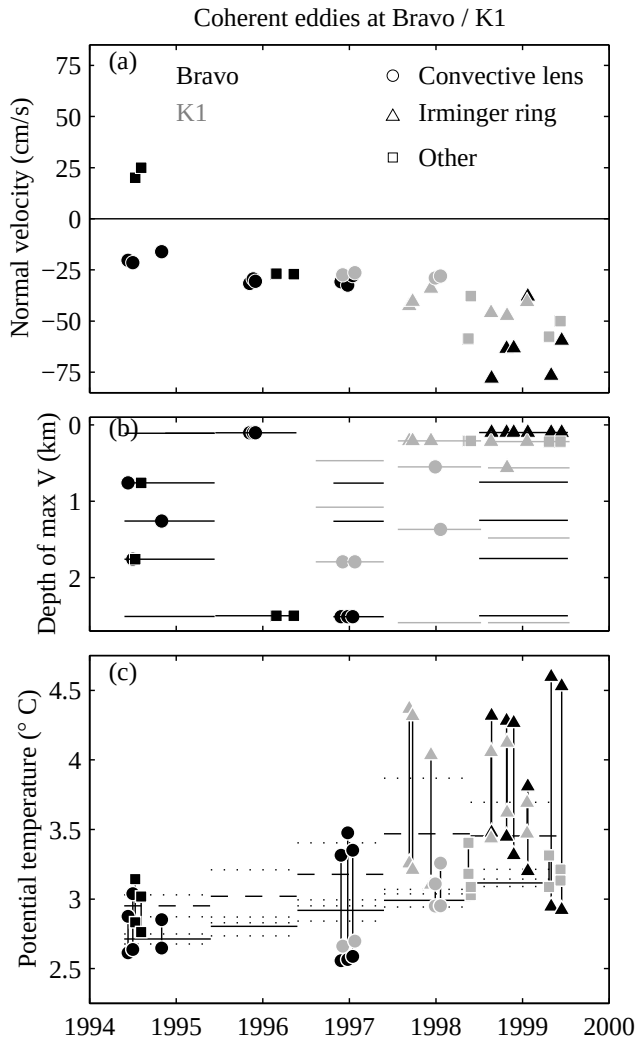

Figure 17. (Fig.17)

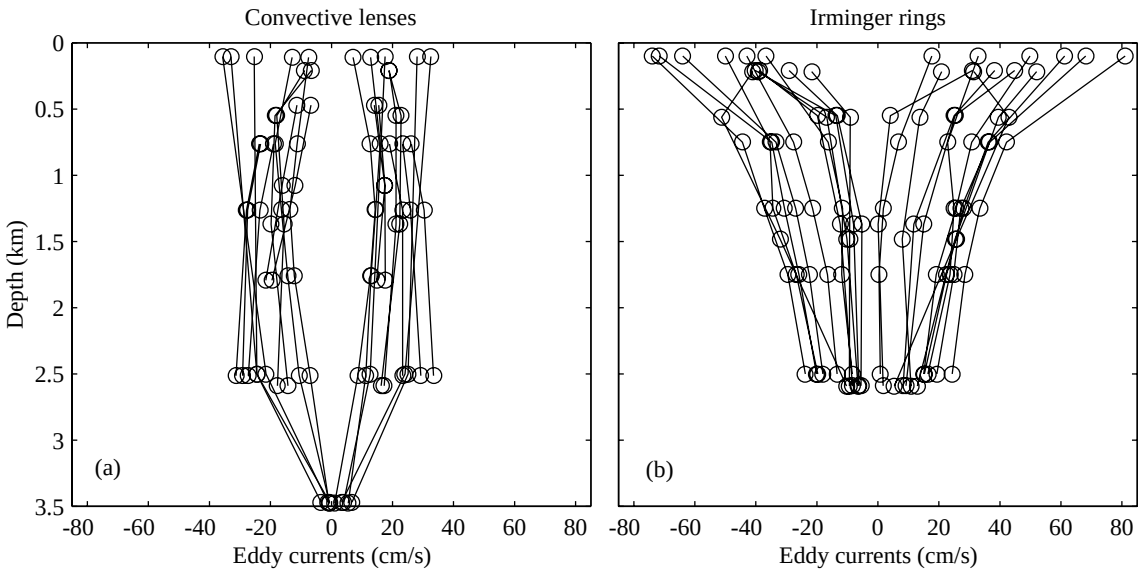

Figure 18. (Fig.18)

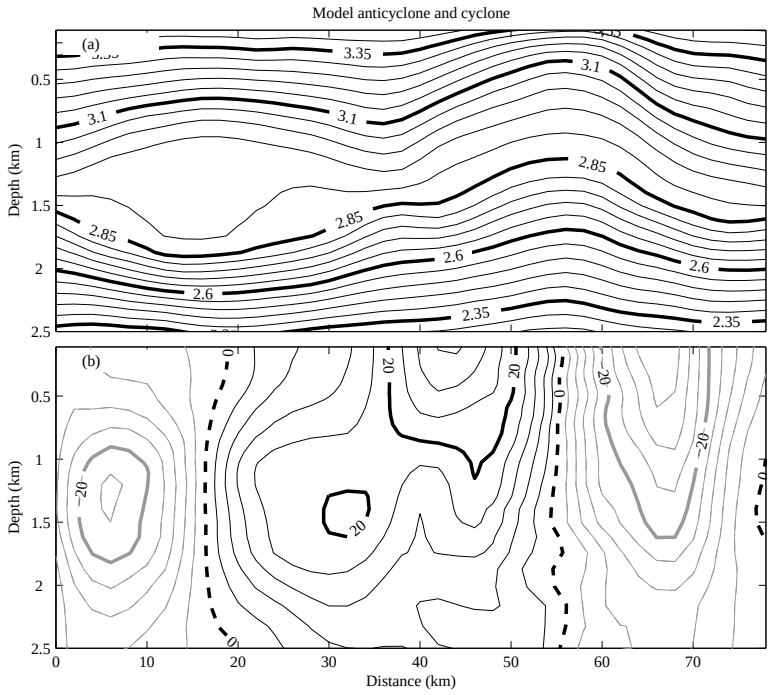

Figure 19. (Fig.19)

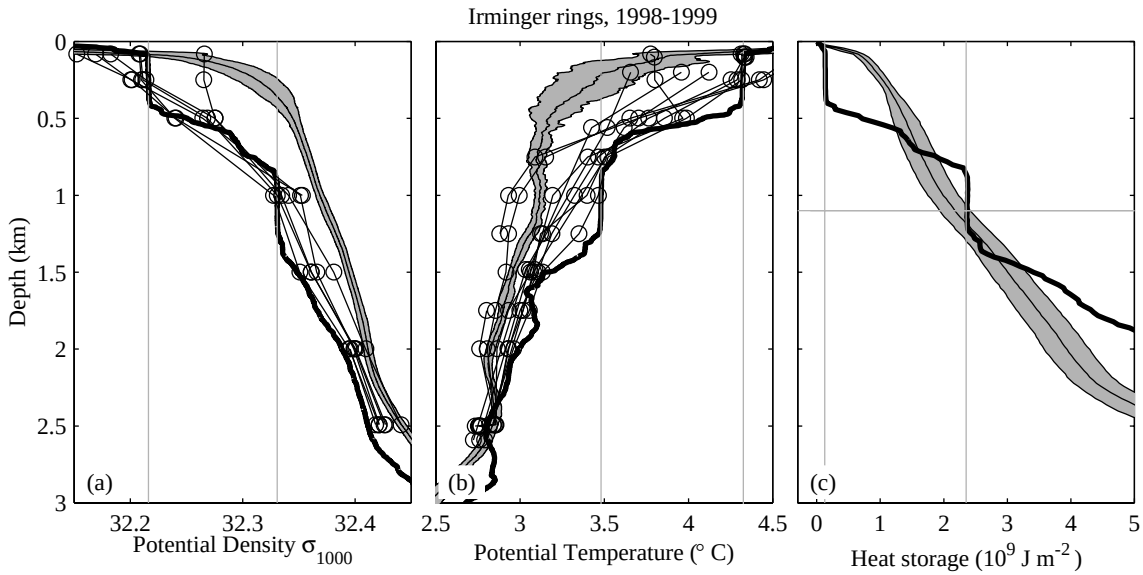

Figure 20. (Fig.20)

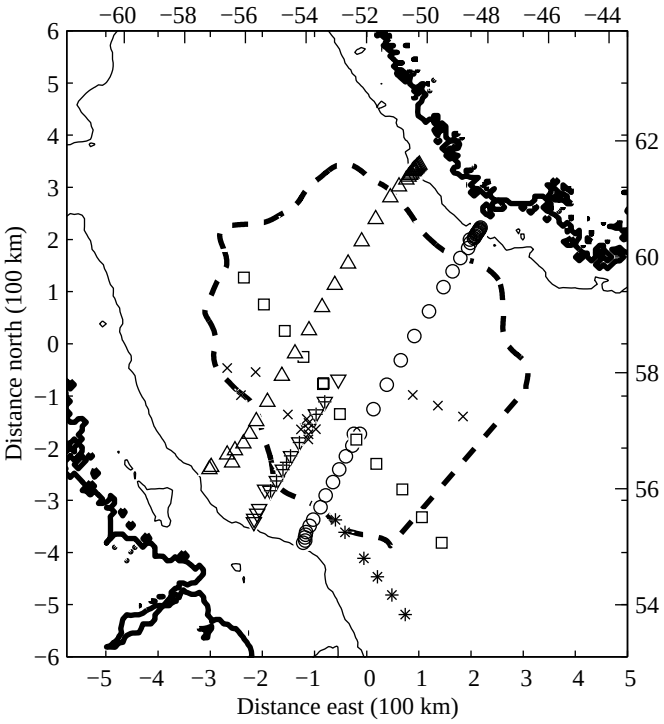

Figure 21. (Fig.21)

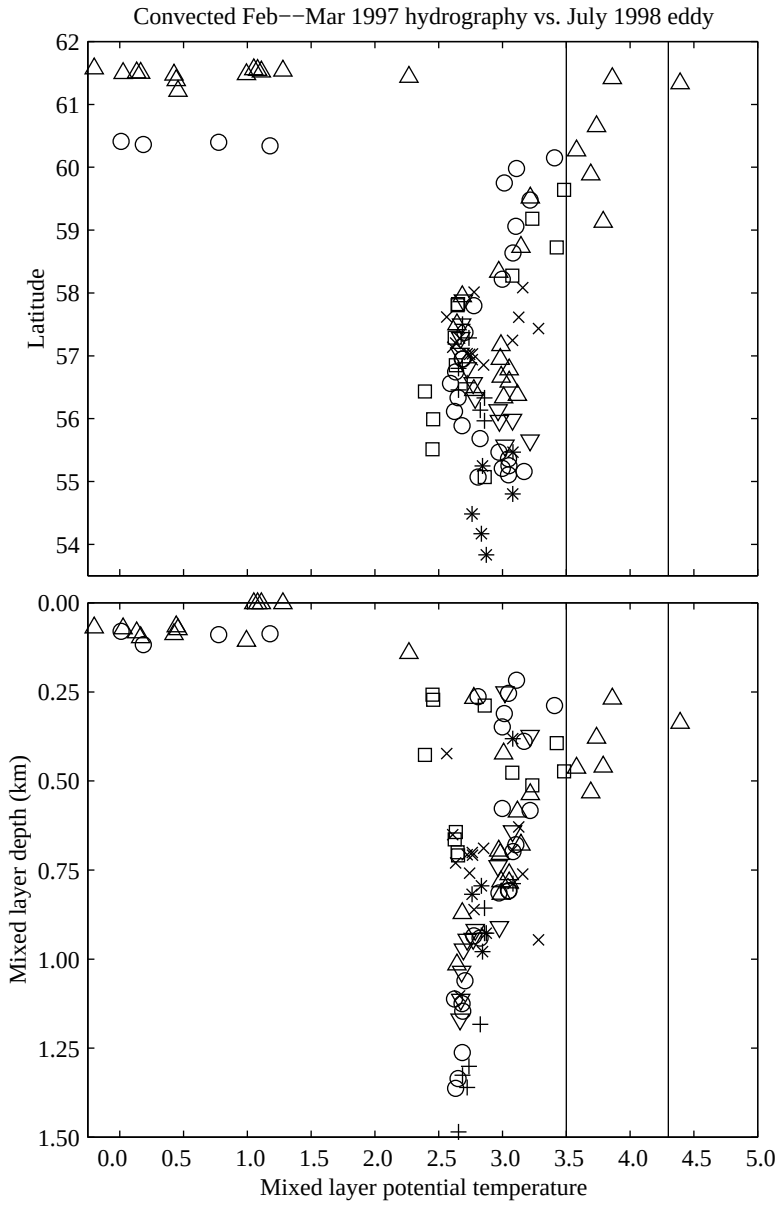

Figure 22. (Fig.22)

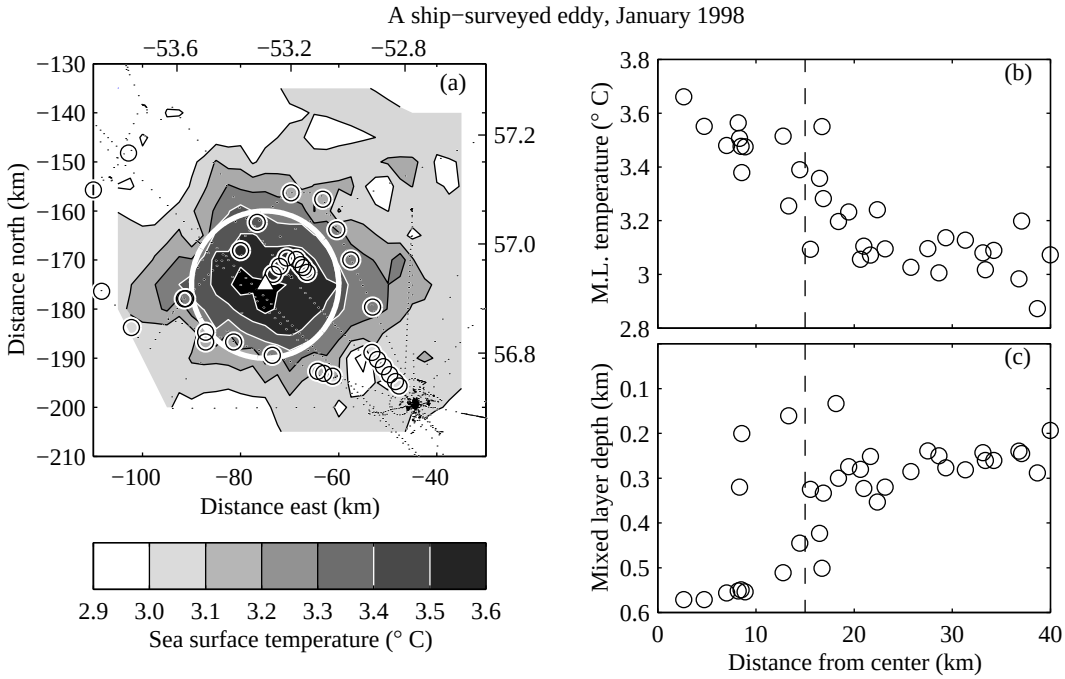

Figure 23. (Fig.23)

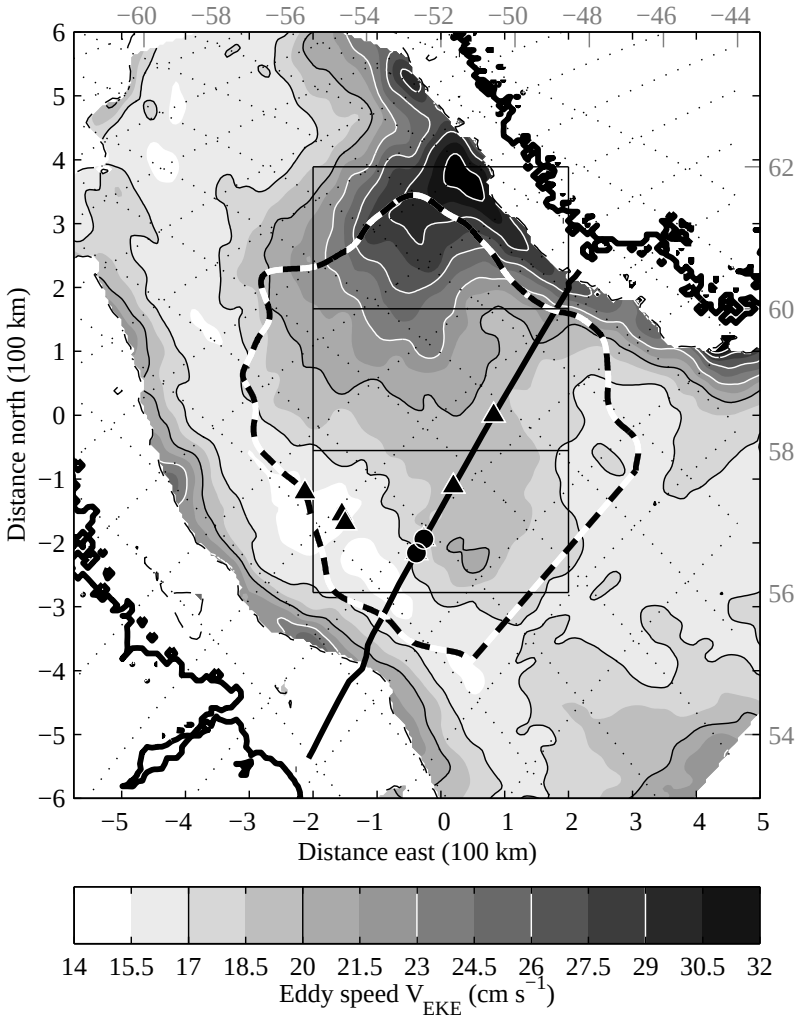

Figure 24. (Fig.24)

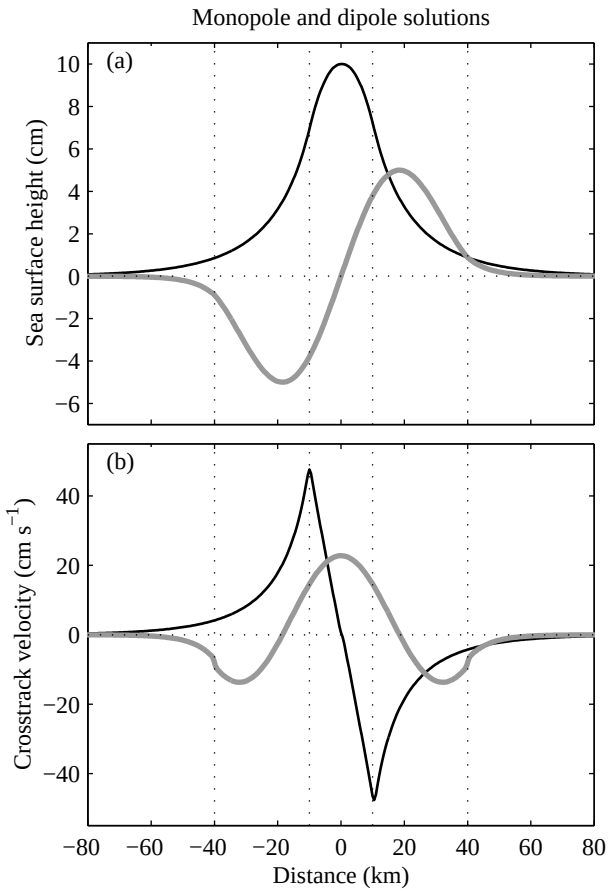

Figure 25. (Fig.25)

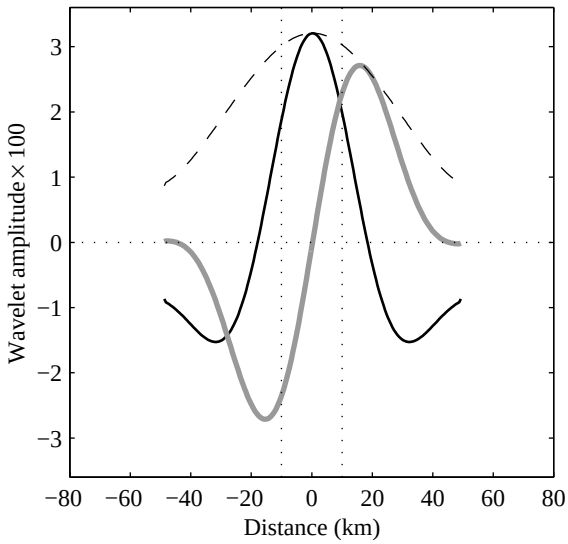

Figure 26. (Fig.26)

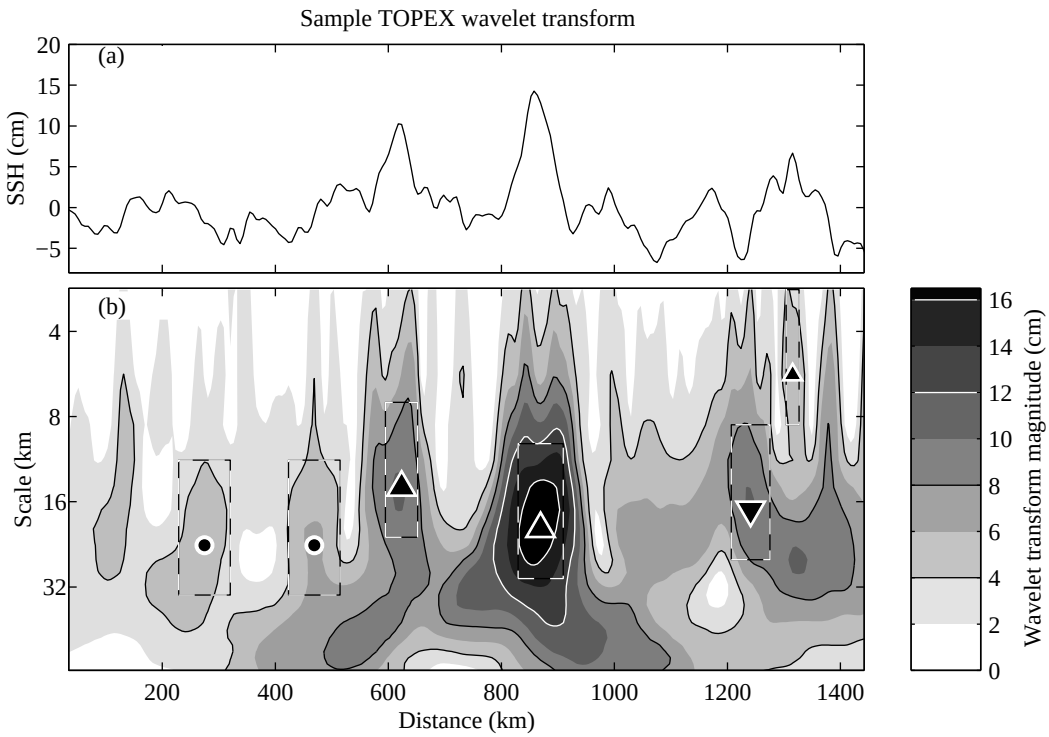

Figure 27. (Fig.27)

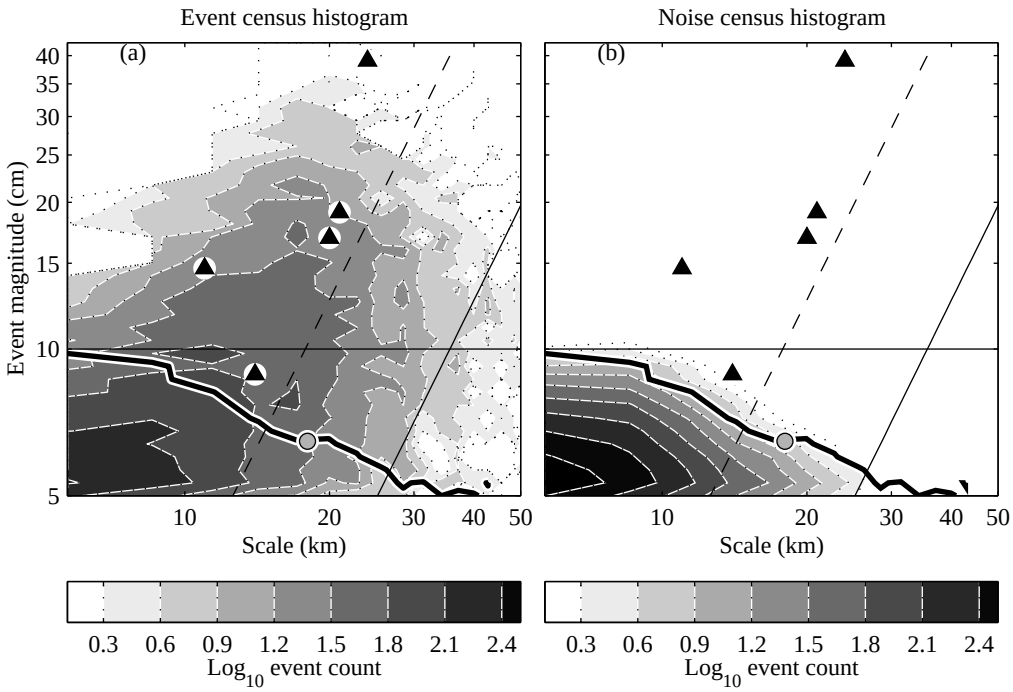

Figure 28. (Fig.28)

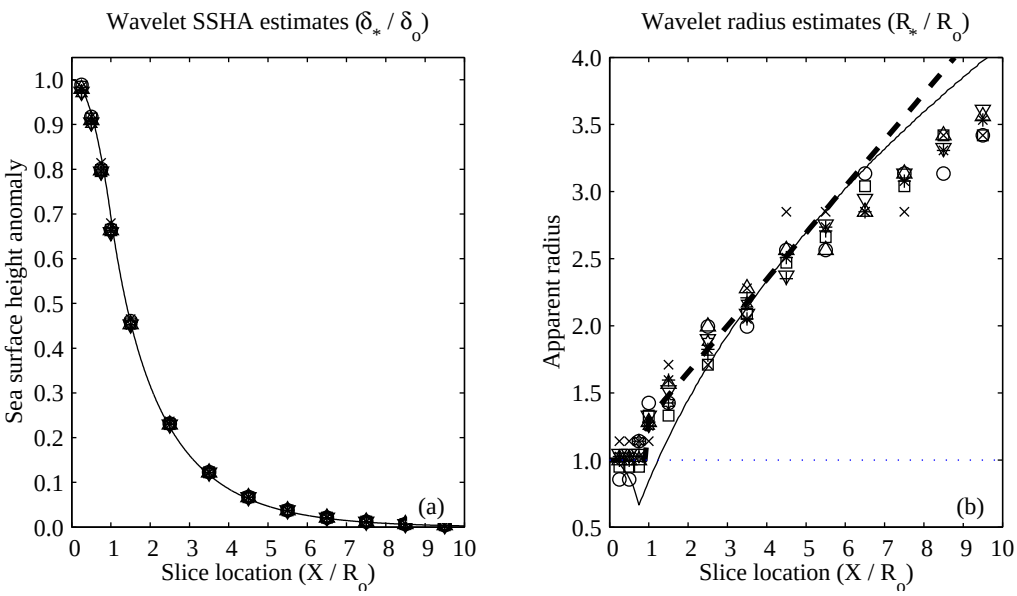

Figure 29. (Fig.29)

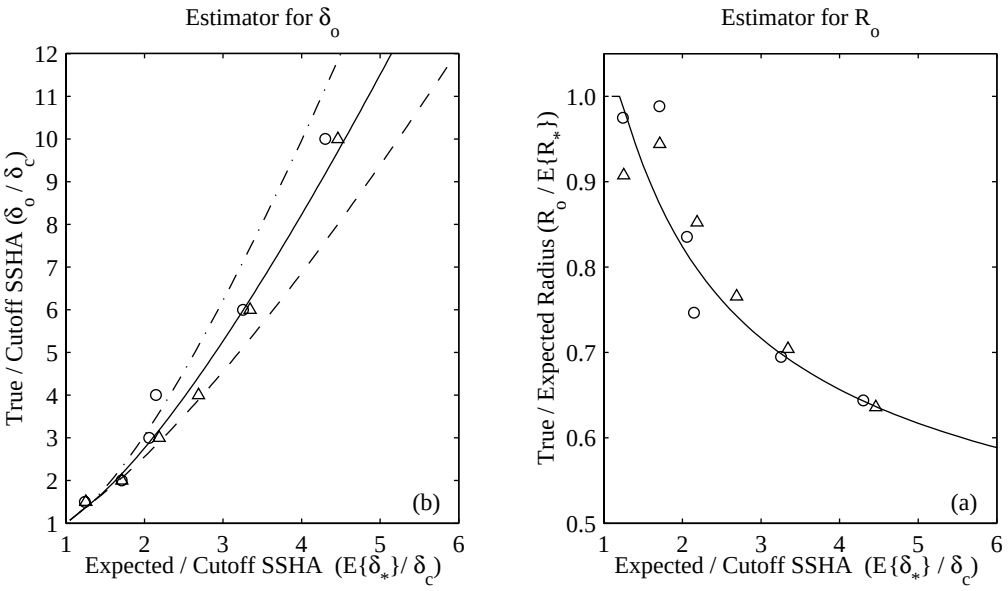

Figure 30. (Fig.30)

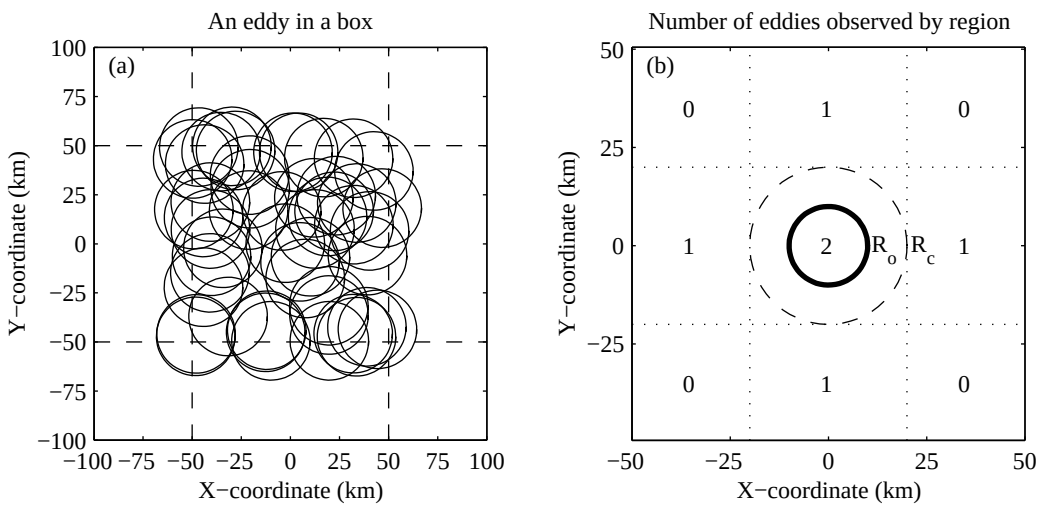

Figure 31. (Fig.31)

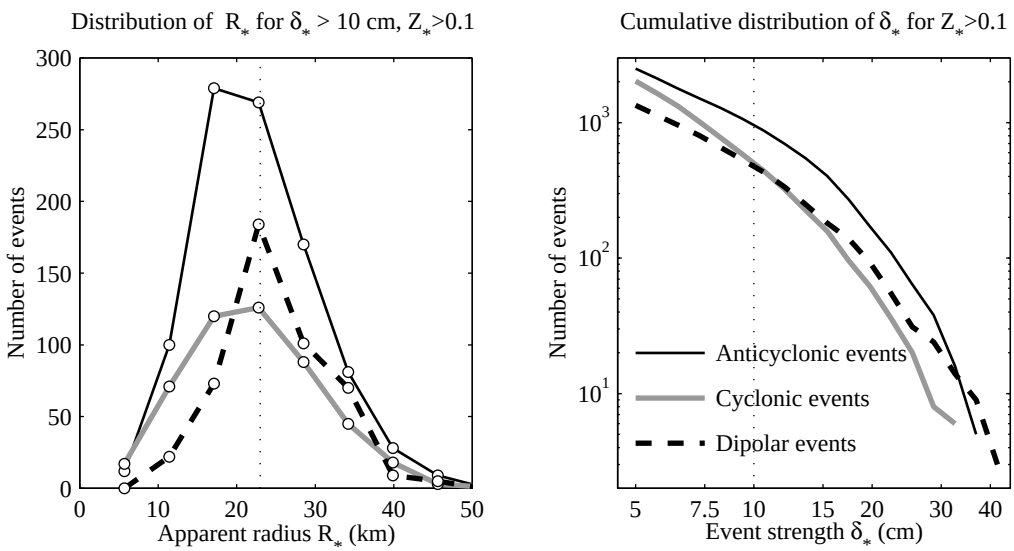

Figure 32. (Fig.32)

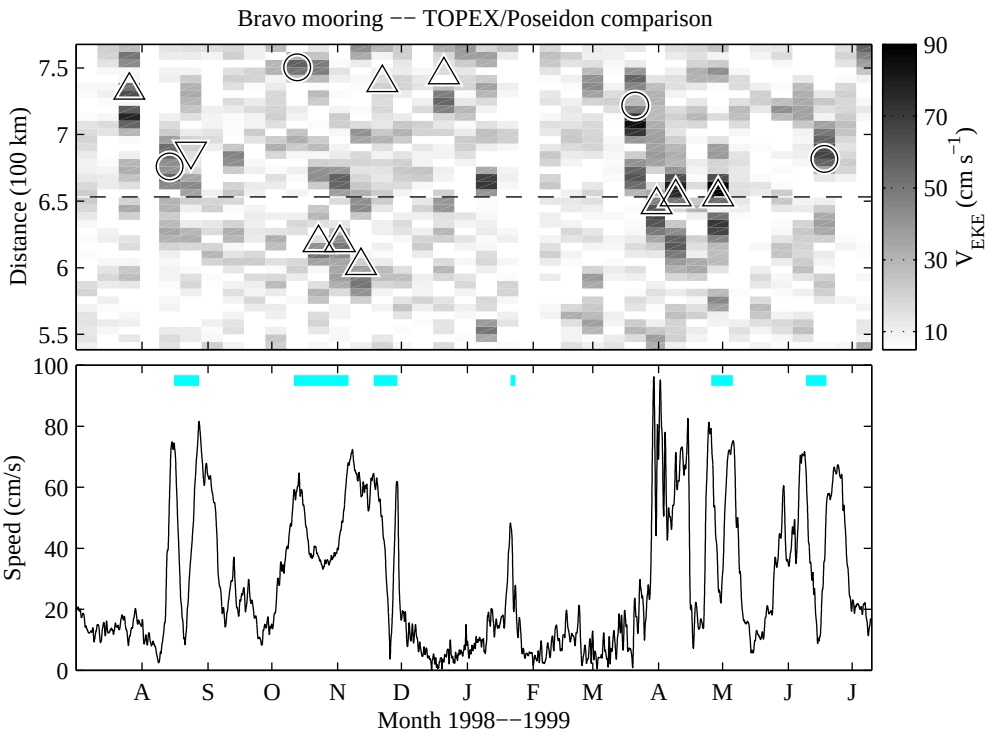

Figure 33. (Fig.33)

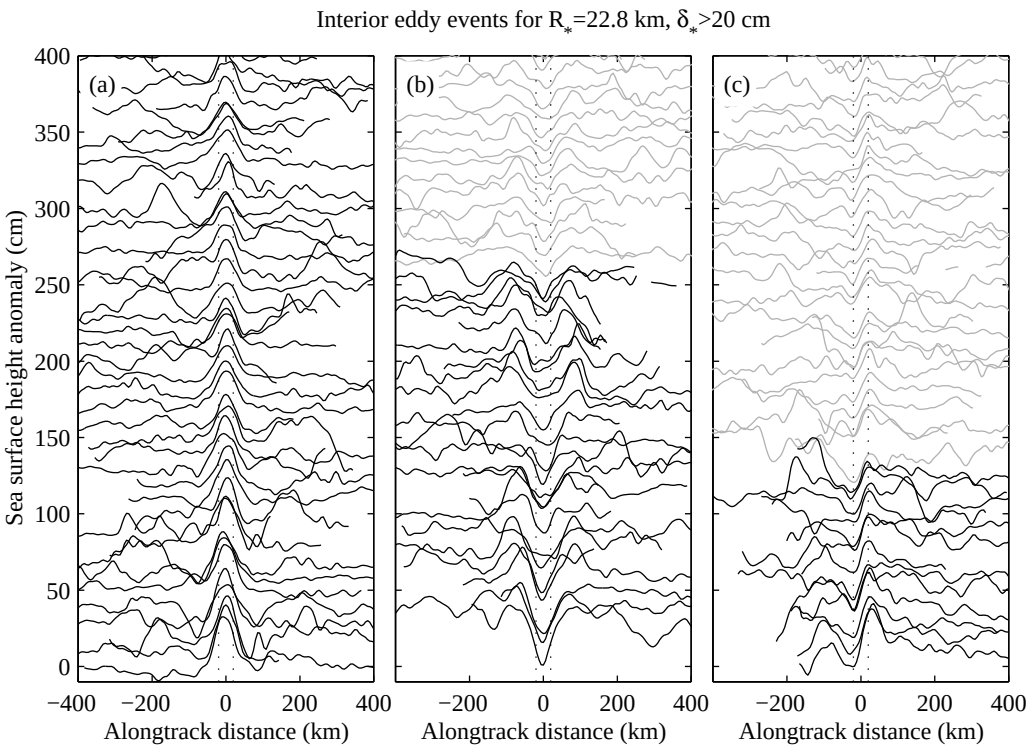

Figure 34. (Fig.34)

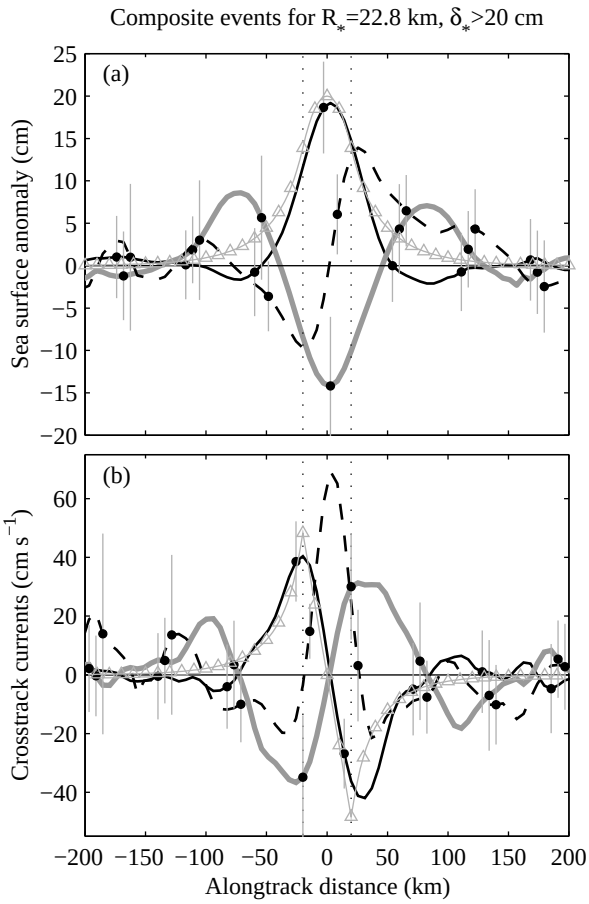

Figure 35. (Fig.35)

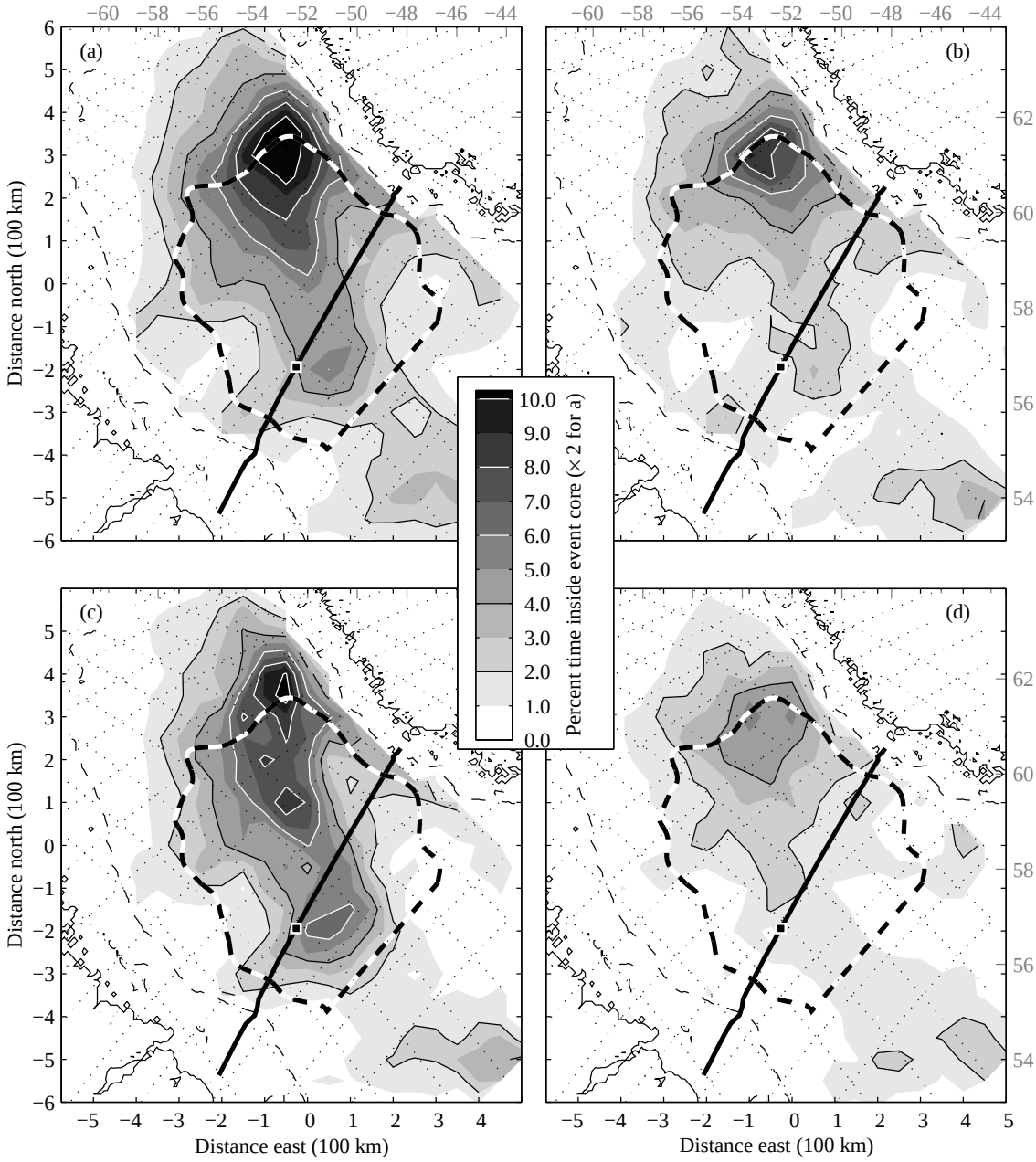

Figure 36. (Fig.36)

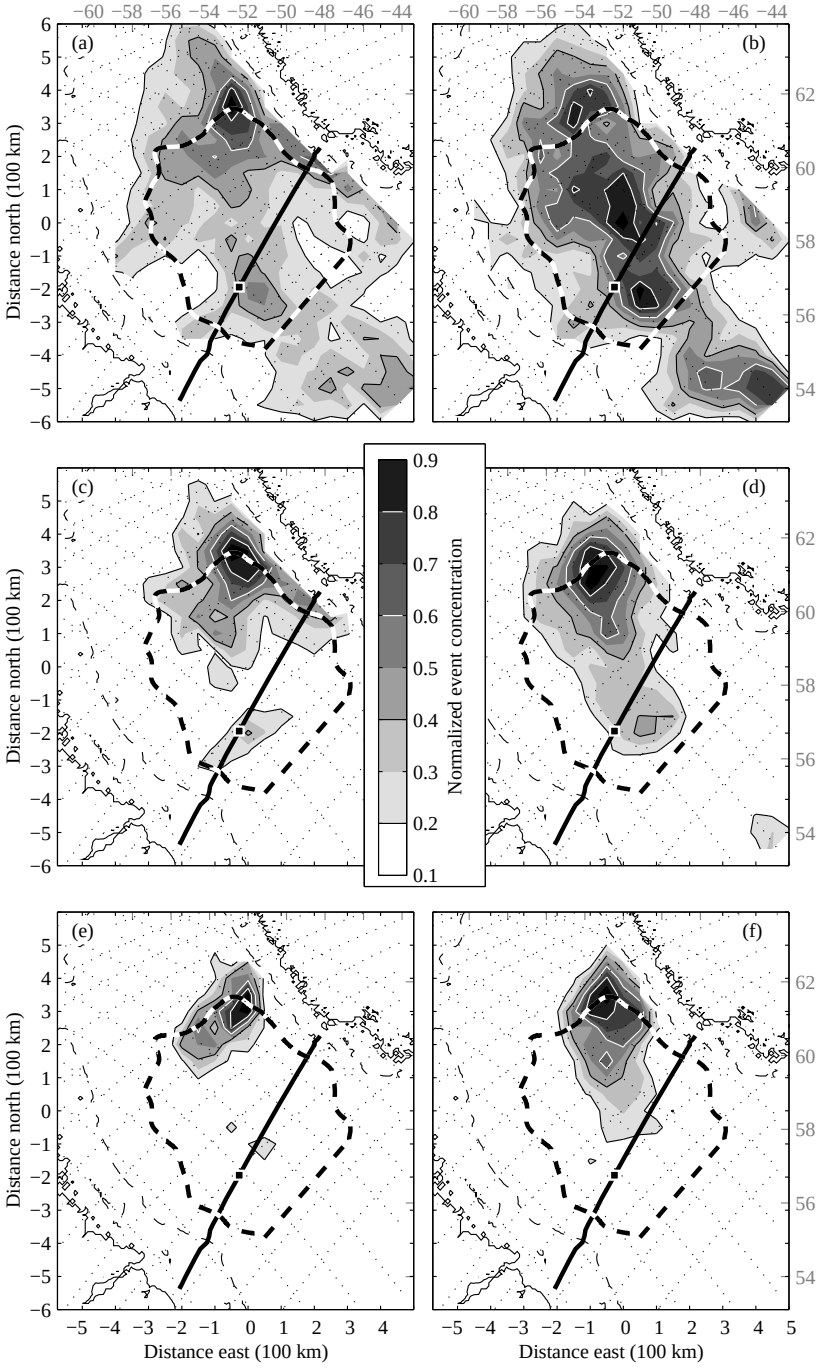

Figure 37. (Fig.37)

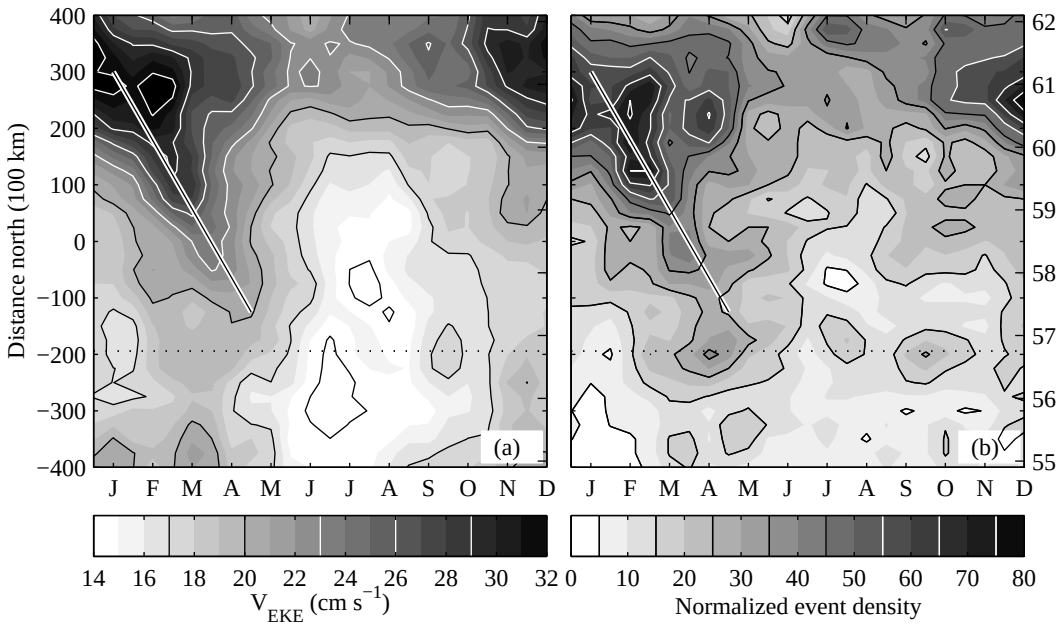

Figure 38. (Fig.38)

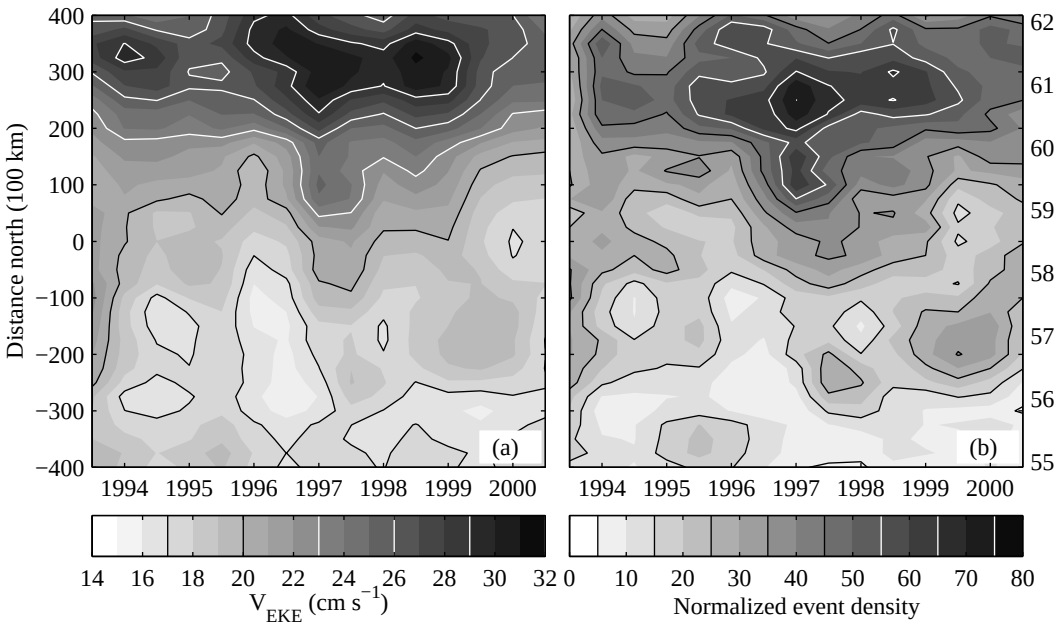

Figure 39. (Fig.39)

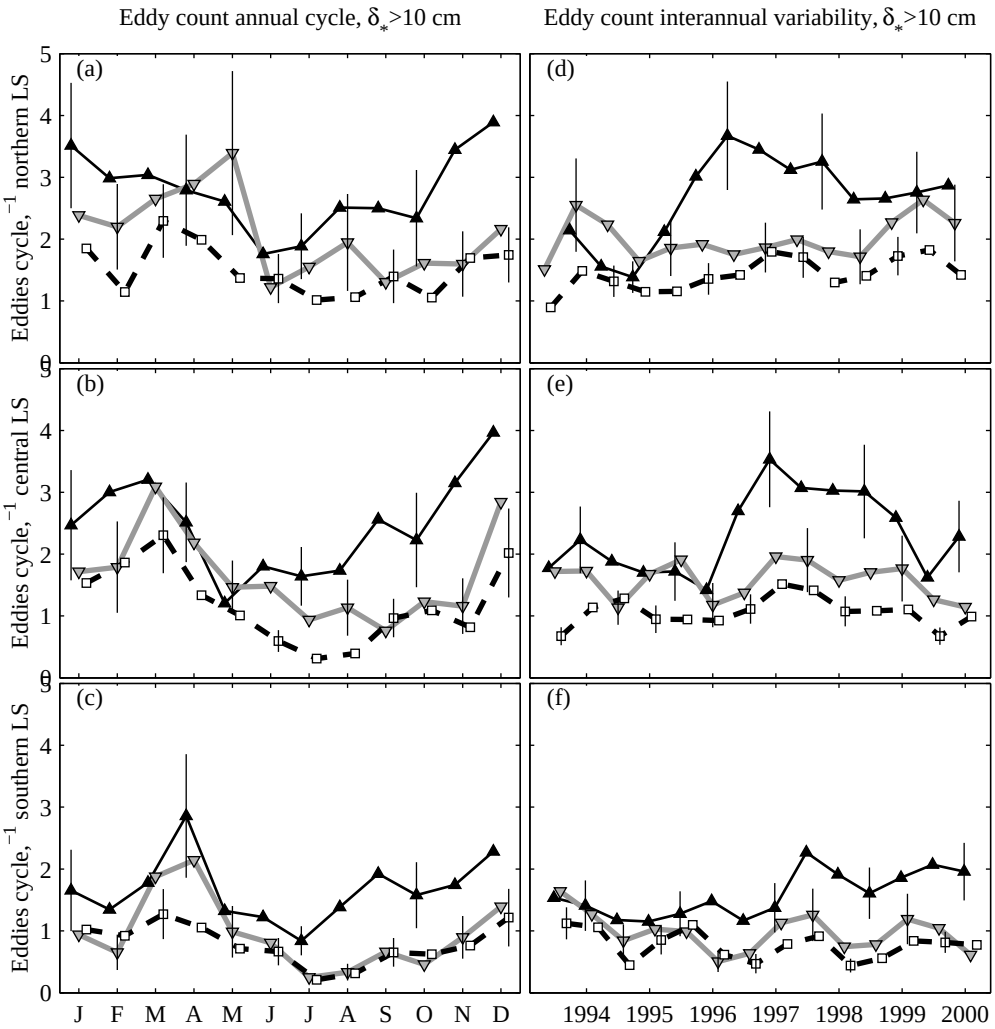

Figure 40. (Fig.40)

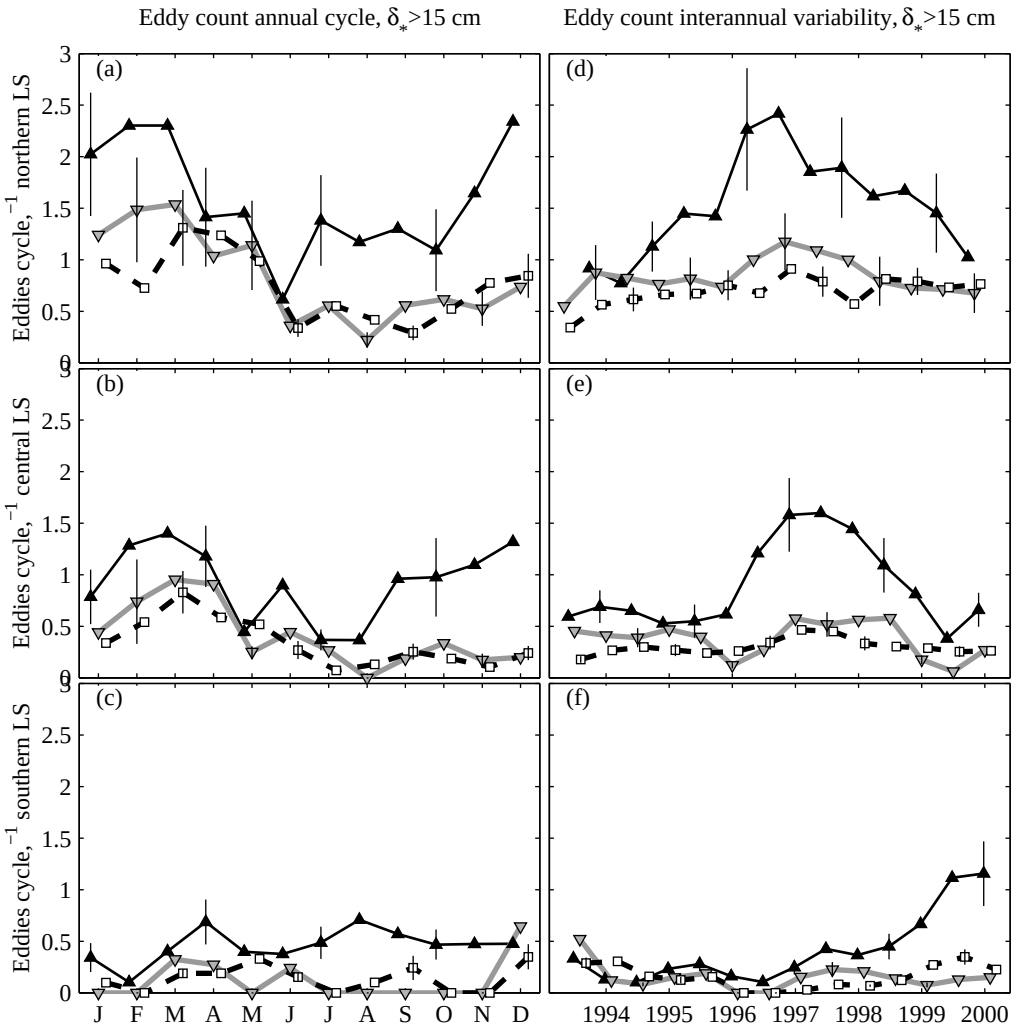

Figure 41. (Fig.41)

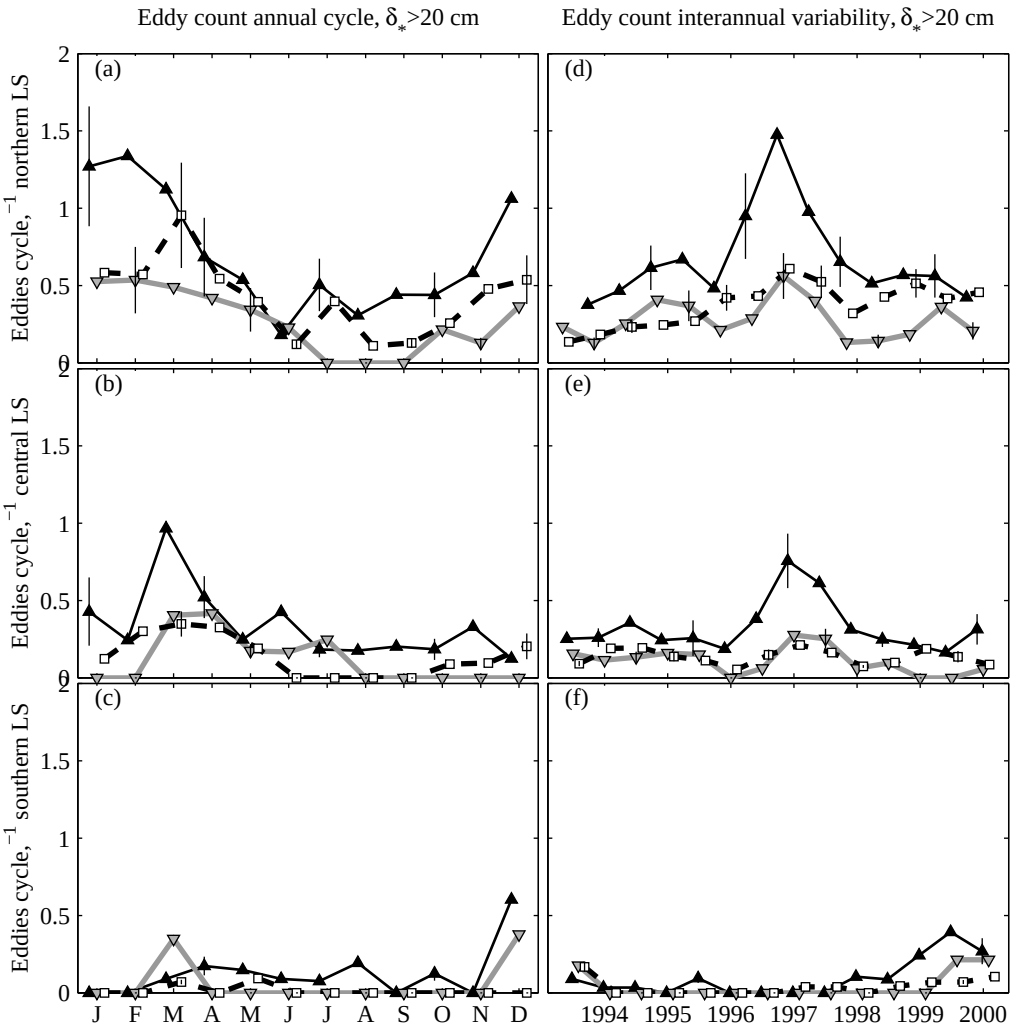

Figure 42. (Fig.42)

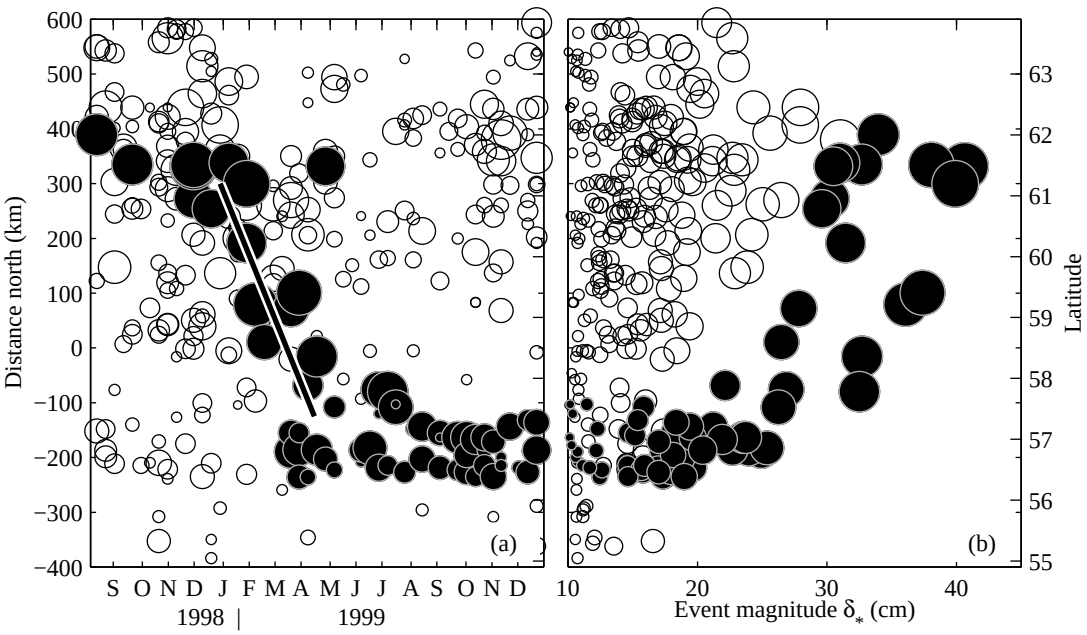

Figure 43. (Fig.43)

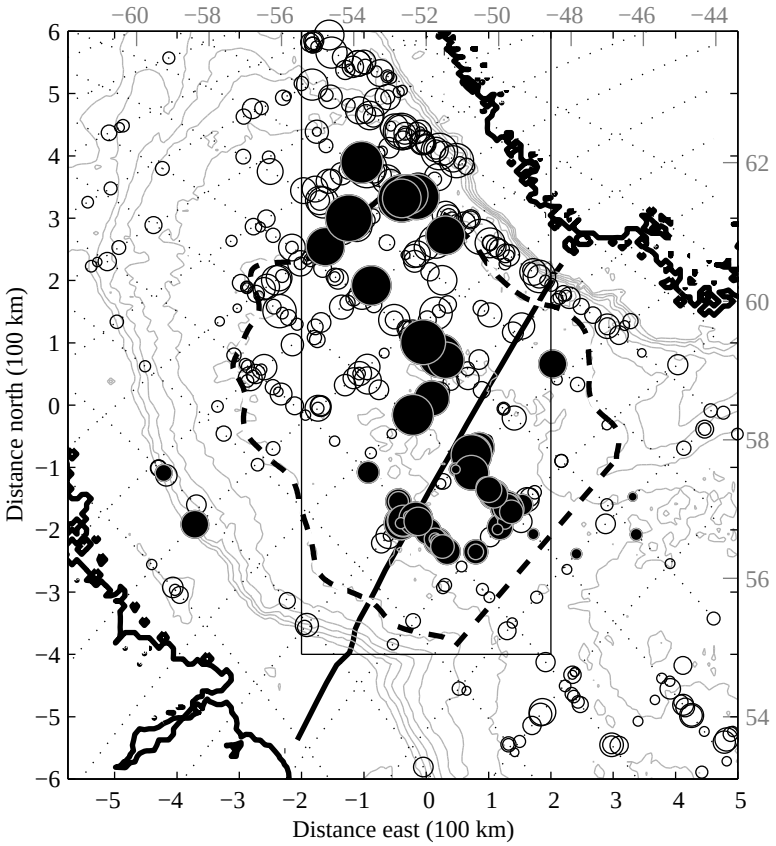

Figure 44. (Fig.44) .

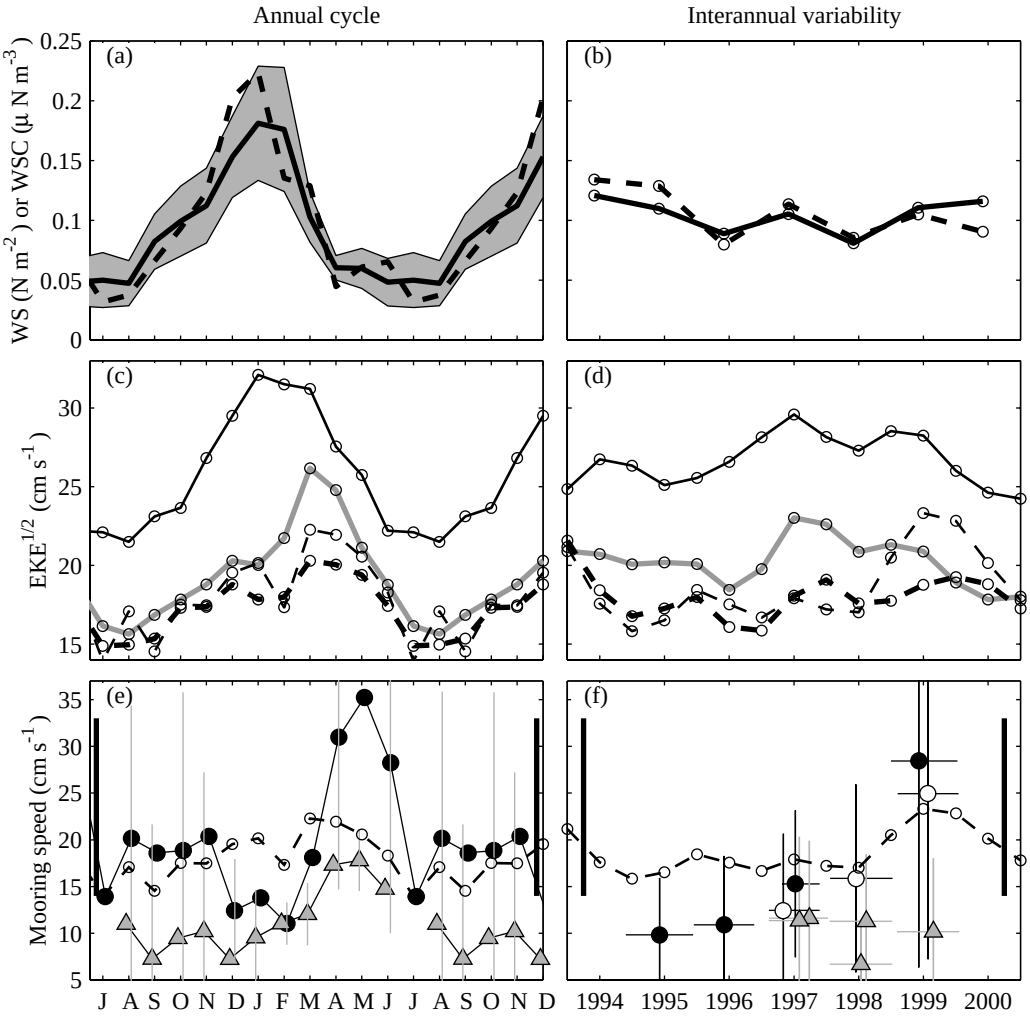

Figure 45. (Fig.45)